# First-Principles Calculations on the Electronic, Optical, and Vibrational Properties of Ultrawide-Band-Gap Semiconductor Materials

by

Kelsey Mengle

A dissertation submitted in partial fulfillment
of the requirements for the degree of
Doctor of Philosophy
(Materials Science and Engineering)
in the University of Michigan
2020

Doctoral Committee:

Associate Professor Emmanouil Kioupakis, Chair
Assistant Professor John Heron
Professor Zetian Mi
Associate Professor Pierre F. P. Poudeu

Kelsey Mengle

kmengle@umich.edu

ORCID iD: 0000-0001-6812-8113

# ACKNOWLEDGEMENTS

**Personal Acknowledgements**

**Manos:** I tell everyone that I could not imagine a better Ph.D. experience, and I mean that with my whole heart. I have been blessed and honored to work in your group over the past 4 years, and I don't know how I would be so successful without having such a wonderful advisor. You have been relentlessly supportive—academically, professionally, and personally. That consideration for my all-around well-being is what enabled me to be so successful. When I needed to talk to you about problems in my research or problems in my personal life, you were there for me. Thank you. The members of our research group have also warmed my heart from day one. Manos, I thank you endlessly for establishing a group with such amazing culture.

**Kioupakis Group**: We form deep familial relationships with one another and can talk about anything. I cherished sharing an office with you and learned so much from each of you. A special thanks goes to Guangsha, Dylan, Andrew, Christina, Jihang, and Logan who were there to help me when I started out. Our group made my Ph.D. experience unbelievable. I pass down my role as Group Bard to one of my juniors.

**Guangsha**: Thank you for being my mentor from the very beginning. One of the silly reasons why I am thankful to both you and Manos is that you worked together relentlessly to get me to like seafood. I am happy that we have continued to stay in touch over the last few years and that we will soon be neighbors in The Bay. I look

forward to our continued friendship.

**Nocona**: You're one of my best friends and my twin. You have been there for me through the best times and worst times, and you have always been supportive. I am deeply touched at how much I can rely on you and trust you. I will never forget how you were there with me through our First Annual Day of Accountabilitiness. Don't forget our promise in 9 years.

**Sieun**: I have such a deep respect and appreciation for you and our friendship. I am so blessed to have someone like you who I can confide in and know is always there for me. You will continue to be one of my best friends for life.

**Sahil**: You were the best undergraduate student researcher who I could mentor. Some of my happiest days were those when I made you laugh so hard you were nearly crying. I am so happy that I got to be your mentor for half of your undergrad career. I know that you are going to be incredibly successful. I have no doubt.

**Bryan, Swerds, and Derbs**: We immediately became friends when we entered Michigan together. I had endless fun with you all over the past four years. Many good times were had, and I look forward to reuniting with all of you often.

**Lisa, Kyle, and Neha**: The past four years have been some of the greatest in my life, and it was due to all of you. We weren't just housemates; we were (and are) a family. I lived in five different places during my Ph.D., and our house was my favorite.

**Hannah and Becky**: You lovely women are continually in my heart. I went through a wild ride while getting my Ph.D., and I knew that I could always count on you to ask about my adventures by phone and when I visited PA.

**Ju Won**: I am beyond grateful that I met you, and I wish we had met sooner. You are one of the purest people that I know, and I look forward to us getting to know each other even more.

**Kylee**: Thank you for showing me the albino groundhog every time I asked (at least 100 times) since I've been at Michigan. I am so proud at the successful young woman you've become. Keep up the good work. I am proud to call you my sister.

**Mom and Dad**: Thank you for establishing good academic habits in my life and for being supportive of all of my decisions. Working and studying hard for my Ph.D. was significantly easier because of this. I love and appreciate you so much.

*To the Kioupakis group—Sometimes you do and sometimes you don't.*

My dissertation is fully dedicated to my heart, Winchester. ♡

# TABLE OF CONTENTS

# LIST OF FIGURES

x

# LIST OF TABLES

# ABSTRACT

First-principles calculations enable an unprecedented atomistic insight to experimentally-observed phenomena on a massive scale. Such calculations can intelligently guide experimental efforts to save both human time and money. The methods in this dissertation are first-principles calculations based on density functional theory (DFT), many-body perturbation theory (using the GW method), and density functional perturbation theory (DFPT). With these methods, the electronic, optical, and vibrational properties of $\beta$-Ga$_2$O$_3$, h-BN, and r-GeO$_2$ are calculated and analyzed to assess their promise for deep-ultraviolet luminescence and high-power electronic applications.

First, I investigate the near-edge electronic and optical properties of $\beta$-Ga$_2$O$_3$. The fundamental band gap is indirect, but the minimum direct gap is only 29 meV higher in energy, which explains the strong near-edge absorption. Our calculations verify the anisotropy of the absorption onset and explain the range of experimentally reported band-gap values. Our results for the radiative recombination rate indicate that intrinsic light emission in the deep-UV range is possible at high excitation. I calculate the phonon dispersion, which relates to properties such as thermal transport, carrier mobility, and breakdown voltage. The large mode Grüneisen parameters reflect the anharmonicity of monoclinic $\beta$-Ga$_2$O$_3$ and help explain its low thermal conductivity. I also evaluate the electron-phonon coupling matrix elements for the lowest conduction band to determine the phonon mode that limits the mobility at room temperature. I apply these matrix elements to estimate the breakdown field of $\beta$-Ga$_2$O$_3$.

A second ultra-wide-band-gap material which shows promise for deep-UV luminescence applications is hexagonal boron nitride (h-BN). I examine the effects of stacking sequence and number of layers on the electronic and luminescence properties of h-BN structures. I explore the variations of the quasiparticle band gap and interband optical matrix elements for bulk, bilayer, and monolayer stacking polytypes. Although the fundamental gap for most structures is indirect, phonon-assisted transitions are strong (typically 600 times stronger than bulk Si) and enable efficient deep-UV luminescence. The polarization of the emitted light is transverse electric, which facilitates light extraction perpendicularly to the h-BN basal plane.

Rutile germanium dioxide (r-GeO$_2$) is an ultra-wide-band-gap semiconductor that has not been explored for semiconducting applications in electronic and optoelectronic devices. Our band-structure calculations indicate a dipole-forbidden direct band gap at $\Gamma$ with an energy of 4.44 eV and relatively low carrier effective masses. The first allowed optical transition at $\Gamma$ occurs at 5.04 eV ($\vec{E} \perp \vec{c}$). I also evaluate the optical absorption coefficient along both crystallographic directions. I theoretically predict the electron and hole mobility of r-GeO$_2$ as a function of temperature. At 300 K, the carrier mobilities (in cm$^2$ V $^{-1}$ s$^{-1}$) are $\mu_{elec} = 153.6$ ($\perp \vec{c}$), $\mu_{elec} = 74.1$ ($\parallel \vec{c}$), $\mu_{hole} = 4.7$ ($\perp \vec{c}$), and $\mu_{hole} = 2.2$ ($\parallel \vec{c}$). The thermal conductivities at 300 K are 37 W m$^{-1}$ K$^{-1}$ in-plane and 57 W m$^{-1}$ K$^{-1}$ out-of-plane. Last, I compare the Baliga's figure of merit (BFOM) for high-power-electronic applications and show that the BFOM for r-GeO$_2$ surpasses those of competing semiconductors, including $\beta$-Ga$_2$O$_3$.

Our theoretical characterization of the electronic, optical, and vibrational properties of $\beta$-Ga$_2$O$_3$, h-BN, and r-GeO$_2$ highlight the viability of these ultra-wide-band-gap semiconductors for applications in deep-UV luminescence and high-power electronics and provides a path for experimental development of materials for improved performance in devices.

# CHAPTER I

# Introduction

## 1.1 SEMICONDUCTORS

Semiconductors are an incredibly important class of materials for humankind, yet they have only been studied by humans for two centuries. Technologies incorporating semiconductors have existed an even shorter time, beginning in just 1947 with the introduction of the first transistor.[18] This is in great contrast to metals, which have been a part of human history for thousands of years. Despite being in its relative infancy, countless innovators, scientists, and engineers have imagined and realized many significant history-changing applications for semiconductors and created devices composed of them, at least in part. Sitting between metals and insulators in terms of electrical conductivity, semiconductors have characteristic energy thresholds, referred to as a band gap or $E_g$, that must be reached in the prescence of an electric field before an electron is excited from the valence to conduction band. The band gap varies widely between semiconductors and is used to characterize and classify each material into different sets of applications. This Ph.D. dissertation focuses on materials within the subclass of ultrawide-band-gap (UWBG) semiconductors for applications in deep-ultraviolet (deep-UV) luminescence and high-power electronics.

### 1.1.1 Applications

Semiconductor technologies span a huge range of applications. The first of which was a germanium (Ge)-based transistor in 1947 invented by Bardeen and Brattain at Bell Telephone Laboratories.[18] Key purposes of this invention included the ability to translate variations in electrical signals using a small, simple device and to be operative immediately after being turned on rather than waiting for components to heat up. Transistors benefited communications for ordinary civilians through integra-

**Timeline of compound semiconductor development**

▲ Timeline of compound semiconductor development
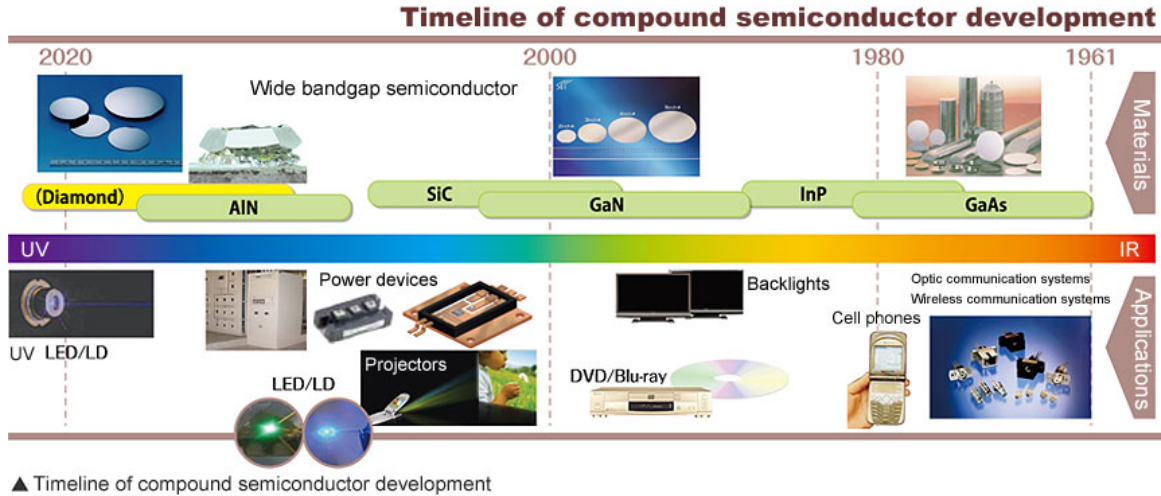
Figure 1.1: Various common semiconductor materials and their applications across the visible spectrum as well as in the ultraviolet and infrared.[1]

tion in radios and walkie-talkies. Governments subsequently found uses for these new devices in the police force and military.[19] Technology of today (espcially computers) relies heavily on silicon (Si) with many semiconductor companies based in the aptly-named "Silicon Valley" in California, U.S.A. All over the world, companies improve existing devices and create new products that impact all life. Many compound semi-conductors (*i.e.* semiconductors composed of two different atom types) are used in cell phones, displays, power devices, laser diodes, and more, which span wavelengths with lower energies in the infrared (IR) through the entire visible spectrum to higher energies in the UV and deep-UV. Figure 1.1 shows a sample of common materials and their corresponding applications throughout the history of compound semiconductor development.[1]

While applications utilizing energies lower than the deep-UV are highly impact-ful, semiconductors with higher energy band gaps have significant advances for op-toelectronics and other devices operating at high voltages or frequencies. A sampling of possible applications includes solid-state lighting (especially light-emitting diodes (LEDs), laser diodes, and deep-UV light emitters), UV detection in the solar-blind (wavelengths $\lambda < 280$ nm) and visible-blind ($\lambda < 400$ nm) regimes, and devices operat-ing at high temperature and/or power.[20–23] As can be seen in Figure 1.1, wide-band-gap semiconductors have only been studied significantly in the past two decades.[1] This leaves noticable opportunities for discovery of new materials (or applications), refinement of existing architectures, and engineering material structures to achieve specific desired properties. This dissertation will discuss several recent UWBG semi-

conductors and how their fundamental electronic, optical, and vibrational properties can be harnessed to advance technology as we know it.

### 1.1.2 Background Physics

To deeply understand semiconductor applications and predict the usefulness of a particular material for any given application, the basics of fundamental physics of semiconductors must be discussed.

On the atomic scale, electrons occupy spaces around the nuclei in atomic orbitals. In a crystalline solid, vast numbers of atoms are held together closely by interatomic forces. These electrons occupy so-called energy bands rather than orbitals. While atomic orbitals can be described mathematically with a radial term and an angular term which define the specific shape of the orbital, energy bands require an additional factor that takes into account the periodicity of the crystal lattice. The symmetry of a crystal lattice plays a key role in determining the shapes and energies of the bands. Atomic positions can be described with coordinates in real space, but electronic bands are described in reciprocal space—otherwise known as $k$-space. Due to crystal periodicity, electronic wavefunctions do not travel infinitely in one direction but instead undergo what is called a Bragg reflection at increments of $k = \pm\frac{1}{2}G$, where $n$ is an integer, and $G = 2\pi n/a$ corresponds to the reciprocal lattice vector for a real-space-lattice vector with magnitude $a$.[24]

The way to visualize the energy bands is through a band structure, where the $y$-axis corresponds to energy and the $x$-axis corresponds to the "crystal momentum" or direction in $k$-space. At each Bragg reflection, the bands fold such that they go backwards along the $k$-direction rather than continuing on to larger $k$ values. However, in general as bands fold, they continue to increase in energy. In a crystal with completely isotropic symmetry, *i.e.* a cubic system, the lattice vector magnitudes are equivalent. That is, $a = b = c$. In this case, the Bragg reflections occur at equivalent values of $k$ regardless of direction. As the crystal symmetry is broken and becomes more anisotropic, the energy bands also become anisotropic. Many fundamental material properties are derived from the band structure, thus the anisotropy results in direction-dependent properties. This is an ongoing theme for this dissertation as the majority of UWBG semiconductors have anisotropic crystal structures.

Already mentioned several times, the band gap of a semiconductor is its most prominent material property; it is what distinguishes a solid as a semiconductor rather than a metal or insulator. The band-gap value also dictates in which applications the material can be used. Just as each atomic orbital can hold only two electrons, so
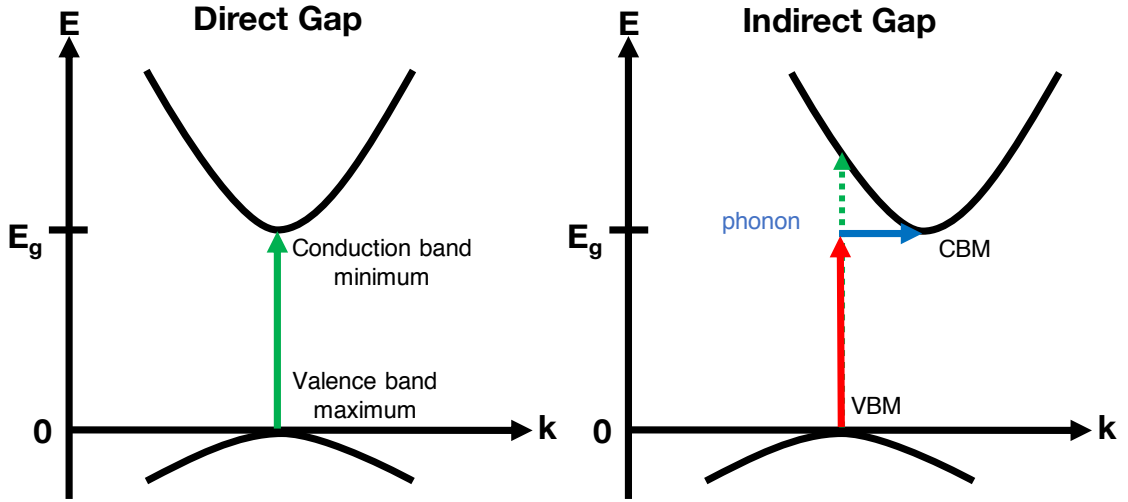
Figure 1.2: Schematic highlighting the difference between direct (left) and indirect (right) fundamental band gaps. The smallest direct transition in each case is shown with a green vertical arrow. For an electronic transition across the indirect band gap, the electron follows a two-fold process where it absorbs energy (red arrow) and a phonon (blue arrow) to reach the CBM. A direct transition is possible in the indirect-band-gap case (dashed green arrow), however, the energy needed for this transition to occur is larger than that of the fundamental band gap.

can each band. The band gap occurs between the top occupied (valence) band and bottom unoccupied (conduction) band. When excited with enough energy, electrons are free to move from their currently occupied band to another unoccupied band. Upon relaxation, an electron gives off energy thermally or by emitting a photon (light) and falls to a lower energy band.[25] This is the basis for electrical conduction and optical absorption and emission.

Two types of band gaps exist and can have significant impacts on the properties of the semiconductor. Figure 1.2 illustrates the differences between the band gap types and how electronic excitation occurs in either case. The simpler type of band gap is called a direct gap and describes a material where the highest energy of the top valence band (valence band maximum or VBM) and lowest energy of the bottom conduction band (conduction band minimum or CBM) occur at the same $k$ wavevector. Electronic excitation across a direct gap occurs vertically in the band structure, hence the electron only changes energy. In the case where the VBM and CBM are located at different $k$-points, the band gap is indirect. For electronic transitions to occur with the minimum possible energy (*i.e.* $E_g$) the electron must be excited with that much energy in addition to changing its crystal momentum. Atomic vibrations, or phonons, can assist an indirect-gap transition by coupling with an electron and

changing its momentum. Since this process requires two changes simultaneously rather than one, indirect-gap transitions occur less readily than direct transitions. Typically, this causes indirect-gap materials to poorly absorb and emit light at the energy of the intrinsic band gap. However, this is not always the case as will be shown in the following chapters. More important is the value of the band gap energy. An UWBG is essential for deep-UV luminescence where high energies are needed to emit photons of the desired wavelength and for high-power electronics where the wider the band gap, the more energy the material can withstand before destructive breakdown occurs.[20]

## 1.2 DEEP-ULTRAVIOLET LUMINESCENCE

At energies above the visible part of the electromagnetic radiation spectrum fall the UV and deep-UV. UV light is broken up into different classifications depending on wavelength, ranging from 10 nm to 400 nm (in terms of energy: 3.1 eV to 124 eV). The most well-known types of UV radiation in a general audience are the UVA (320 nm to 400 nm) and UVB (290-320 nm). Both of these UV bands have wavelengths that can damage skin, including wrinkles, aging, sunburns, and ultimately skin cancer.[26] At even shorter wavelengths (100 nm to 290 nm) lies the UVC band which is completely absorbed by the Earth's atmosphere and ozone layer. Slightly overlapping with the UVC band and down to the lowest UV wavelength of 10 nm is the extreme UV (EUV), which falls between 10 nm to 121 nm.

While the UVA and UVB negatively impact the lives of humans, UVC radiation can be extremely beneficial. The UVC energy range falls at wavelengths where many organic molecules strongly absorb. Thus, UVC light may be used to inactivate organisms such as bacteria and viruses by exposing them to this high-energy radiation and severely damaging their DNA, disabling their reproduction.[27] There is a great need for this particular application because food poisoning, for instance, is disturbingly common. In the United States alone, one out of six Americans fall ill annually from foodborne pathogens.[28] Symptoms of such illnesses are unpleasant; abdominal pain, diarrhea, bloody stools, fever, and vomiting are some milder symptoms of the bacterium *Salmonella*, but other pathogens can cause more serious harm.[27] Harmful microorganisms are also found on surfaces that are frequently touched by humans, in the air, and in water. UVC irradiation of each of these areas can control pathogens and reduce illnesses, hospitalizations, and even deaths.

Currently, the most widely used material that emits UVC light is mercury (Hg) in the form of a Hg lamp. The emission wavelength of Hg is 254 nm, which overlaps with
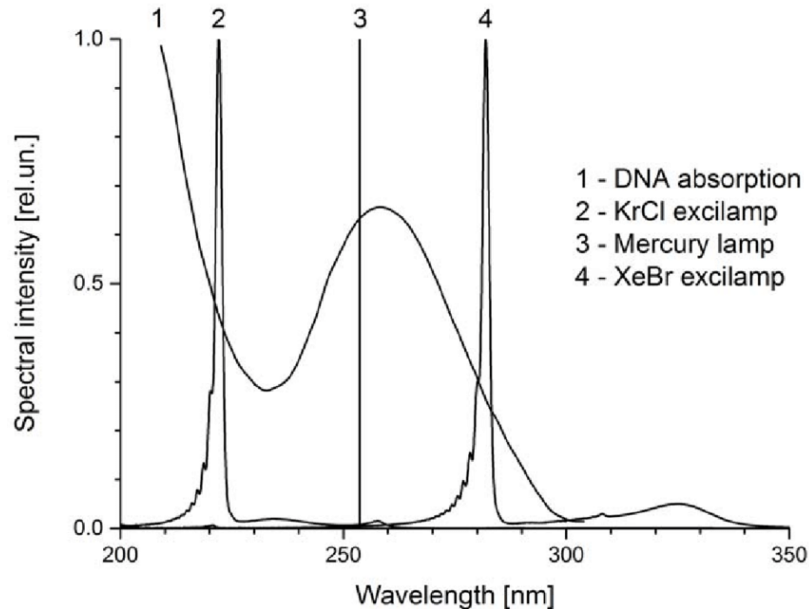
Figure 1.3: Absorption spectrum of DNA and emission peaks for three excilamps at wavelengths that have considerable overlap with the DNA absorption.[2]

a strong absorption peak in DNA. Figure 1.3 shows the characteristic DNA absorption peak as well as the emission peaks for three different excilamps that emit wavelengths in this spectrum.[2] While the Hg lamp emits at a wavelength which DNA absorbs more strongly than that of either KrCl or XeBr, there are several drawbacks to using Hg lamps. First, the goal of using a Hg lamp is to treat food and make it safer. However, in the event that the lamp cracks or breaks, mercury could contaminate the food. Other complications include the short lifetime of these devices, a significant amount of energy needed to power them, and that their emission wavelength is strictly fixed at 254 nm. The latter point is problematic because this wavelength may not always be the most effective in a given environmental condition. Emission-wavelength tunability could improve device efficacy. Deep-UV LEDs, on the other hand, can overcome these problems.

Many UWBG semiconductors exist, and they can be incorporated in deep-UV LEDs to achieve specific emission wavelengths for a given application while also being much less toxic than their Hg lamp counterpart. Semiconductors have the advantage of adjustable band gaps which can be tuned by tailoring material thickness, alloying with various ions, or changing the material entirely. One example of a highly-studied and commercialized semiconductor with a wide band gap of 3.4 eV (~365 nm) is wurtzite gallium nitride ($w$-GaN). GaN has been used in solid-state lighting for several decades. Shuji Nakamura, Isamu Akasaki, and Hiroshi Amano all contributed to the

6
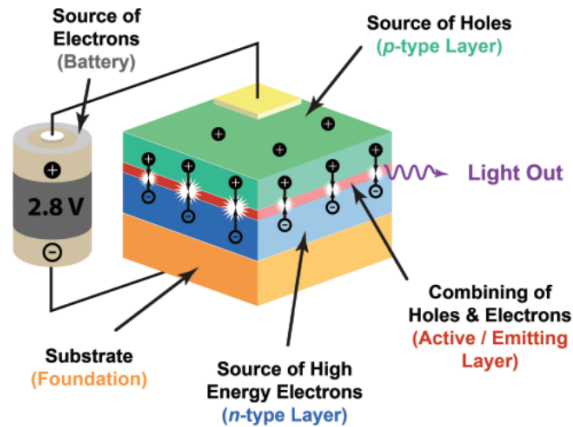
Figure 1.4: Basic structure of a light-emitting diode (LED) that is powered by a battery and is based on a double heterostructure. In the active layer (shown in red), electrons and holes recombine and emit photons with an energy equal to the band gap of the material used in that device layer.[3] [Reprinted from the Nobel Lecture by Professor Shuji Nakamura (https://www.nobelprize.org/uploads/2018/06/nakamura-lecture.pdf) with permission from ©The Nobel Foundation.]

invention and development of efficient blue LEDs that enable white light sources which are bright and energy-saving.[29,30] An example of the device structure is shown in Figure 1.4.[3] Their contributions to solid-state lighting won the trio the Nobel Prize in Physics in 2014. While this application for lighting is in the visible part of the spectrum for general lighting applications in the household, within businesses, public lighting, and other such uses, GaN LEDs can also be used for the germicidal applications discussed above.

When alloyed with a small amount of aluminum (Al) cation, the band gap can increase from the UVA to the UVC region. Würtele *et al.* designed two such types of GaN-based UV LEDs with emission peaks at 269 nm and 282 nm to test their suitability for disinfecting water.[31] Both static and flow-through tests were performed and showed effective disinfection when the water was irradiated for up to 3-4 minutes. The long time scale stems from the low output power of these devices, which is an area that can be improved in future work. Comparable experiments were conducted by Oguma *et al.* who achieved similar results.[32] Their AlGaN UV LED with an emission wavelength of 265 nm showed higher germicidal efficiencies compared to that emitting at 280 nm under the same fluence conditions, while the 280 nm LED was more effective in time-based conditions. One ongoing challenge with AlGaN LEDs is the low external quantum efficiency (up to ~20% but typically less).[33] GaN-based deep-UV LEDs have proven successful in some areas, however, there are limitations to their applications

7

because of the fundamental properties of GaN.

Materials are chosen for incorporation in devices based on their ability to perform a certain way under specific conditions. How materials behave is dependent on their fundamental material properties. In the case of deep-UV luminescence, some of the most important properties to consider are the band gap, efficiency of light emission, and ability to be doped with both negatively (electron) and positively-charged (hole) charge carriers. Even if a material has a band gap in the deep-UV energy range, the presence of free carriers[34] or defects can create centers for sub-band-gap absorption and emission[35]. The direction of light emission depends on the crystal structure. This can significantly affect the efficiency of light extraction. For instance, c-plane aluminum nitride (AlN) emits light with transverse-magnetic (TM) polarization, which means that the luminescence is not propagating in the desired direction for light extraction.[36] GaN inherently emits the desired transverse-electric (TE) polarization of light but must be alloyed with a wider-band-gap material like as Al to achieve deep-UV luminescence. GaN structures can be doped with only so much Al depending on strain conditions or the thickness of quantum well before the polarization switches from TE to TM, limiting the maximum usable band gap that can be achieved.[37] Challenges such as these in existing materials motivate the study of new UWBG semiconductors, alloys, size effects (e.g. quantum wells or nanowires)[38,39], or heterostructures[40].

## 1.3  HIGH-POWER ELECTRONICS

As for deep-UV luminescence applications, high-power electronics require a wide-band gap to push device usability to higher voltages and frequencies. Governments, businesses, and individuals invest intense research, time, and financial resources toward collecting and storing energy from renewable resources. However, renewable energy production and storage only solve part of the sustainability problem. Another lies in the conversion of electricity into usable forms for our daily lives (*e.g.*, to heat and light our homes or to power machinery in industry). Of all electricity that is transmitted and distributed, 5% is lost during the process.[41] Conversion inefficiencies must be addressed to achieve higher levels of sustainability, motivating research in new high-power electronics, which are used in the process of converting electricity from high to low voltages or frequencies and vice versa, *e.g.*, to charge our electronics or send cell-phone signals. Semiconducting materials are the workhorses of the electronics industry, which are characterized by an energy gap between their electronic

## Electricity generation, transmission, and distribution

power plant
generates electricity

transmission lines carry
electricity long distances

distribution lines carry
electricity to houses

transformer steps
up voltage for
transmission

neighborhood
transformer steps
down voltage

transformers on poles
step down electricity
before it enters houses

Source: Adapted from National Energy Education Development Project (public domain)

Figure 1.5: Schematic showing the process of transmitting and distributing electricity from the initial power generation at a plant to final arrival at a home, business, etc. Transformers are first used to increase the voltage to reduce losses during the long transmission distance and then are used to downconvert the electricity for final usage. Source: U.S. Energy Information Administration (Oct 2019). [4]

states. The wider the gap, the higher the electric field that can be applied without the device failing.

High voltages and frequencies cannot simply be avoided. Nuclear, hydro-electric, or coal plants, for instance, produce power that is at least several hundred megawatts. This is in great contrast compared to the amount of energy distributed to city or industry networks, which is on the order of 2-3 megawatts. Before power is downconverted to levels required by business or household uses, it is stored in a power grid and transmitted long distances across wires at very high voltages.[42] In the transmission of electricity, some is lost as waste heat due to electrical resistances of the wires and other components involved. To reduce the loss percentage, higher rather than lower voltages are transmitted. Step-down transformers are used convert this high voltage energy to low voltages for final distribution to our homes and businesses.[43] Figure 1.5 shows a schematic for this process from generation to transmission to final distribution of electricity.[4] UWBG materials are needed for this step because their high-energy-band gap enables them to withstand significant voltage levels before their chemical bonds physically break and fundamental structure is irreparably destroyed.

Currently, ultrawide-band-gap semiconductors with gaps wider than GaN, the incumbent technology, have been the focus of power-electronics materials research. But

what is the best semiconductor for power applications among the possible ultrawide-gap materials? Important material parameters for power electronics include the ability to be doped both with electrons ($n$) and with holes ($p$), efficient heat transport (high thermal conductivity), high electrical conductivity (mobility $\mu$), and the ability to withstand strong electric fields without damage (critical dielectric breakdown field $E_C$). The latter property has the largest contribution to the Baliga's figure of merit (BFOM) for potential power-electronic materials.[44,45] BFOM is used as a way to contrast candidate materials for this application, with the larger the FOM, the greater the promise for that particular material. BFOM for low frequencies is given by:

$$BFOM = \frac{1}{4}\epsilon_0 \mu E_C^3, \tag{1.1}$$

where $\epsilon_0$ is the static dielectric constant. The BFOM depends on the dielectric breakdown field to the third power but is only linearly dependent on mobility. Thus, $E_C$ has the strongest influence on the BFOM.

To maximize $E_C$ (and consequently BFOM), materials with large band gaps are preferred. As an electric field is applied to a material, electrons are excited to the conduction band and can climb to higher energies. When an electron reaches an energy equal to $E_{CBM}+E_g$, there is a chance for impact ionization. When this happens, an electron high in the CB loses energy equal to the band gap, which provides enough energy for an electron in the VB to reach the CB. Impact ionization causes carrier multiplication and can result in an avalanche of electrons that can break chemical bonds. When a material has a larger $E_g$, it can withstand higher electric fields before carriers reach the impact ionization energy. Electrons in an electric field normally lose energy by emitting phonons, the likelihood of which is determined by electron-phonon coupling strength. One method to estimate the breakdown field is via the von Hippel approach. Here, $E_C$ is defined as the lowest electric field at which the average energy loss due to phonons for all electrons in the CB with energies lower than $E_{CBM}+E_g$ is less than the average energy gain from the electric field. With this assumption, an electron will impact ionize as soon as it exceeds the energy $E_{CBM}+E_g$.[46]

Within this space, the $\beta$ polymorph of gallium oxide ($\beta$-Ga$_2$O$_3$) has recently been the focus of attention for high-power-electronic applications. While its carrier mobility is lower than that of other commonly used power-electronic materials, its band gap of $\sim$4.5 eV exceeds that of the others by more than 1 eV (except for diamond, which has an $E_g$ of 5.6 eV). The band gap of silicon carbide (SiC) is 3.2 eV, and that of GaN is 3.4 eV. However, the low thermal conductivity and the impossibility of $p$-type doping of $\beta$-Ga$_2$O$_3$ intrinsically limit its viability for power devices. To continue pushing the

frontier of efficient power devices and to overcome these issues, new materials must be identified and explored as candidate power-electronics materials. Research in this area will have a lasting impact in power-electronics technology and global sustainability by introducing semiconductors with superior properties for energy conversion to reduce the energy loss fraction.

## 1.4  COMPUTATIONAL METHODS

First-principles (also referred to as *ab initio*) calculations enable an unprecedented atomistic insight to experimentally-observed phenomena on a massive scale. Thousands of different materials can be tested for specific, desirable properties much quicker than would be possible experimentally. Computational methods can be applied to materials that are known to exist already or even to materials which have not yet been synthesized or will be impossible to ever synthesize. This theoretical output efficiency allows for clever collaborations between computational and experimental research groups. Calculations can intelligently guide experimental efforts to save both human time and money and to increase intellectual and technological progress and output.

In this dissertation, the results for every chapter were obtained with density functional theory (DFT), many-body perturbation theory (GW method), and Wannier interpolations. Chapters 3, 4, 5, and 6 also utilized density functional perturbation theory (DFPT). These techniques can provide insightful information regarding the electronic, optical, and vibrational properties of a material. Both open-source and commercial software packages are available that utilize these theories and can calculate the properties of interest.

### 1.4.1  Density Functional Theory

DFT is the primary method for studying many of the fundamental properties of wide-band-gap-semiconductor materials. DFT is a ground-state theory that can accurately predict and describe the atomic structure of a material. From DFT, information such as band structure, band gap, and effective mass can be obtained.

The origination of DFT came in 1964 when Hohenberg and Kohn published a paper describing the exact solution for the ground state of an interacting electron gas in an external potential.[47] The key contributions from this theory are to consider the electronic density $n(\boldsymbol{r})$ as variable and the realization of a functional $F[n(\boldsymbol{r})]$ (that is universal regardless of the external potential or number of particles) that describes all electronic systems which are in their ground state. The universal functional is given

by:

$$F[n(\boldsymbol{r})] = (\Psi, (T + U)\Psi), \tag{1.2}$$

where $\Psi$ is the ground state electronic density, $T$ is the kinetic energy of a single particle, and $U$ is the potential energy interaction between two particles that depends on their distance of separation. The variational approach is taken to determine the ground state energy of a given system, and the functional $F[n(\boldsymbol{r})]$ is used in:

$$E_v[n] = \int v(\boldsymbol{r})n(\boldsymbol{r}) + F[n], \tag{1.3}$$

where $E_v[n]$ is the ground state energy (achieved when the correct $n(\boldsymbol{r})$ is used) and $v(\boldsymbol{r})$ is a given potential.

DFT has proven extremely useful for predicting ground state atomic structures. However, the major drawbacks to using DFT are that it is only meant to describe the ground state and, thus, cannot explain excited state phenomena, and the band gap of semiconductors is often underestimated by $\sim$50%. A theory and method that goes beyond the ground state to the excited state is necessary for calculating and predicting properties such as electronic transition energies and optical absorption and emission.

### 1.4.2 Many-Body Perturbation Theory (GW Method)

In this dissertation, many-body perturbation theory (the GW method in particular) was used to overcome the challenges associated with DFT. In particular, the GW method can be used to correct the band gap that is known to be underestimated by DFT, correct the band dispersions, and can also calculate the excited state properties of materials. The GW method requires a starting point which is typically the wavefunctions and eigenvalues calculated by DFT. These ground-state values are treated as an initial guess to the quasiparticle wavefunctions $\psi_{n\mathbf{k}}^{\mathrm{QP}}$ and energies $E_{n\mathbf{k}}^{\mathrm{QP}}$ which are obtained by solving the equation:

$$\left[ -\frac{1}{2}\nabla^2 + V_{ion} + V_H + \Sigma\left( E_{n\mathbf{k}}^{\mathrm{QP}} \right) \right] \psi_{n\mathbf{k}}^{\mathrm{QP}} = E_{n\mathbf{k}}^{\mathrm{QP}} \psi_{n\mathbf{k}}^{\mathrm{QP}}, \tag{1.4}$$

where $\Sigma$ is the self-energy operator. The true and complete form of $\Sigma$ is an infinite power sum, but it is truncated to the first term within the GW approximation, which is the origin of its name:

$$\Sigma = iGW, \tag{1.5}$$

where $G$ stands for the Green's function, and $W$ is the screened Coulomb interaction (*i.e.* the potential one electron experiences in the presence of a second electron).[48]

### 1.4.3 Density Functional Perturbation Theory

The previous two methods (DFT and GW) are useful to obtain structural and electronic properties. However, the vibrational properties cannot be computed with these methods. Instead, an extension of DFT called density functional perturbation theory (DFPT) can be used to obtain the vibrational properties by, as the name suggests, perturbing the atoms in the crystal lattice and quantifying how the potential of atoms in the lattice changes.[49] A method developed earlier by Giannozzi *et al.* implemented a linear-response approach within DFT that required the use of supercells.[50] This method allowed for the first full-zone phonon dispersions of Si, Ge, GaAs, AlAs, GaSb, and AlSb. However, this approach is limited in implementation due to the computational cost required for supercells.

DFT relies on first-order derivatives of the energy, and DFPT relies on the second-order derivatives. With this information, the dynamical matrices (change in forces due to atomic displacements) for any wave vector can be calculated. Once a fine enough grid of wave vectors in the BZ (referred to as $q$-vectors for phonons) is known, the interatomic force constants (IFCs) can be computed via a Fourier transformation. With the IFCs, the calculation of a dynamical matrix and phonon frequency for any given $q$-vector is simple. Additional properties of interest that can be obtained through DFPT include the high-frequency dielectric constant $\epsilon_\infty$ and—for polar materials—Born effective charge tensors, which include information about how the second-order derivatives of energy change both from atomic displacements and electric fields.

The results from DFPT are used alongside electronic structure information calculated within DFT (or the GW method) to obtain additional material properties includings phonon-assisted optical transitions, electron-phonon coupling strength, thermal conductivity, and electron and hole mobilities.

### 1.4.4 Wannier Interpolation

While calculations of a band structure on a very fine BZ sampling grid within DFT are manageable, this is costly and not always possible (especially for larger systems) within the GW method. Within these methods, electronic states for a periodic crystalline solid are represented by extended Bloch orbitals corresponding to their specific electronic band $n$ and crystal-momentum $k$. Another way to mathematically

describe electronic states is through maximally localized Wannier functions, which are differentiated by their band index $n$ and the lattice vector for their corresponding unit cell $\mathbf{R}$.[51]

The Wannier method enables another description of the band structure and can be used to better understand the chemical bonds in solid materials. Its most practical use for the research discussed in this dissertation is the ability to interpolate band structures on very fine BZ sampling grids through interpolation rather than explicitly calculating a large number of $k$-points. For instance, a band structure calculated on a $\sim$6×6×6 coarse grid may be interpolated in a short amount of time to a $\sim$240×240×240 grid for properties requiring extremely fine $E$ versus $k$ information. This is particularly useful for obtaining finer GW band structures, both from a purely visual standpoint as well as to calculate optical properties from the electronic structure.

## 1.5 ORGANIZATION OF DISSERTATION

This dissertation discusses first-principles computational studies of three different ultrawide-band-gap semiconductors. The electronic, optical, and vibrational properties were explored with DFT, GW, DFPT, and other methods which will be described in the relevant chapters. All three of the different materials discussed share the common feature of an UWBG and, thus, the potential for device applications involving deep-UV luminescence and high-power electronics.

In Chapter II, the state-of-the-art UWBG material $\beta$-Ga$_2$O$_3$ is explored as a potential deep-UV light emitter despite having an indirect band gap. Chapter III involves the same material but focuses on vibrational (phonon) properties, phonon-phonon interactions, and electron-phonon coupling to understand the limits of the thermal conductivity, electron mobility, and dielectric breakdown field for high-power electronic applications. The electronic and optical properties of h-BN, are investigated in Chapter IV, where all of the possible stacking sequences of the basal planes are evaluated for prospective deep-UV luminescence applications. In Chapters V and VI, we propose a new material, r-GeO$_2$, to surpass the incumbant $\beta$-Ga$_2$O$_3$ for deep-UV luminescence and high-power electronics applications. Chapter V focuses on the electronic structure and optical properties, while Chapter VI delves into the temperature and direction dependent charge carrier mobilities and thermal conductivity.

# CHAPTER II

# Electronic and Optical Properties of $\beta$-Ga$_2$O$_3$

We use first-principles calculations based on many-body perturbation theory to investigate the near-edge electronic and optical properties of $\beta$-Ga$_2$O$_3$. The fundamental band gap is indirect, but the minimum direct gap is only 29 meV higher in energy, which explains the strong near-edge absorption. Our calculations verify the anisotropy of the absorption onset and explain the range (4.4-5.0 eV) of experimentally reported band-gap values. Our results for the radiative recombination rate indicate that intrinsic light emission in the deep-UV range is possible in this indirect-gap semiconductor at high excitation. Our work demonstrates the applicability of $\beta$-Ga$_2$O$_3$ for deep-UV detection and emission.

## 2.1 INTRODUCTION

The $\beta$ phase of gallium oxide ($\beta$-Ga$_2$O$_3$) is a promising wide-band-gap semiconductor for power electronics, deep-ultraviolet (UV) optoelectronics, and transparent conductors. Its large band gap results in a high breakdown voltage (8 MV/cm) desirable for power electronics,[52] such as field effect transistors (FETs) and Schottky barrier diodes.[53–55] The large gap also results in visible and UV transparency. Solar-blind photodetectors have been successfully fabricated with $\beta$-Ga$_2$O$_3$ nanostructures, such as nanowires[56] and nanobelts.[57] These devices demonstrate the potential of $\beta$-Ga$_2$O$_3$ in electronic and optoelectronic applications.

Despite numerous experimental and theoretical studies on $\beta$-Ga$_2$O$_3$, the nature and value of its fundamental band gap remain controversial. The room-temperature (RT) gap from optical absorption measurements ranges from 4.4 to 5.0 eV.[58] This controversy is partially due to the anisotropy of the crystal structure, which causes the absorption onset to depend on the polarization of the incident light. In addition, the small energy difference between the direct and indirect gaps has led to claims that

the fundamental gap is direct.[22,59] Other open questions are regarding luminescence from this material. Most photoluminescence studies do not show the intrinsic emission across the gap in the deep-UV ($\sim$265-278 nm) but only emission in the ultraviolet A (UVA) to visible range ($\sim$350-600 nm).[60] An exception is the report by Li *et al.* of luminescence at $\sim$265 nm and $\sim$278 nm, which correspond to the experimentally reported absorption edges.[60] Several mechanisms have been proposed to explain the UVA/visible luminescence of $\beta$-$Ga_2O_3$, including vacancies and other defects and self-trapped hole polarons.[60,61]

In this work, we use predictive calculations to investigate the near-edge electronic and optical properties of $\beta$-$Ga_2O_3$ to resolve open questions about the nature of its band gap. We determine the energies, orbital character, and locations of the band extrema and correlate them with the measured optical properties. We show that $\beta$-$Ga_2O_3$ is an indirect-gap semiconductor, but the lowest direct gap is only 29 meV larger. To understand the optical properties, we calculate the imaginary part of the dielectric function and the radiative recombination rates at various temperatures and carrier concentrations. Our results explain the different reported optical absorption onsets and demonstrate that intrinsic light emission is possible in this indirect-gap semiconductor.

## 2.2 COMPUTATIONAL METHODS

We performed the first-principles calculations using density functional theory and the local-density approximation (LDA) with the Quantum ESPRESSO code.[62] We used a plane-wave basis set with a 250 Ry cutoff energy and a Brillouin-zone sampling grid of 12$\times$6$\times$6. These values converge the total energy to 150 mRy and the electron eigenenergies for states within 6 eV from the band extrema to 1-2 meV. Subsequently, we corrected the band gap with many-body perturbation theory and the $G_0W_0$ method using the BerkeleyGW software.[63] For the GW calculations, the semi-core states were excluded from the parameterization of the generalized plasmon-pole model used to extrapolate the dielectric matrix to finite frequencies,[64] and we used an 8$\times$4$\times$4 Brillouin-zone sampling grid, a screened Coulomb energy cutoff of 45 Ry, and a summation over 3,000 bands. These parameters converge the band gap to within 0.1 eV. We did not consider excitonic effects in the evaluation of the dielectric functions, since excitonic interactions are weakened by phonon screening and dissociate at RT. We also applied the maximally localized Wannier function method[65] and the Wannier90 code[66] to obtain band structures, dielectric functions, and radia-

| | |
|---|---|
| $a$ (Å) | 3.037 |
| $b$ (Å) | 5.798 |
| $c$ (Å) | 6.293 |
| $\alpha$ | 103.414° |
| $\beta$ | 103.964° |
| $\gamma$ | 90.000° |

Table 2.1: Experimental primitive unit cell lattice parameters and angles of $\beta$-$Ga_2O_3$ used for the calculations.[8]

tive recombination coefficients.[67] GW calculations used semi-core norm-conserving pseudopotentials,[68] which treat the Ga $3s$, $3p$, and $3d$ electrons as valence states,[69] the generalized plasmon-pole model for the extrapolation of the dielectric function to finite frequency,[64] and the static-remainder approach to converge the sum over unoccupied states.[70] The radiative recombination coefficient was evaluated using Equation (6) in Ref. 67 by interpolating the GW quasiparticle energies and optical matrix elements to fine meshes ($168\times108\times108$) to sample the small region of the first Brillouin zone occupied by carriers.[67] The band occupations by free carriers were determined using Fermi-Dirac statistics and the frozen-band approximation. The conventional cell of monoclinic $\beta$-$Ga_2O_3$ belongs to the C2/$m$ space group and contains twenty atoms.[8] The gallium ions inhabit two crystallographically distinct positions with half of the ions in an octahedral and half in a tetrahedral geometry. Three different oxygen ion environments exist in the crystal structure, forming a distorted cubic close-packed arrangement. For our calculations we used the primitive unit cell containing four Ga and six O atoms (Figure 2.1). This specific primitive cell has a triclinic geometry, where two of the lattice vectors are similar in magnitude. Table 2.1 shows the experimental primitive unit cell lattice vectors and angles used in our calculations. We used the experimental lattice parameters and atomic coordinates without structural relaxation to avoid artifacts by theoretical structural optimization errors on the calculated band structure. Calculations were performed using the experimental lattice parameters and atomic positions (Table 2.1 and Figure 2.1).[8] The lattice vector magnitudes changed by 0.30%-0.68% upon relaxation and resulted in a direct band gap approximately 0.2 eV smaller compared to the unrelaxed structure.
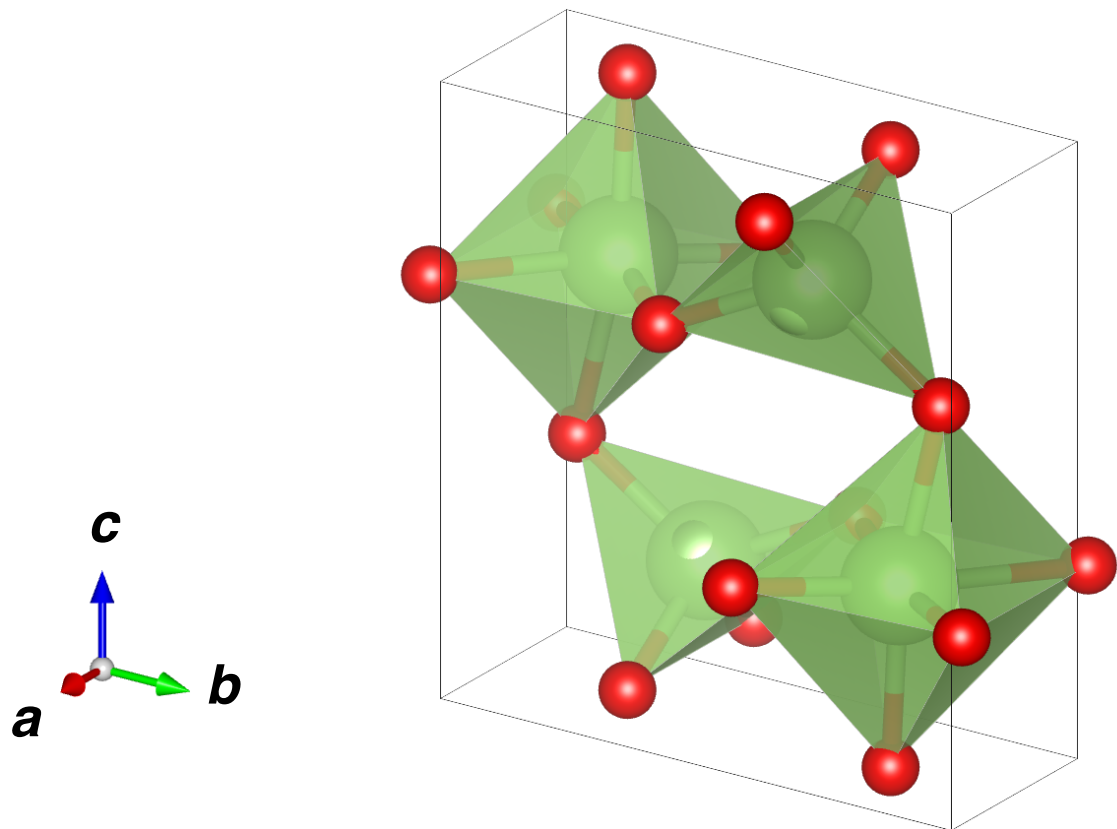
Figure 2.1: Primitive unit cell of $\beta$-Ga$_2$O$_3$, showing the tetrahedral and octahedral configurations of the Ga ions (large green spheres) with coordinated O ions (small red spheres) used in the calculations.

## 2.3 RESULTS AND DISCUSSION

### 2.3.1 Electronic Properties

The near-edge band structure of $\beta$-$Ga_2O_3$ calculated with LDA and LDA+$G_0W_0$ is shown in Figure 2.2 (the band structure over a broader energy range is shown in Figure 2.3). The quasiparticle $G_0W_0$ corrections to LDA simultaneously shift up the conduction bands and shift down the Ga $3d$ bands. It is important to note that the Ga $3d$ and O $2p$ orbitals are not hybridized at the LDA level. Such unphysical pd mixing is an artifact of LDA for materials containing cations with shallow d orbitals such as ZnO, InN, and CdO.[71] Since our LDA calculations do not show $pd$ mixing, LDA with semi-core states included in the valence is an accurate starting point for perturbative GW calculations. The topmost valence band (VB) of the $G_0W0$ band structure is composed predominantly of O $2p$ states with a band width of approximately 7.1 eV. The Ga $3d$ states are located between -12 and -14 eV below the valence band maximum (VBM), and the O $2s$ states are located between -17.5 and -19.5 eV below the VBM. The bottom conduction band consists primarily of Ga $4s$ and O $2s$ states. The conduction band minimum is located at the $\Gamma$-point. Both the LDA and LDA+$G_0W_0$ band structures exhibit the global valence band maximum slightly off the R point along the R-$\Gamma$ line. Note that the Brillouin zone special points were assigned based on the $TRI_{1b}$ lattice as determined by Setyawan and Curtarolo.[72]

Our LDA+$G_0W_0$ band structure and band gap are in overall agreement with previous calculations based on the Heyd-Scuseria-Ernzerhof (HSE) hybrid functional and experiment [polarized transmittance and angle-resolved photoemission spectroscopy (ARPES)] (Table 2.2). As expected, LDA severely underestimates the band gap; it predicts an indirect gap of 1.932 eV and a direct gap at $\Gamma$ that is 21 meV larger. The band gap remains indirect after $G_0W_0$ corrections with a vlue of 4.240 eV. Our LDA+$G_0W_0$ indirect gap is 29 meV smaller than the direct gap, in comparison to the 30-40 meV range reported in the literature.[58,73–75] This is in contrast to the HSE+GW results of Furthmüller and Bechstedt, which yield a direct gap.[73] The authors of Ref. 73 acknowledge that the discrepancy of their calculated direct gap with the experimentally measured indirect gap could be a result of numerical uncertainties. Our LDA+$G_0W_0$ indirect gap is only 0.2 eV smaller than measured values at RT. We note, however, that the calculated gaps should be compared to experimental data at 0 K, which are approximately 200 meV larger than RT values.[11] Despite the slight gap underestimation, the near-edge band features (indirect gap, symmetry of the matrix elements, etc.) are predicted correctly with LDA+$G_0W_0$ and yield accurate
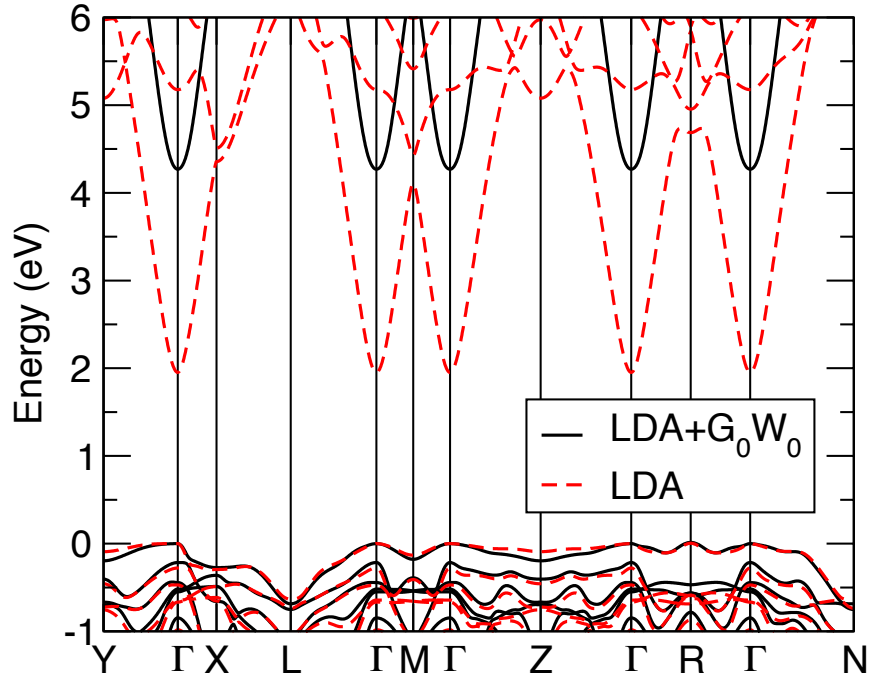
Figure 2.2: Near-edge band structure of $\beta$-Ga$_2$O$_3$ calculated with LDA (red dashed) and LDA+G$_0$W$_0$ (black solid). Both methods show an indirect band gap, the CBM at $\Gamma$, and the VBM near R. The LDA (LDA+G$_0$W$_0$) minimum direct gap is 1.953 eV (4.269 eV), which is 21 meV (29 meV) higher in energy than the indirect gap.
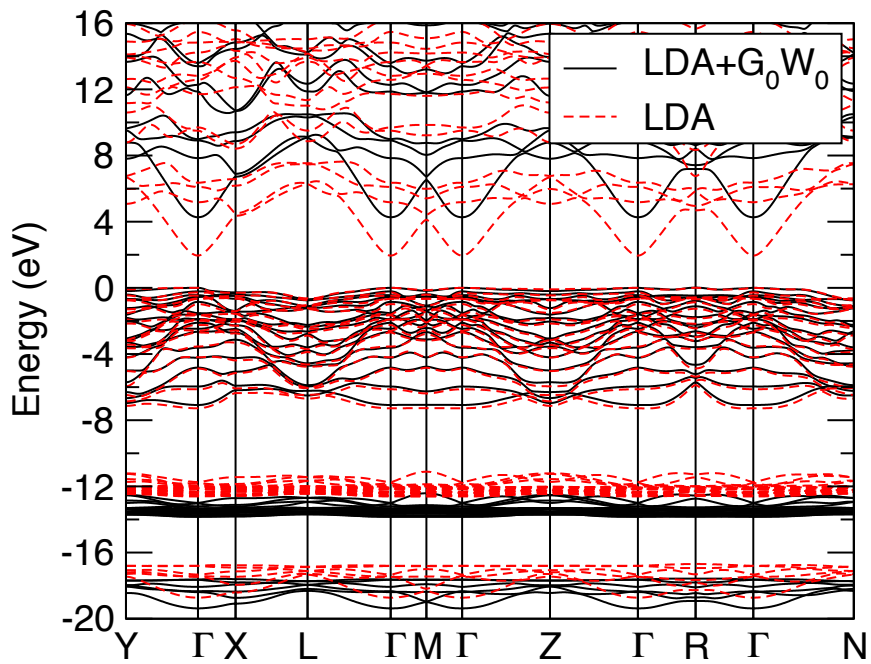


Figure 2.3: Band structure of $\beta$-Ga$_2$O$_3$ calculated with DFT-LDA (red dashed) and LDA+G$_0$W$_0$ (black solid) methods. Energies are referenced to the top of the valence band.

| Method | $E_{g,indirect}$ (eV) | $E_{g,direct}$ (eV) | Reference |
|---|---|---|---|
| LDA | 1.932 | 1.953 | This work[78] |
| LDA+$G_0W_0$ | 4.240 | 4.269 | This work[78] |
| HSE | 4.84 | 4.88 | 74 |
| HSE+GW | 5.046 | 5.038 | 73 |
| Experiment (RT) (polarized transmittance) | 4.43 | 4.48 | 58 |
| Experiment (RT) (ARPES) | $4.85 \pm 0.1$ | $4.9 \pm 0.1$ | 75 |

Table 2.2: The direct and indirect band gaps of $\beta$-$Ga_2O_3$ determined by various experimental and theoretical methods.

near-edge optical properties. Our bulk calculations cannot determine absolute band positions. Reported values for the electron affinity of $\beta$-$Ga_2O_3$ range from 2.95 eV to 4.00 eV.[76,77]

### 2.3.2 Optical Properties

To understand the directionally dependent experimental optical absorption spectra, we need to consider not only the band gap but also the optical matrix elements for the first several interband transitions. Numerous experiments reported directionally dependent absorption onsets using different polarization angles and crystal orientations.[58,79–83] The different edges arise from several hole bands of different symmetries that reside within 1 eV from the local valence band (VB) maximum at $\Gamma$.[73] Direct optical transitions from the topmost six valence bands to the bottom conduction band at $\Gamma$ occur at 4.27, 4.48, 4.71, 4.79, 4.82, and 5.12 eV, as determined from our LDA+$G_0W_0$ band structure, and correspond to polarization-dependent absorption onsets (Table 2.3 and Figure 2.4(b)). The optical matrix elements show that transitions to the conduction-band minimum (CBM) from the third and fifth VB from the top are forbidden. The other four transitions listed above are symmetry allowed. The 4.27 eV transition energy corresponds to polarization along $y$, 4.48 eV to $z$, and 4.79 and 5.12 eV to $x$. The $x$-direction is parallel to the $a$-axis, $y$ is parallel to the $b$-axis, and $z$ is 19.56° off of the $c$-axis. Note that we use different labels for the axes as compared to others in the literature.

The optical matrix elements of the allowed $\Gamma$-$\Gamma$ transitions explain the directionally dependent onset of the calculated imaginary part of the dielectric function (Figure 2.4(a)) since the matrix elements show that each of the bottom four transitions are allowed for only one polarization direction in this material. As seen in Figure 2.4, the energies of the absorption onsets match the allowed transition energies for the $\Gamma$-$\Gamma$

| VB Index | Energy (eV) | Matrix Element (atomic units) |
|----------|-------------|-------------------------------|
| 1 | 4.27 | $0.73\ \vec{y}$ |
| 2 | 4.48 | $0.73\ \vec{z}$ |
| 3 | 4.71 | $0$ |
| 4 | 4.79 | $0.34\ \vec{x}$ |
| 5 | 4.82 | $0$ |
| 6 | 5.12 | $0.72\ \vec{x}$ |

Table 2.3: Calculated energy differences and optical matrix elements for electronic transitions from the top five valence bands to the conduction band minimum at $\Gamma$.
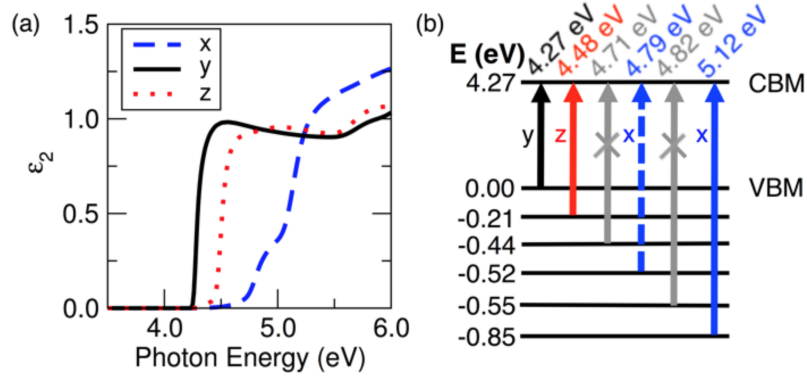


Figure 2.4: (a) Imaginary part of the dielectric function along the $x$-($E\|a$), $y$-($E\|b$), and $z$-($E\perp a,b$) directions evaluated with LDA+$\mathrm{G_0W_0}$. The absorption onset for light polarized along the $y$-axis (solid black curve) is the minimum LDA+$\mathrm{G_0W_0}$ direct gap (4.27 eV). Absorption measurements with light polarized along other crystallographic directions lead to an erroneous overestimation of the band gap. (b) The energies, characters (allowed or forbidden), and polarizations ($x$, $y$, or $z$) of optical transitions at the $\Gamma$ point explain the directionally dependent onset of the absorption spectra in (a).

transitions. The shoulder around 4.7-5.1 eV along the $x$-direction (also seen experimentally at a smaller intensity[83]) arises from the small but non-zero matrix element of the fourth from the top VB to the CBM, while the larger matrix element of the sixth from the top VB to the CBM dominates at higher energies. The energies on either side of the shoulder also agree with the allowed $\Gamma$-$\Gamma$ transition energies above. Our analysis of the matrix elements and the polarization-dependent absorption edges agrees with the results of Sturm *et al.*[83] Our results further validate that the measured absorption onset of $\beta$-Ga$_2$O$_3$ can be used to determine the fundamental gap ($\sim$4.4-4.5 eV at room temperature[58]) only after considering the anisotropy of this material and the lowest direct absorption onset along the $y(b)$ crystallographic direction. Optical measurements along different crystal axes and/or non-polarized light result in larger gap values (*e.g.*, 4.7 eV at RT[79]).

Our results also show that, despite having an indirect fundamental gap, $\beta$-Ga$_2$O$_3$ is capable of light emission similar to direct-gap materials. The local VBM at $\Gamma$, which corresponds to the lowest-energy direct optical transition, is only 29 meV lower than the global VBM at R. At low carrier concentrations and temperatures, all holes occupy the R valley. As the carrier concentration or temperature increases, holes begin to populate the $\Gamma$ valley as well. Energy isosurfaces of the top VB are found in Figure 2.5. As the $\Gamma$ valley fills with holes, light emission becomes possible. The radiative recombination rate $R_{rad} = \frac{dn}{dt} = Bn^2$ is proportional to the square of the carrier concentration $n$, where $B$ is the bimolecular radiative recombination coefficient.[84] The magnitude of $B$ was calculated for a range of carrier concentrations and temperatures (Figure 2.6). At 4 K and carrier concentrations up to $\sim 10^{20}$ cm$^{-3}$, $B$ is essentially zero. From 4 K to 200 K, the $B$ coefficient increases by tens of orders of magnitude to values typical of direct-gap semiconductors.16 Even at 4 K, the $B$ coefficient becomes non-zero as the carrier concentration increases to $10^{21}$ cm$^{-3}$, as degenerate carriers fill the $\Gamma$ valley. Over the carrier concentration range $10^{15}$—$3.5\times10^{19}$ cm$^{-3}$, the coefficient is maximum for a temperature of 200 K. From approximately $3.5\times10^{19}$—$4\times10^{20}$ cm$^{-3}$, the maximum occurs at 300 K. The $B$ coefficient decreases with subsequent temperature increase, as in direct-gap materials. Figure 2.7 shows the temperature dependence of the $B$ coefficient at a carrier concentration of $10^{15}$ cm$^{-3}$. Our results prove that, despite having an indirect band gap, $\beta$-Ga$_2$O$_3$ can emit light like a direct-gap material, albeit at a lower recombination rate.

We note that the deep-UV luminescence at photon energies corresponding to the band gap of $\beta$-Ga$_2$O$_3$ (4.4-5.0 eV) has not been observed for bulk or thin-film samples. The reported luminescence in the visible range is attributed to defects,[61] while
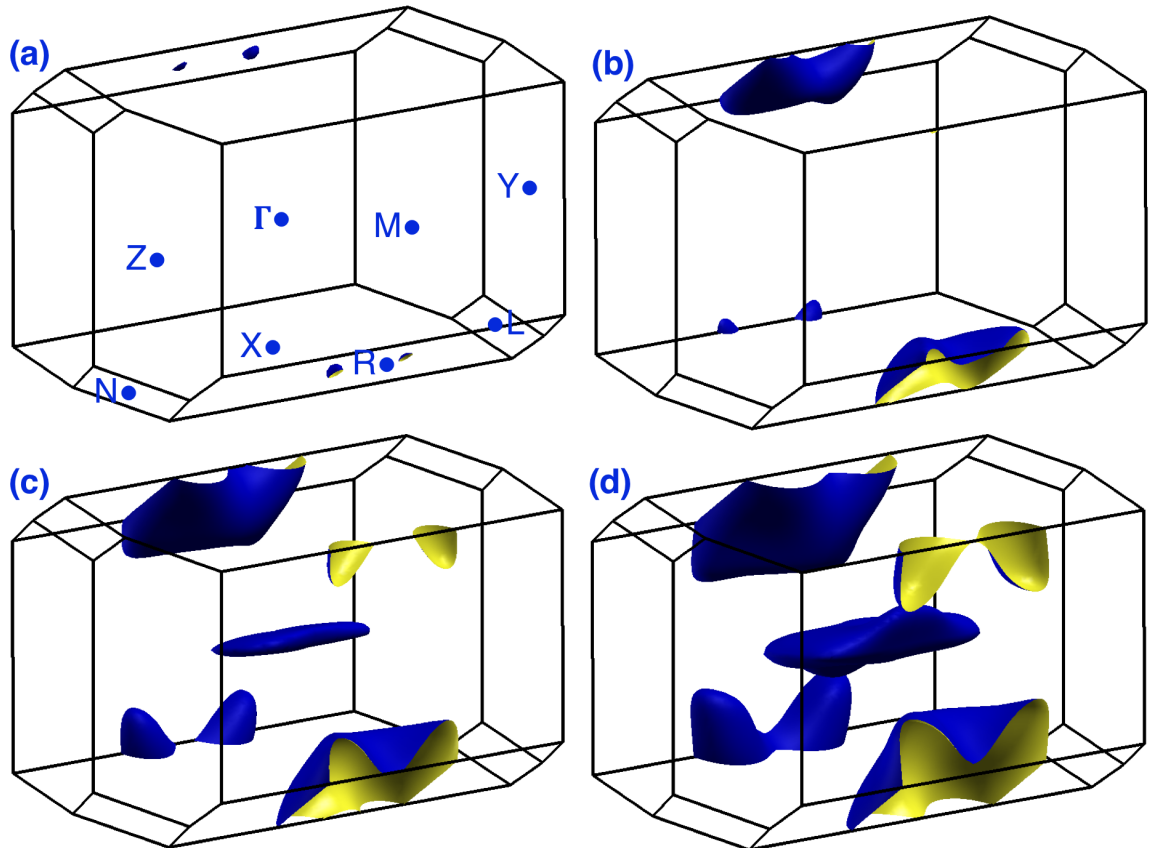
Figure 2.5: Top valence band energy isosurfaces of $\beta$-Ga$_2$O$_3$ in the Brillouin zone corresponding to the primitive unit cell in Figure 2.1 at (a) 0.001, (b) 0.025, (c) 0.050, and (d) 0.075 eV below the VBM. Near the VBM, all holes occupy the R valley. As the energy is lowered to approximately 30 meV below the VBM, holes start to fill the $\Gamma$ valley. High symmetry points are labeled in (a).
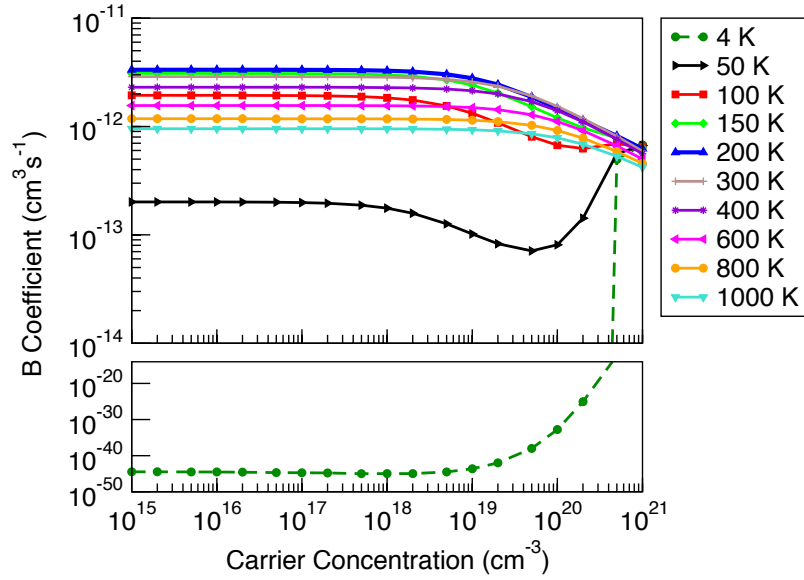
Figure 2.6: Bimolecular radiative recombination coefficient $B$ of $\beta$-Ga$_2$O$_3$ as a function of carrier concentration and temperature. The radiative coefficient drops to essentially zero at 4 K and low carrier concentrations (dashed dark green curve, bottom panel) but increases significantly at higher concentrations or temperatures as holes fill the $\Gamma$ valley (top panel) to values comparable to direct-gap semiconductors. With increasing temperature between 4 K and 200 K, the low-density ($10^{15}$—$3.5\times10^{19}$ cm$^{-3}$) $B$ coefficient increases and subsequently decreases for increasing temperature.
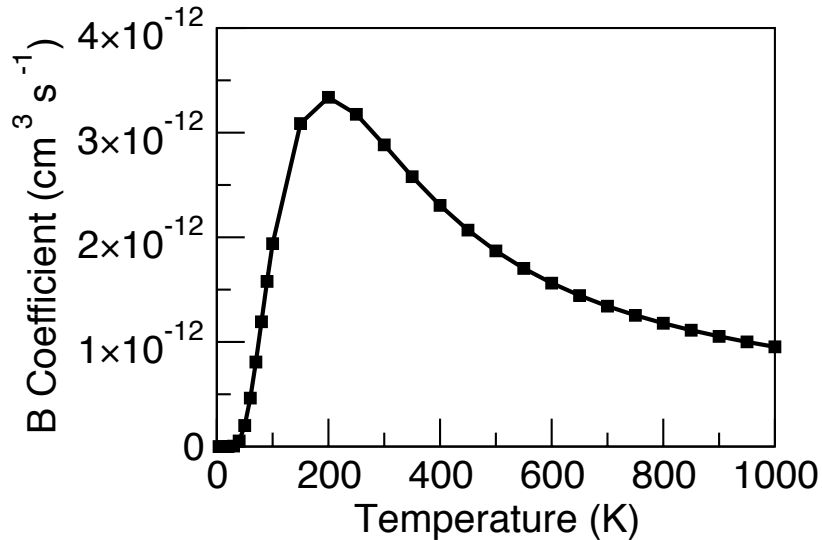


Figure 2.7: Low-density ($10^{15}$ cm$^{-3}$) radiative coefficient of $\beta$-Ga$_2$O$_3$ between 4 and 1000 K. The $B$ coefficient is maximum at 200 K before decreasing with increasing temperature as in direct-gap materials.

25

the near-UV luminescence (3.1 eV) is caused by localization of self-trapped hole po-larons.[85] However, deep-UV luminescence has been observed in $\beta$-Ga$_2$O$_3$ nanowires.[60] One explanation for the emergence of the deep-UV luminescence in nanowires is the reduced concentration of defects.[60] However, self-trapped hole polarons are expected to be stable even in nanowires and would prevent deep-UV luminescence. An additional factor that explains the deep-UV luminescence is the dissociation of hole polarons at high excitation power. The critical density of holes $n_c$ for the Mott transition of trapped hole polarons to free holes is given by (Ref. 86) $n_c^{1/3}(\epsilon_0\text{-}\epsilon_\infty)/\epsilon_0 \times R_P$ = 0.25, where $\epsilon_0$ = 10.2 is the static dielectric constant (Ref. 87), $\epsilon_\infty$ = 3.75 is the directionally averaged high-frequency dielectric constant (Ref. 73), and R$_P$ = 2.1 Å is the bound-state radius, which we assume to be equal to the O-Ga bond length due to the strongly localized nature of hole polarons (Ref.[85]). Our estimate for the critical density for the Mott transition of self-trapped hole polarons to free holes is therefore $4.3\times10^{20}$ cm$^{-3}$, which may be attained in nanowires due to the small sample volume. Our estimates, therefore, indicate that self-trapped hole polarons can dissociate into free holes at high excitation power and recombine with electrons across the gap to produce intrinsic deep-UV photons.

## 2.4   CONCLUSIONS

In summary, we investigated the electronic structure and optical properties of $\beta$-Ga$_2$O$_3$ with predictive atomistic calculations. Our results explain the broad range of experimentally reported band-gap values (4.4-5.0 eV at RT) due to the optical anisotropy of the crystal. Linearly polarized light and defined crystal orientations are needed to deduce accurate band-gap values from absorption measurements as in, *e.g.*, Ref. 11. Moreover, our calculations predict that deep-UV luminescence is possible in this indirect-gap material at sufficiently high carrier concentrations and temperatures. Our work elucidates the near-edge optical properties of this important semiconductor for power electronics and deep-UV optoelectronics.

# CHAPTER III

# Vibrational and Electron-Phonon Coupling Properties of $\beta$-Ga$_2$O$_3$: Impact on the Mobility and Breakdown Field

The wide-band-gap semiconductor $\beta$-Ga$_2$O$_3$ shows promise for applications in high-power and high-temperature electronics. The phonons of $\beta$-Ga$_2$O$_3$ play a crucial role in determining its important material characteristics for these applications such as its thermal transport, carrier mobility, and breakdown voltage. In this work, we apply predictive calculations based on density functional theory and density functional perturbation theory to understand the vibrational properties, phonon-phonon interactions, and electron-phonon coupling of $\beta$-Ga$_2$O$_3$. We calculate the directionally dependent phonon dispersion, including the effects of LO-TO splitting and isotope substitution, and quantify the frequencies of the infrared and Raman-active modes, the sound velocities, and the heat capacity of the material. Our calculated optical-mode Grüneisen parameters reflect the anharmonicity of the monoclinic crystal structure of $\beta$-Ga$_2$O$_3$ and help explain its low thermal conductivity. We also evaluate the electron-phonon coupling matrix elements for the lowest conduction band to determine the phonon mode that limits the mobility at room temperature, which we identified as a polar-optical mode with a phonon energy of 29 meV. We further apply these matrix elements to estimate the breakdown field of $\beta$-Ga$_2$O$_3$. Our theoretical characterization of the vibrational properties of $\beta$-Ga$_2$O$_3$ highlights its viability for high-power electronic applications and provides a path for experimental development of materials for improved performance in devices.

## 3.1 INTRODUCTION

An increasing amount of recent experimental and theoretical research has focused on the $\beta$ phase of gallium oxide ($\beta$-Ga$_2$O$_3$), with a primary focus on its applications in high-power electronic devices.[88] Because of its wider band gap and, correspondingly, its larger estimated breakdown voltage, $\beta$-Ga$_2$O$_3$ has been identified as a promising alternative for power electronics compared to other wide-gap semiconductors such as GaN and SiC.[23,52–54,58,89] The band gap of $\beta$-Ga$_2$O$_3$ is an especially important property to consider, with various reports placing it within a broad energy range of 4.4-5.0 eV.[10,52,58,74,90] Reasons for this uncertainty could include experimental growth conditions, sample type (*i.e.* film, bulk, etc.), sample quality, and light polarization. However, recent detailed experimental and theoretical absorption onset results point toward a fundamental band gap near 4.5 eV, i.e. at the lower limit of the reported range.[58,78,82] Although the band gap of Ga$_2$O$_3$ is lower than estimated in earlier reports, it is still much larger than other power-electronics materials, such as Si (1.1 eV), GaAs (1.4 eV), 4H-SiC (3.3 eV), or GaN (3.4 eV).[52] Since the breakdown field of a material increases strongly with increasing band-gap value, a reinvestigation of the breakdown field estimate is needed. This is achievable by studying the phonon and electron-phonon coupling properties. From the phonon dispersion, one can also obtain important information such as sound velocities and longitudinal optical (LO)-transverse optical (TO) splitting. Phonon-phonon interactions can provide information on the anharmonicity of different phonon modes, which can be used to explain finite thermal conductivity. Limited carrier mobility and breakdown field can both be explained by the electron-phonon coupling in a material. Each of these properties is important for high-power electronic applications.

In addition to the requirement of a wide band gap and large breakdown field, materials used in power electronics need to also exhibit large electron mobility to minimize Joule heating, as well as a high thermal conductivity to facilitate heat extraction. While the band gap and estimated breakdown field of $\beta$-Ga$_2$O$_3$ make it promising for power electronics, its electron mobility and thermal conductivity are lower than desired for such applications. An initial estimate placed the electron mobility of $\beta$-Ga$_2$O$_3$ around 300 cm$^2$ V$^{-1}$ s$^{-1}$.[52] However, both experimental and theoretical subsequent reports find much lower values. Various scattering mechanisms including acoustic deformation potential, ionized impurity, neutral impurity, and polar optical (PO) phonon scattering were analyzed alongside Hall-effect measurements by Ma *et al.* The results showed that the dominant mechanism limiting electron mobility

28

in $\beta$-$Ga_2O_3$ is PO phonon scattering, which limits the room temperature mobility to $<200$ cm$^2$ V$^{-1}$ s$^{-1}$ (for doping densities less than $\sim 10^{18}$ cm$^{-3}$).[91] Zhang $et$ $al.$ recently grew $\beta$-$(Al_xGa_{1-x})_2O_3/Ga_2O_3$ heterostructures with modulation doping, resulting in a high mobility 2D electron gas at the interface. They measured the highest experimental room temperature mobility in bulk $\beta$-$Ga_2O_3$ to date: 180 cm$^2$ V$^{-1}$ s$^{-1}$.[33] Two separate ab initio calculations using the Boltzmann transport equation (BTE) take into account scattering by PO phonons and impurities as well, resulting in room-temperature mobility values around 115 cm$^2$ V$^{-1}$ s$^{-1}$ for $n = 1.1 \times 10^{17}$ cm$^{-3}$ (Ghosh and Singisetti)[92] and 155 cm$^2$ V$^{-1}$ s$^{-1}$ for $n = 10^{17}$ cm$^{-3}$ (Kang $et$ $al.$).[93] On the other hand, the measured thermal conductivity depends on the crystallographic direction due to the anisotropic monoclinic crystal structure,[5] but the highest value is only 27 W m$^{-1}$ K$^{-1}$ along the [010] direction, and the lowest is 10 W m$^{-1}$ K$^{-1}$ along the [100] direction. First-principles calculations estimated the thermal conductivity along several directions (both cross-plane and in-plane) for a range of film thicknesses and found the highest value to be 21 W m$^{-1}$ K$^{-1}$ along the [010] direction.[94] To fully realize the promise of $Ga_2O_3$ as a high-power electronic material, the properties of phonons and their interactions with electrons and each other must be quantified to elucidate the atomistic origins of the inherent limits to its electronic and thermal transport properties.

In this work, we apply first-principles calculations based on density functional theory (DFT) and density functional perturbation theory (DFPT) to calculate the fundamental vibrational properties of $\beta$-$Ga_2O_3$, such as its phonon dispersion, phonon-phonon interactions, and electron-phonon coupling properties, and compare to available experimental data. Our results show that the monoclinic crystal structure strongly influences the phonon modes by causing strong anharmonicities, which are detrimental to the thermal conductivity. Moreover, our evaluated electron-phonon coupling matrix elements point to a specific low-frequency polar optical phonon mode that limits the electron mobility at room temperature. These matrix elements are also used to estimate a value of 6.8 MV/cm for the breakdown field of $\beta$-$Ga_2O_3$. Our results highlight the viability of $\beta$-$Ga_2O_3$ for applications in high-power electronics and propose a path for experimental development for improved performance in devices.

This chapter is organized as follows. In Section II we describe the computational methodology. Section III discusses the vibrational properties, including phonon frequencies, isotope effects, sound velocities, and heat capacity. Phonon-phonon interactions and their implications for thermal transport are described in Section IV, followed by a description of how the strong electron-phonon coupling in this material impacts

the mobility and breakdown field in Section V. Section VI summarizes the key results of this work.

## 3.2   COMPUTATIONAL METHODS

Our computational methods are based on DFT and DFPT. The Quantum ESPRE-SSO software package was used for the calculations within the plane-wave pseu-dopotential formalism and the local density approximation (LDA) for the exchange-correlation potential.[62,65,66,95] Norm-conserving pseudopotentials were used for all cal-culations with the Ga $4s$, $4p$, and $3d$ and O $2s$ and $2p$ electrons included as valence states. A plane wave energy cutoff of 130 Ry and a Brillouin-zone sampling grid of 4×8×4 were determined to converge the total energy of the system to within 1 mRy/atom. The experimental lattice parameters ($a = 12.214$ Å, $b = 3.0371$ Å, and $c = 5.7981$ Å)[8] and atomic positions for $\beta$-Ga$_2$O$_3$ were converted to the primitive cell and used as starting points for the structural relaxation calculation. For reference, the primitive-cell lattice and the reciprocal lattice vectors are referred in this paper as $a_1 = $ (-1.53, -1.46, 5.96), $a_2 = $ (3.06, 0, 0), $a_3 = $ (0, 5.82, 0), and $b_1 = $ (0, 0, 0.17), $b_2 = $ (0.33, 0, 0.08), and $b_3 = $ (0, 0.17, 0.04), respectively. The structure was relaxed from the experimental lattice parameters and atomic positions until the total force on all atoms was less than $2 \times 10^{-5}$ Ry/a$_0$ and the total stress was less than $4 \times 10^{-8}$ Ry/a$_0{}^3$ along each direction.

Phonon frequencies $\omega(q)$ were determined with DFPT for a 4×8×4 grid of phonon wave vectors $q$ using a stricter plane-wave cutoff energy of 170 Ry. The acoustic sum rule was applied to the phonon modes at $\Gamma$ to ensure that the acoustic modes sat-isfy $\omega(q) \to 0$ as $q \to 0$. Using the dynamical matrices produced during the phonon calculations, the interatomic force constants were generated via a Fourier interpola-tion and applied to determine the phonon dispersion with finer sampling along each reciprocal lattice vector direction. Frequencies obtained from the interatomic force constants were compared to those obtained from an explicit phonon calculation for two $q$-vectors [$q = $ (0, 0.25, 0) and $q = $ (-1.476, 0.812, 0.329)] that are not included in the coarse grid. The difference between the interpolated and explicitly calculated frequencies agree within 1.5 cm$^{-1}$ for both $q$-vectors, verifying the accuracy of the Fourier interpolation. The frequency splitting between the longitudinal (LO) and transverse optical (TO) modes for infrared-active (IR) phonons along the three re-ciprocal lattice vector ($b_j$) directions was calculated by including the non-analytical terms to the dynamical matrices for $q \to 0$ along each reciprocal-vector direction. The

electron-phonon coupling matrix elements between electron states $(n,k)$ and $(m,k+q)$ are given by:

$$g_{nk,mk+q} = \left(\frac{\hbar}{2M\omega_i(q)}\right)^{1/2} \langle \psi_{mk+q}| \, \partial_{iq}V \, |\psi_{nk}\rangle \,, \tag{3.1}$$

where $M$ is the total mass of the atoms in the unit cell, $\omega_i(q)$ is the frequency of phonon mode $i$ with wave vector $q$ and index $i$, $\partial_{iq}V$ is the derivative of the self-consistent potential resulting from ionic displacement by phonon $iq$, and $\psi_{nk}$ and $\psi_{mk+q}$ are electronic wave functions at bands $n$ and $m$ with wave vectors $k$ and $k+q$. All $g_{nk,mk+q}$ were determined for phonon wave vectors $q$ along the reciprocal lattice directions by evaluating the potential derivative $\partial_{iq}V$ for all phonon modes with DFPT and calculating the matrix element in (1) using the conduction-band electron wave functions at $\Gamma$ and at $q$. This method for the calculation of electron-phonon coupling matrix elements yields accurate values even for the polar-optical modes for $q \neq 0$.[96]

## 3.3    VIBRATIONAL PROPERTIES

### 3.3.1    Phonon Frequencies

The calculated phonon dispersion of $\beta$-$Ga_2O_3$ is shown in Figure 3.1. It includes thirty $(3N_{atom})$ phonon modes that span frequencies up to a maximum value of 784.92 cm$^{-1}$, which occurs at the zone edge along the $b_3$ direction. The frequency values for the phonon modes at $\Gamma$ are listed in Table 3.1 (IR-active modes) and Table 3.2 (Raman-active modes). Directionally dependent LO-TO splitting occurs at $\Gamma$ as expected for a polar material. Table 3.1 lists both the TO and LO frequencies for each mode and compares our calculated values (obtained within LDA and Quantum ESPRESSO) to the calculated results both by Schubert *et al.*[10] (obtained within LDA and Quantum ESPRESSO) and Liu *et al.*[9] (obtained with the Perdew-Burke-Ernzerhof functional[97] and the ABINIT code[98]) and to the experimental measurements using infrared (IR) and far-infrared (FIR) generalized spectroscopic ellipsometry (GSE) by Schubert *et al.*[10] and infrared spectroscopic ellipsometry (IRSE) by Onuma *et al.*[11]

Comparing our calculated TO modes to other calculations, the majority of the frequencies agree within 5% compared to the results of Liu *et al.*, and within 7% compared to Schubert *et al.* The majority of our reported TO frequencies agree with experiment (Onuma *et al.*) better than the calculations reported by Liu *et al.*, and five

of our reported values are closer by more than 5% to experiment. Overall, the average error in our TO frequencies compared to the results of Onuma *et al.* is 6.3%, while the average error of the results by Liu *et al.* is slightly larger (7.9%). All but one of the TO frequencies reported by Schubert *et al.* more closely match the experimental values of Onuma *et al.* than those reported here, with their average error in TO modes being 3.6%. Experimentally determined TO modes are also reported by Schubert *et al.* Half of our calculated frequencies are in better agreement with their experimental data than their calculations, and half of their calculated values are in better agreement than ours. Our TO frequencies have an average error of 4.0%, and Schubert *et al.* have an average error of 3.4%. All three calculations represented in Table 3.1 show an IR-active phonon mode with a frequency of $\sim$570-590 cm$^{-1}$. Schubert *et al.* also report an experimentally measured value in this range, but there is a noteworthy disagreement ($\sim$15%) between theory and experiment for this particular mode for the data reported by Onuma *et al.* who measured a value of 671 cm$^{-1}$.

We also report the LO frequencies for each IR-active mode as calculated along the three conventional crystal axes for better comparison with experiment. As expected from the crystallographic anisotropy, the LO-TO splitting depends on the direction, and some directions show larger splitting than others for a given phonon mode. The LO frequency for IR-active mode #5 agrees extraordinarily well across all reports (theoretical and experimental). A coincidental finding is that our LO frequencies agree better with the reported experimental TO frequencies than the corresponding LO frequencies for both the Schubert *et al.* and Onuma *et al.* data sets.

Table 3.2 lists the calculated Raman-active mode frequencies and compares them to the calculations by Liu *et al.*[9] and by Machon *et al.*,[12] who both employed ultrasoft pseudopotentials within the LDA in VASP.[99,100,100] Experimentally obtained Raman-active phonon frequencies reported by Machon *et al.* are also included. The majority of our calculated frequencies agree within 3% with the other two reported sets of calculated values. Both our calculated Raman frequencies and those calculated by Liu *et al.* match the experimental values reported by Machon *et al.* nearly as well as they match each other. Only three of our calculated frequencies disagree with experiment by more than 6%. Further comparisons of experimentally and theoretically obtained phonon frequencies, are reported in Refs. 11 and 101.

### 3.3.2   Isotope Effects on the Phonon Dispersion

Previous work by Khurgin *et al.* studied the LO phonon modes of mixtures of GaN isotopes and found that isotope disorder can have a beneficial impact on ma-
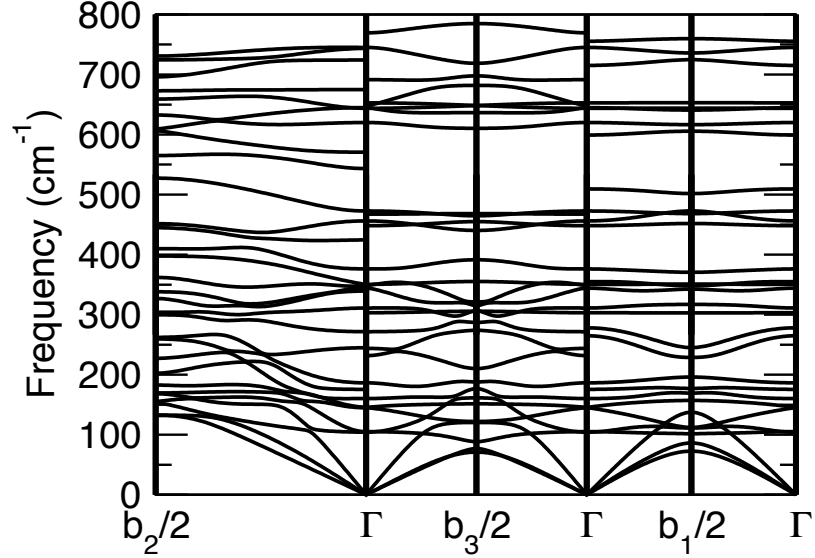
Figure 3.1: The phonon dispersion of $\beta$-Ga$_2$O$_3$ along the directions of the reciprocal lattice vectors.

| Mode Index | Present Work (Calc.) TO | LO a | b | c | Liu *et al.*[9] (Calc.) TO | LO | Schubert *et al.*[10] (Calc.) TO | (Exp.) TO | LO | Onuma *et al.*[11] (Exp.) TO | LO |
|---|---|---|---|---|---|---|---|---|---|---|---|
| 1 | 145.63 | 145.65 | 145.99 | 145.63 | 141.6 | 146.5 | 155.69 | 154.8 | 156.3 | - | - |
| 2 | 175.52 | 177.89 | 175.52 | 230.11 | 187.5 | 190.5 | 202.4 | 213.8 | 269 | - | - |
| 3 | 243.78 | 264.92 | 243.78 | 251.52 | 251.6 | 264.5 | 260.4 | 262.3 | 286 | 272[a] | 284[a] |
| 4 | 271.55 | 277.42 | 271.55 | 271.69 | 265.3 | 283.6 | 289.71 | 279.2 | 305 | 287[a] | 301[a] |
| 5 | 303.17 | 306.85 | 343.07 | 303.17 | 296.2 | 325.5 | 327.45 | 296.6 | 345.9 | 301[b] | 343[b] |
| 6 | 346.94 | 358.76 | 346.95 | 352.88 | 343.6 | 354.1 | 365.84 | 356.8 | 389 | 357[a] | 387[a] |
| 7 | 423.14 | 445.23 | 423.14 | 447.66 | 383.5 | 510.6 | 446.83 | 432.6 | 562 | 448[b] | 561[b] |
| 8 | 448.16 | 486.56 | 546.76 | 448.16 | 410.5 | 484.7 | 475.69 | 448.7 | 595 | 486[a] | 590[a] |
| 9 | 567.48 | 616.66 | 567.48 | 666.65 | 574.3 | 625.3 | 589.86 | 572.5 | 709 | 673[a] | 707[a] |
| 10 | 652.77 | 655.15 | 741.92 | 652.77 | 647.9 | 738.5 | 678.39 | 663.2 | 770 | 671[b] | 767[b] |
| 11 | 676.01 | 720.72 | 676.01 | 686.91 | 672.6 | 728.2 | 705.78 | 692.4 | 781.3 | 716[a] | 762[a] |
| 12 | 725.62 | 746.79 | 725.62 | 764.26 | 741.6 | 764.6 | 753.76 | 743.5 | 810 | 774[a] | 798[a] |

[a] $E \| a$
[b] $E \| b$

Table 3.1: Calculated frequencies (in cm$^{-1}$) for IR-active phonon modes. Our values are compared to the computational results of Liu *et al.*[9] and Schubert *et al.*[10] and the experimental values measured by Schubert *et al.*[10] and Onuma *et al.*[11] Superscripts "*a*" and "*b*" correspond to the direction in which the electric field was applied in the IRSE experiments by Onuma *et al.*

| Mode Index | Present Work (Calc.) | Liu et al.[9] (Calc.) | Machon et al.[12] | |
|---|---|---|---|---|
| | | | (Calc.) | (Exp.) |
| 1 | 104.21 | 104.7 | 104 | 110.2 |
| 2 | 105.11 | 112.1 | 113 | 113.6 |
| 3 | 144.83 | 141.3 | 149 | 144.7 |
| 4 | 160.21 | 163.4 | 165 | 169.2 |
| 5 | 186.4 | 202.3 | 205 | 200.4 |
| 6 | 311.07 | 315.8 | 317 | 318.6 |
| 7 | 344.15 | 339.7 | 346 | 346.4 |
| 8 | 350.48 | 348.3 | 356 | — |
| 9 | 376.18 | 420.2 | 418 | 415.7 |
| 10 | 456.16 | 459.4 | 467 | — |
| 11 | 472.68 | 472.8 | 474 | 473.5 |
| 12 | 620.03 | 607.1 | 600 | — |
| 13 | 643.76 | 627.1 | 626 | 628.7 |
| 14 | 644.83 | 656.1 | 637 | 652.5 |
| 15 | 745.19 | 757.7 | 732 | 763.9 |

Table 3.2: Calculated frequencies ($cm^{-1}$) of the Raman-active phonon modes. Our results are compared to the computational work by Liu et al.[9] and to the reported computational and experimental results by Machon et al.[12]

terials for high-power electronic applications by increasing the density of LO phonon modes, thereby enabling more efficient cooling and an increased drift velocity.[102] Motivated by this finding and to further understand the vibrational properties of isotope-substituted $\beta$-$Ga_2O_3$, we calculated the phonon frequencies at $\Gamma$ for four different isotope substitutions ($Ga^{69}$, $Ga^{70}$, $O^{15}$, and $O^{16}$) in place of atoms with the isotopically averaged weight (i.e., 69.723 amu for Ga and 15.999 amu for O). For each comparison, we kept the mass of one atom type as its isotopic average and substituted the other with the isotopically pure value for all atoms of that type in the primitive cell.

Figure 3.2 shows the phonon frequencies for the TO [Figure 3.2(a)], LO [Figure 3.2(b)], and Raman [Figure 3.2(c)] modes for each isotope variant. Reported LO values correspond to the largest LO-TO splitting out of the three reciprocal lattice vector directions. The percentile differences relative to the isotopically-averaged material are listed in Figure 3.2(d)-(f). Our results show that the isotope substitution of oxygen by $O^{15}$ has the strongest effect on the phonon frequencies compared to the isotopically-averaged material. All of the high-frequency modes and approximately half of the low-frequency modes increase in frequency by about 2.5-3% in $Ga^{69.723}O^{15.000}$ compared to the average. Changing the O mass from 15.999 amu to 16.000 amu has essentially no

effect on the frequencies, as is expected from such a small mass variation. Increasing the mass of Ga atoms to 70.000 amu resulted in a decrease in frequency of about 0.2% for the lower half of the phonon modes, while decreasing their mass to 69.000 amu increases the frequency of those same modes by $\sim$0.1-0.5%.

The physical origin of the isotopic variation of the vibrational frequencies stems from the type of atoms that dominate the vibrations in each frequency range. The Ga atoms primarily contribute to many of the phonon eigenmodes at low frequencies. Since the fractional variation of the Ga mass between isotopes is small ($|\frac{\Delta m}{m}|\approx1.4\%$), isotope substitution has a small effect on the frequency of those modes (up to $|\frac{\Delta\omega}{\omega}| = \frac{1}{2}|\frac{\Delta m}{m}|\approx0.7\%$) On the other hand, the motion of the lighter O atoms dominates atomic vibrations at the high-frequency end of the spectrum and some of the low-frequency phonons. Since the fractional change of the O mass is larger ($|\frac{\Delta m}{m}|\approx6.3\%$), it results in a stronger variation of the O-dominated mode frequencies ($|\frac{\Delta\omega}{\omega}|\approx3.1\%$).

### 3.3.3  Sound Velocities and Heat Capacity

The phonon dispersion is also crucial in determining other properties of a material such as the sound velocity $v$ and heat capacity $C_V$, which are important in the evaluation of the lattice thermal conductivity. Table 3.3 shows the sound velocity of $\beta$-$Ga_2O_3$ along the reciprocal lattice vector directions for each of the three acoustic modes. The sound velocity takes its lowest value (2.90 km/s) for the bottom transverse acoustic (TA) mode along the $b_2$-direction. The largest value (7.55 km/s) also occurs along the $b_2$-direction for the longitudinal acoustic (LA) mode. In comparison, the lowest sound velocity in GaN is $\sim$4 km/s, and the largest is $\sim$8 km/s.[103] Since the sound velocities of $Ga_2O_3$ are only slightly lower than GaN, they cannot account for its much lower thermal conductivity, the origin of which will be examined later. The heat capacity at constant volume of $\beta$-$Ga_2O_3$ is calculated from the Helmholtz free energy $F$ according to $C_V = -T((\partial^2 F)/(\partial T^2))_V$. First, the phonon density of states (DOS) was calculated with DFPT in Quantum ESPRESSO. From the phonon DOS, the Helmholtz free energy was calculated as a function of temperature, and the second derivative with respect to temperature was taken using the finite-difference method to obtain the heat capacity. Figure 3.3 shows the heat capacity at constant volume $C_V$ over a temperature range from 0-1000 K. At high temperatures, the heat capacity reaches the Dulong-Petit limit of $3N_{atom}k_B = 4.14\times10^{-22}$ J/K per primitive cell. Also shown in Figure 3.3 is the Debye temperature ($\Theta_D$) of $Ga_2O_3$ (738 K) which was determined from experimentally measured heat capacity data and the Debye model.[5] For comparison, GaN has a lower Debye temperature of 586 K.[104]
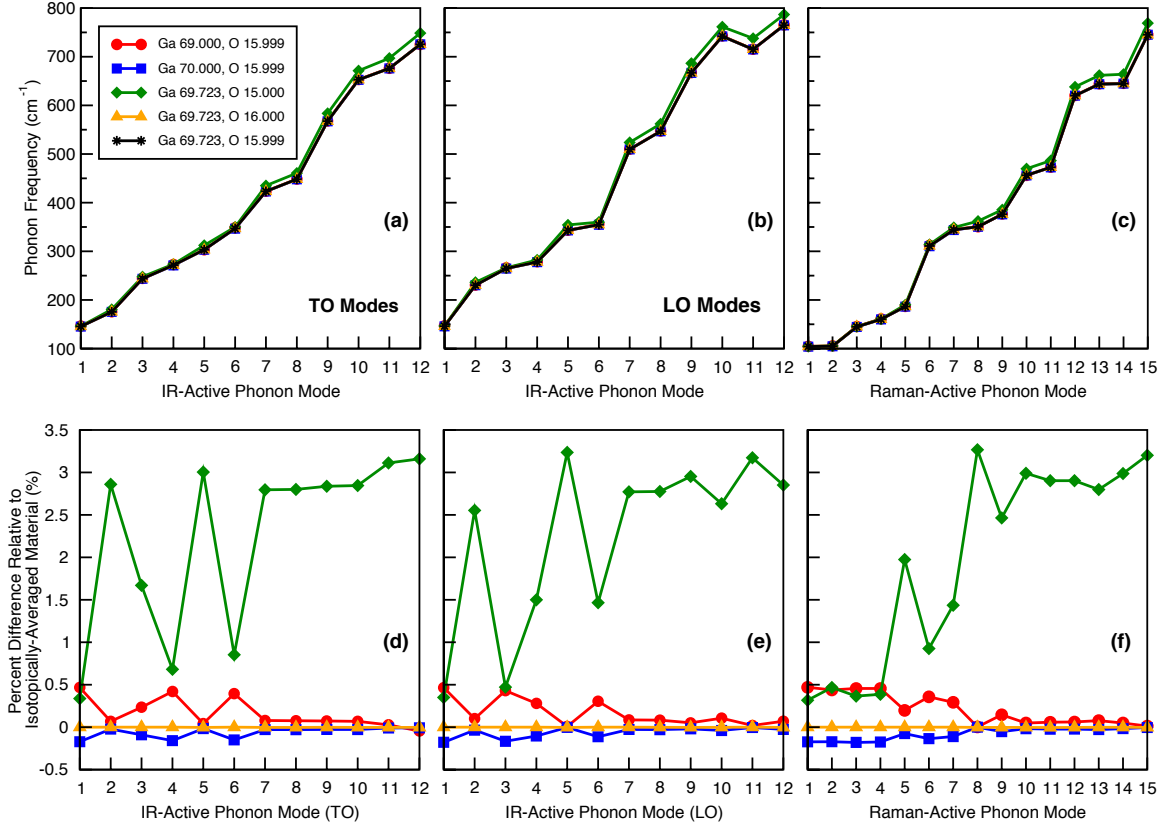
Figure 3.2: Absolute [(a)-(c)] and relative [(d)-(f)] variation of the vibrational frequencies of $\beta$-Ga$_2$O$_3$ by isotopic substitution for the (a), (d) IR-active TO modes; (b), (e) IR-active LO modes with the highest frequencies out of the three reciprocal lattice vector directions; and (c), (f) Raman-active phonon modes. Substitution of oxygen by the O$^{15}$ isotope has the strongest effect on the phonon frequencies, increasing the values by up to $\sim$3% particularly for the highest-frequency modes.

| | Sound Velocities (km/s) | | |
|---|---|---|---|
| | $\Gamma\rightarrow\boldsymbol{b}_1$ | $\Gamma\rightarrow\boldsymbol{b}_2$ | $\Gamma\rightarrow\boldsymbol{b}_3$ |
| (Bottom) TA | 3.57 | 2.90 | 2.99 |
| (Top) TA | 3.99 | 4.01 | 3.20 |
| LA | 6.18 | 7.55 | 7.46 |

Table 3.3: Directionally dependent sound velocities of $\beta$-Ga$_2$O$_3$ for the three acoustic phonon branches along the direction of each reciprocal lattice vector.
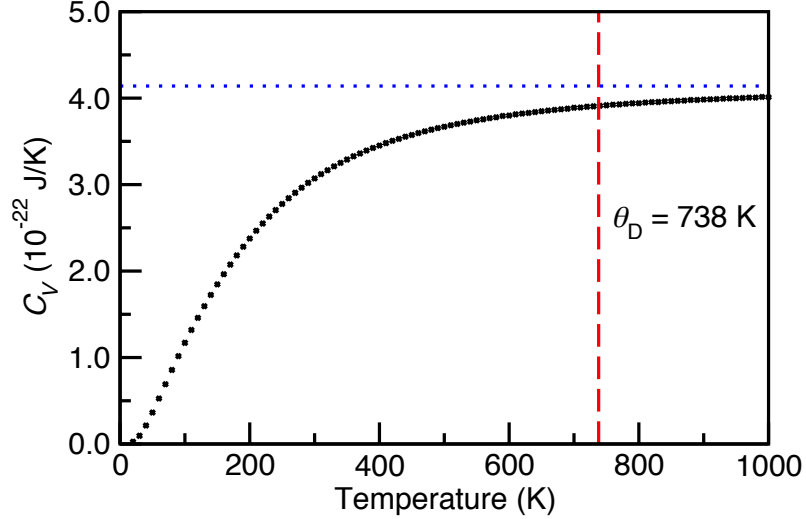
Figure 3.3: The calculated heat capacity per unit cell at constant volume of $\beta$-Ga$_2$O$_3$. The heat capacity approaches the value of $3N_{atom}k_B = 4.14\times10^{-22}$ J/K per 10-atom primitive cell at high temperatures, in agreement with the Dulong-Petit law (blue, dotted horizontal line). The Debye temperature ($\Theta_D = 738$ K)[5] is shown with a red, dashed vertical line.

## 3.4   PHONON-PHONON INTERACTIONS AND THERMAL TRANSPORT

### 3.4.1   Grüneisen Parameters

The lattice thermal conductivity of $\beta$-Ga$_2$O$_3$ at room temperature is strongly influenced by anharmonic phonon-phonon interactions, which are quantified by the Grüneisen parameters. We calculated the Grüneisen parameters for the acoustic and optical phonon modes to understand the origin of the low thermal conductivity of $\beta$-Ga$_2$O$_3$. The average Grüneisen parameter $\gamma$ for the acoustic modes is obtained by fitting the energy versus volume curve for hydrostatic deformation to the Murnaghan equation of state,[105] given by:

$$E(V) = E(V_0) + KV/K'[(V_0/V)^{K'}/(K'-1)+1] - (KV_0)/(K'-1), \qquad (3.2)$$

where $E$ is the total energy of the system, $K$ is the bulk modulus, $K'$ is the pressure derivative of the bulk modulus, $V$ is the system volume, and $V_0$ is the equilibrium volume. Volume values spanning a range of $\pm 20\%$ around the equilibrium were used for the fit. For hydrostatic deformation, we varied the length of the lattice vectors
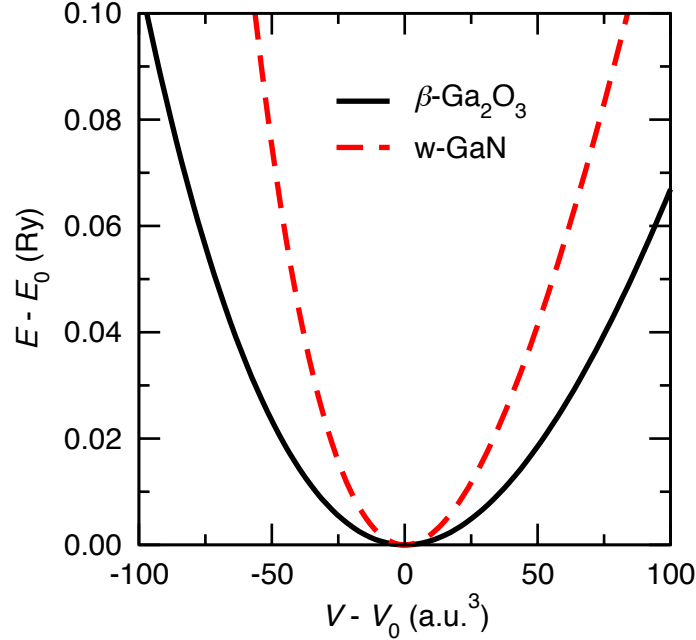
Figure 3.4: Volume-dependent total system energy data was fit to the Murnaghan equation of state was for both $\beta$-Ga$_2$O$_3$ and GaN to determine the bulk modulus and pressure derivative of the bulk modulus. The curves have been rigidly shifted by $(E\text{-}E_0)$ and $(V\text{-}V_0)$. The curvature of the fitted curves show that acoustic vibrations of $\beta$-Ga$_2$O$_3$ exhibit less anharmonicity than GaN.

to obtain the desired volume while maintaining the equilibrium cell shape, and the atomic positions were relaxed to minimize the energy of the system at each volume. From fitting to the model, $K$ is determined to be 173 GPa, and $K'$ is 3.99. The best-fit curves for the Murnaghan equation of state are shown for both $\beta$-Ga$_2$O$_3$ and wurtzite GaN for comparison in Figure 3.4.

Once the parameter $K'$ is determined, Equation (3.3) is used to calculate $\gamma$ based on the Vaschenko-Zubarev definition of the Grüneisen parameter:[106,107]

$$\gamma = K'/2 - 5/6. \tag{3.3}$$

Using the fitted $K'$ parameter from the Murnaghan equation of state, Equation (3.3) was used to calculate an average acoustic Grüneisen parameter of 1.16 for $\beta$-Ga$_2$O$_3$. Another way to obtain the experimental average acoustic Grüneisen parameter is by using Equation (3.4):

$$\gamma = \frac{9\alpha K V_m}{C_V}, \tag{3.4}$$

where $\alpha$ is the linear thermal expansion coefficient and $V_m$ is the molar volume. For

comparison, applying the same methods to wurtzite GaN yields a bulk modulus of 192 GPa, pressure derivative of 4.44, and Grüneisen parameter equal to 1.39. Since the acoustic-mode $\gamma$ for GaN is larger than that for $\beta$-Ga$_2$O$_3$, yet GaN exhibits a higher thermal conductivity, we conclude that the optical modes of $\beta$-Ga$_2$O$_3$ must have a strong impact on limiting thermal conductivity.

For the optical modes, the mode Grüneisen parameters $\gamma_i$ were calculated according to their definition:

$$\gamma_i(q) = -\frac{\partial \ln(\omega_i(q))}{\partial \ln(V)}, \tag{3.5}$$

where $\omega_i(q)$ is the frequency of phonon mode $i$ at wave vector $q$. The unit-cell volume was hydrostatically varied within $\pm 1\%$ around its equilibrium value and the atomic positions were relaxed to minimize forces on the atoms. The resulting structural parameters were subsequently used to calculate phonon frequencies.

Table 3.4 shows the calculated Grüneisen parameters for the IR-active phonon modes. Two of these values (for the two lowest frequency IR-active modes) are negative, indicating that the corresponding modes soften (frequencies decrease) as the volume decreases. This is contrary to typical behavior where modes stiffen due to stronger bonds as the crystal volume decreases. The largest mode Grüneisen parameter is 2.32, corresponding to IR-active mode #5. Other notably large Grüneisen values for the IR modes are 1.97 (mode #9), 1.34 (mode #7), 1.28 (mode #11), and 1.25 (mode #12). Since many of the phonon modes have large Grüneisen parameters, we examined the agreement of the frequencies of these modes to experimental values and whether the frequencies are affected by strong anharmonic effects. However, closer examination of the modes with the largest (and smallest) mode Grüneisen parameters does not show a correlation between the anharmonicity of a particular mode and the magnitude of the disagreement between theory and experiment.

Grüneisen parameters for the Raman-active optical phonon modes are shown in Table 3.5. Calculated and measured values reported by Machon *et al.* are included in Table 3.5 for comparison.[12] The majority of the Raman-mode Grüneisen parameters are larger than 1. Similar to the lowest IR-active phonon modes, the lowest two Raman modes have negative Grüneisen parameters. Raman modes #7, #8, and #12 exhibit the largest Grüneisen values (1.86, 1.71, and 1.60, respectively). We note that although the calculated Raman frequencies reported by Machon *et al.* are in better agreement with their experimentally-measured frequencies than are our calculations, our calculated Raman-mode Grüneisen parameters are in better agreement with their

| IR Mode | $\gamma_i$ |
|---------|-----------|
| 1 | -0.53 |
| 2 | -2.10 |
| 3 | 0.47 |
| 4 | 1.05 |
| 5 | 2.32 |
| 6 | 1.16 |
| 7 | 1.34 |
| 8 | 1.06 |
| 9 | 1.97 |
| 10 | 0.89 |
| 11 | 1.28 |
| 12 | 1.25 |

Table 3.4: Our calculated results for the Grüneisen parameters for the IR-active phonon modes of $\beta$-Ga$_2$O$_3$.

reported experimental $\gamma_i$ values than their calculations.

Grüneisen-parameter values around 1.0 are typically considered to be large, but several of the mode Grüneisen parameters $\gamma_i$ are significantly higher than the acoustic-mode $\gamma$ parameter for this material. This indicates that the optical modes rather than the acoustic modes are the main contributors to phonon anharmonicity in this material. $\beta$-Ga$_2$O$_3$ has several optical mode Grüneisen parameters that are larger than the single largest value for GaN, with the experimental optical mode Grüneisen parameters of GaN ranging from ~1.2-1.5.[108] Comparing the Grüneisen parameters for both materials indicates that the acoustic modes have the stronger impact on the thermal conductivity in GaN, while the optical modes are more impactful in $\beta$-Ga$_2$O$_3$.

### 3.4.2 Thermal Conductivity

The thermal conductivity is an important parameter that determines heat management in devices under high-power operation, as well as in applications such as thermoelectrics. In the simplest approximation, the lattice contribution $\kappa_L$ to the thermal conductivity of $\beta$-Ga$_2$O$_3$ is directly proportional to the values of the sound velocity and the heat capacity through $\kappa_L = \frac{1}{3} C_V v l$, where $l$ is the phonon mean free path in the material due to anharmonic phonon scattering. The experimental values of the thermal conductivity in $\beta$-Ga$_2$O$_3$ have been measured along different crystallographic directions and vary widely due to the anisotropy of the monoclinic crystal structure; the largest value (27 W m$^{-1}$ K$^{-1}$) occurs along the [010] direction, while the [100] direction exhibits the smallest (11 W m$^{-1}$ K$^{-1}$).[109] Rigorous first-principles

| Raman Mode | Present Work | Machon et al.[12] (Calc.) | Machon et al.[12] (Exp.) |
|---|---|---|---|
| 1 | -1.27 | 1.39 | — |
| 2 | -1.50 | -0.7 | — |
| 3 | 1.47 | 1.53 | 1.97 |
| 4 | 0.57 | 1.00 | 0.35 |
| 5 | 1.07 | 1.30 | 0.98 |
| 6 | 1.09 | 1.13 | 0.95 |
| 7 | 1.86 | 1.83 | 1.52 |
| 8 | 1.71 | 1.47 | — |
| 9 | 0.76 | 0.58 | 0.78 |
| 10 | 1.30 | 1.26 | — |
| 11 | 1.44 | 1.14 | 1.27 |
| 12 | 1.60 | 1.70 | — |
| 13 | 1.18 | 0.8 | 1.54 |
| 14 | 1.19 | 1.39 | 1.39 |
| 15 | 1.18 | 1.23 | 1.11 |

Table 3.5: Our calculated Grüneisen parameters for the Raman-active phonon modes of $\beta$-Ga$_2$O$_3$. The calculated and measured values by Machon et al.[12] are also listed for comparison.

calculations have previously estimated the [010] direction thermal conductivity to be 21 W m$^{-1}$ K$^{-1}$.[94] These thermal-conductivity values are much lower than those of other power electronic materials such as GaN ($\sim$130 W m$^{-1}$ K$^{-1}$) and SiC ($\sim$500 W m$^{-1}$ K$^{-1}$).[20] We attribute the low thermal conductivity of $\beta$-Ga$_2$O$_3$ to the large values for $\gamma_i$ (e.g., for IR-active modes #5, #9, #7, #11, and #12 and Raman-active modes #7, #8, and #12) and, in particular, to IR-active mode #5 ($\omega = 303.17$ cm$^{-1}$) with the largest mode Grüneisen parameter of 2.32.

## 3.5 ELECTRON-PHONON COUPLING, MOBILITY, AND DIELECTRIC BREAKDOWN

### 3.5.1 Electron-Phonon Coupling Matrix Elements

We studied electron-phonon interactions in $\beta$-Ga$_2$O$_3$ to gain a fundamental understanding of how they impact the electron transport properties relevant for power electronics. We evaluated the electron-phonon coupling matrix elements between states at $\Gamma$ and at several points along each reciprocal lattice direction in increments of $0.1|b_j|$. Figure 3.5 shows these electron-phonon coupling matrix elements for the bottom con-

duction band as a function of the phonon wave vector. Figure 3.5 also displays the magnitude of the phonon-absorption ($g^2(q)n_q$) and phonon-emission ($g^2(q)(n_q+1)$) contributions of each phonon mode to the mobility, where $n_q$ are the phonon occupation numbers given by the Bose-Einstein distribution:

$$n_q = (e^{\frac{\hbar\omega(q)}{k_B T})-1})^{-1} \tag{3.6}$$

evaluated at 300 K ($k_B T = 25.85$ meV). For clarity, the plots in Figure 3.5 only include the modes that have the top three largest values for either the matrix element squared, phonon-absorption, or phonon-emission terms along each direction. Note that the phonon frequencies given in Figure 3.5 correspond to the frequencies of the modes at the calculated wave vectors q closest to, rather than at, $\Gamma$ since these are the specific wave vectors used in Equations (3.6) and (3.7).

As in polar materials in general, the phonon modes that dominate electron-phonon coupling in $\beta$-Ga$_2$O$_3$ are the polar LO phonon modes[110] and show a diverging behavior as $q \rightarrow 0$. The interaction of electrons with the polar LO phonons is described by the Fröhlich expression of the general form:

$$g^2_{i,b_j}(q) = C_{i,b_j}/q^2 \tag{3.7}$$

for each phonon mode $i$ and wave vector $q$ along each reciprocal lattice vector direction $b_j$. We determined the numerators $C$ from the calculated matrix elements for the wave vectors closest to $\Gamma$ along each direction. Table 3.6 contains the calculated values of $C$ for the top several phonon modes with the largest phonon-absorption and emission values. The $C$ values are used to estimate the breakdown field of $\beta$-Ga$_2$O$_3$ in Section 3.5.3.

The majority of the dominant phonon modes with respect to electron-phonon interactions have high phonon frequencies. Among them the mode with the lowest frequency has a value of 235 cm$^{-1}$. Notably, the energy of this phonon mode (29 meV) is very near that of $k_B T$ at room temperature (26 meV), which indicates that this mode has a high occupation number at room temperature. For all three directions, the highest frequency modes have the largest Fröhlich model $C$ coefficients, and the largest $C$ values occur along reciprocal lattice directions $b_3$ and $b_1$ (1091 meV$^2$/a$_0{}^2$ and 1074 meV$^2$/a$_0{}^2$, respectively). The coefficient values tend to decrease with decreasing phonon frequency.
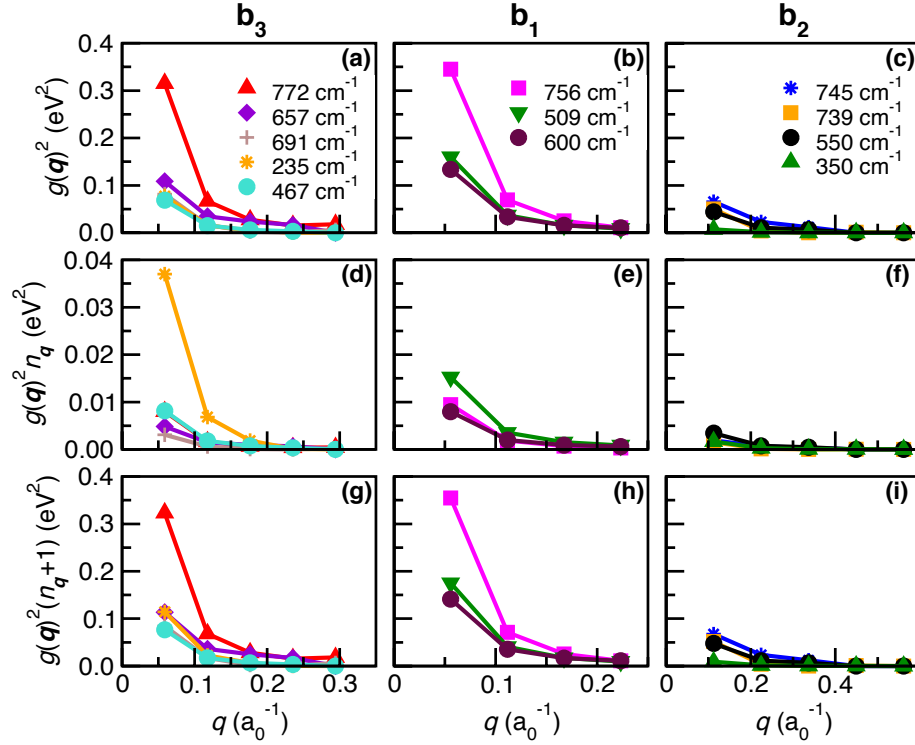
Figure 3.5: The square of the intraband electron-phonon coupling matrix elements $g^2$ for the bottom conduction band of $\beta$-Ga$_2$O$_3$ between $\Gamma$ and $q$ along the three reciprocal lattice directions (a)-(c). The dominant modes for the phonon-absorption (d)-(f) and phonon emission (g)-(i) terms are also plotted for comparison. The legends denote the calculated phonon frequency for each mode at the wave vector included closest to $\Gamma$. Although the mode at 235 cm$^{-1}$ does not yield the strongest matrix element $g^2$, it dominates the phonon-absorption term $(g^2 n)$ due to its low frequency (and associated large phonon occupation number) and limits the electron mobility at room temperature.

43

| Reciprocal Lattice Direction | Phonon Frequency ($cm^{-1}$) | Fröhlich Model $C$ Coefficient ($meV^2/a_0{}^2$) |
|:---:|:---:|:---:|
| $\boldsymbol{b}_1$ | 261 | 40 |
| | 275 | 65 |
| | 509 | 498 |
| | 600 | 416 |
| | 756 | 1074 |
| $\boldsymbol{b}_2$ | 335 | 32 |
| | 350 | 93 |
| | 550 | 559 |
| | 572 | 119 |
| | 739 | 634 |
| | 745 | 826 |
| $\boldsymbol{b}_3$ | 235 | 268 |
| | 467 | 238 |
| | 657 | 376 |
| | 691 | 282 |
| | 772 | 1091 |

Table 3.6: The $C$ coefficients for the Fröhlich model for the dominant phonon modes are shown. The coefficients were calculated using the electron-phonon coupling matrix elements $g$ calculated at the wave vector closest to $\Gamma$ for each direction ($0.1 \times \boldsymbol{b}_j$) with Equation (3.7).

### 3.5.2   Origin of Mobility Limit

Our results for the electron-phonon coupling matrix elements enable us to identify the limiting factors to the room-temperature mobility and interpret experimental results. The modes that couple strongest to electrons along each direction are the highest-frequency ones (772 cm$^{-1}$ along $b_3$, 756 cm$^{-1}$ along $b_1$, and 745 cm$^{-1}$ along $b_2$). Those modes dominate phonon emission and, as discussed in Section 3.3.3, play an important role in determining the dielectric-breakdown properties. For low-field transport, however, the thermal energy of electrons ($\sim k_B T$) is insufficient to cause electron scattering by the emission of those high-frequency phonons. Hence we turn our attention to those phonon modes that couple strongly to electrons yet have an energy that is sufficiently low (on the order of $k_B T$ or less) that allows them to be emitted by thermal electrons. The low-energy modes also have large phonon occupation numbers that facilitate electron scattering by phonon absorption. Of all the modes that dominate electron-phonon coupling, the mode with frequency 235 cm$^{-1}$ has a phonon energy (29 meV) close to $k_B T$ at room temperature (26 meV). The next lowest-energy mode that couples strongly to electrons has a frequency of 350 cm$^{-1}$ (43 meV). Despite having a lower $g^2(q)$ value than many of the other dominant modes, the 29 meV mode exhibits the largest contribution to the phonon-absorption term of electron-phonon coupling out of all modes for all three directions. The value of the phonon-emission term for the 29 meV mode is also comparable to the dominant high-frequency modes, yet its low energy allows those phonons to be emitted by thermal electrons and cause scattering. Therefore, our electron-phonon coupling results identified this particular phonon mode at 235 cm$^{-1}$ (29 meV) to likely be one of the fundamental intrinsic limitations of the electron mobility of $\beta$-Ga$_2$O$_3$ at room temperature. Our results also show that the highest mode, despite having large electron-phonon coupling matrix elements, does not dominate electron-phonon scattering due to the small activation of this mode at room temperature.

Our results agree with previously reported values for the frequency of the PO phonon mode that limits the room-temperature mobility (21 meV and 44 meV).[91,92] Hall-effect measurements by Ma *et al.* found that, for doping densities $< 10^{18}$ cm$^{-3}$, the electron mobility is intrinsically limited by phonons to $< 200$ cm$^2$ V$^{-1}$ s$^{-1}$ at 300 K.[91] The authors also estimated the dimensional Fröhlich coupling constant ($\alpha_F$) to be almost three times stronger than that of GaN. The atomistic origin behind the stronger electron-phonon scattering in Ga$_2$O$_3$ is the low symmetry of the crystal structure, which hosts low-energy polar optical modes. The lack of such low-frequency modes leads to a higher intrinsic electron mobility in GaN than $\beta$-Ga$_2$O$_3$.

### 3.5.3 Dielectric Breakdown

We applied our calculated electron-phonon coupling matrix elements to estimate the intrinsic breakdown electric field of $\beta$-Ga$_2$O$_3$ following to the first-principles methodology developed by Sun *et al.*[46] The breakdown-field value $V_{br}$ is estimated according to:

$$V_{br} = max[\frac{\sqrt{3m}}{e}\sqrt{\frac{1}{\tau(E)}B(E)}], E \in CBM, CBM + E_g \tag{3.8}$$

for $E_{CBM} \leq E \leq E_{CBM} + E_g$, where $E_g$ is the experimental band gap of $\beta$-Ga$_2$O$_3$ (4.5 eV), $m$ is the electron mass, $e$ is the electron charge, $\tau(E)$ is the electron relaxation time, and $B(E)$ is the net rate of energy loss. $\tau(E)$ is given by Equation (3) in Ref. 46 and is evaluated by summing over the probabilities of electronic scattering to all possible final states (Fermi's golden rule) and represents the time it takes for a single electron to independently relax from a certain energy to another. $B(E)$ is given by Equation (6) in Ref. 46 and is calculated similarly to $\tau(E)$ but accounts for energy exchanges between electrons and phonons either through phonon absorption or emission. Complete details for this method are described in the work by Sun *et al.*[46] $V_{br}$ is calculated in an energy range equal to the energy of the band gap, starting from the bottom of the CBM to $E_g$ higher in the conduction band(s). This limit is set by assuming that once an electron reaches energies higher than the band gap, impact ionization will occur at a rate of 100%. This assumption holds for a material sample with infinite size. Practical devices, however, have a finite channel length, and thus not all electrons that reach this energy impact ionize within the time that they cross the device. Therefore, the breakdown field in devices can be higher than our estimate for the bulk intrinsic material, and its analysis requires impact ionization coefficients of electrons such as those calculated by Ghosh and Singisetti.[111] To determine the breakdown field, we applied our previously calculated GW band structure[78] and the fitted Fröhlich parameters $C$ (see Table 3.6) for the electron-phonon coupling matrix elements to evaluate the scattering time and energy loss rate as a function of the electron energy above the conduction band minimum, similar to Ref. 112. We assumed screening by a carrier concentration of $10^{16}$ cm$^{-3}$ and a temperature of 300 K. We considered the contributions by the dominant phonon modes, which altogether account for approximately 80% of the total magnitude of the electron-phonon interaction.

The argument of the max function on the right-hand side of Equation (3.8) is

plotted as a function of energy in Figure 3.6. The maximum values of the function for electron energies between the conduction-band minimum and an energy equal to the gap higher (4.5 eV) are 4.8, 5.5, and 5.9 MV/cm along the $b_1$, $b_2$, and $b_3$ directions, respectively, which correspond to a directionally-averaged breakdown field of 5.4 MV/cm. This result was obtained considering only the dominant LO phonon modes, which account for $\sim$80% of the total electron-phonon coupling magnitude along each direction. Multiplying the estimated breakdown field by a factor of 1.25 to extrapolate and account for the total electron-phonon interaction magnitude, we arrive at a breakdown-field value of 6.8 MV/cm. This estimated value is smaller than the earlier estimate of 8 MV/cm by Higashiwaki $et$ $al.$ based on the universal trend established by wide-band-gap semiconductors and assuming a gap value of 4.9 eV,[52] which at the time was the accepted gap value of $\beta$-Ga$_2$O$_3$. However, the value predicted using this trend is 6.3 MV/cm once the correct room-temperature gap value of 4.5 eV from Ref. 58 is considered, which agrees with our calculated result within $\sim$0.5 MV/cm. Our results, therefore, agree with the estimated range of values for the breakdown field of 6-8 MV/cm for a band-gap range of 4.5-4.9 eV reported in recent work by Sasaki $et$ $al.$[90]

In a recent review, Stepanov $et$ $al.$[89] used the empirical relationship developed by Hudgins $et$ $al.$[113] to estimate the breakdown field of $\beta$Ga$_2$O$_3$ and reported a value over 8 MV/cm. The authors used a band-gap value of 4.85 eV and the empirical relationship for a direct-gap material [$V_{br} = 1.73\times10^5(E_g^{2.5})$] rather than an indirect-gap material [$V_{br} = 2.38\times10^5(E_g^2)$], where $V_{br}$ has units of V/cm and $E_g$ is in eV, citing that the small energy difference between the direct and indirect gaps and the weakness of the indirect transitions essentially make Ga$_2$O$_3$ behave as a direct-gap material. If the band gap value of 4.5 eV is used, the Hudgins $et$ $al.$ empirical relationships predict breakdown fields of $\sim$7.4 MV/cm (direct band gap) or $\sim$4.8 MV/cm (indirect band gap), and the direct-gap estimate agrees well with our reported value of 6.8 MV/cm.

Our estimated breakdown field of $\beta$-Ga$_2$O$_3$ is lower than previous estimates and calls for a re-examination of the prospects of $\beta$-Ga$_2$O$_3$ for high-power electronic devices. Baliga's figure of merit (BFOM) depends on the breakdown field ($V_{br}$) to the third power at low frequencies (BFOM $= \epsilon\mu V_{br}^3$).[44,45] Previous estimates by Higashiwaki $et$ $al.$ assumed a breakdown field of 8 MV/cm and reported a BFOM at low frequencies for GaN and $\beta$-Ga$_2$O$_3$ as 870 and 3,444 relative to Si, respectively.[52] Our new estimate of 6.8 MV/cm reduces the BFOM for $\beta$-Ga$_2$O$_3$ to $\sim$2,115 ($\sim$1.6 times lower) at low frequencies. Additionally, the value used for mobility in the previous
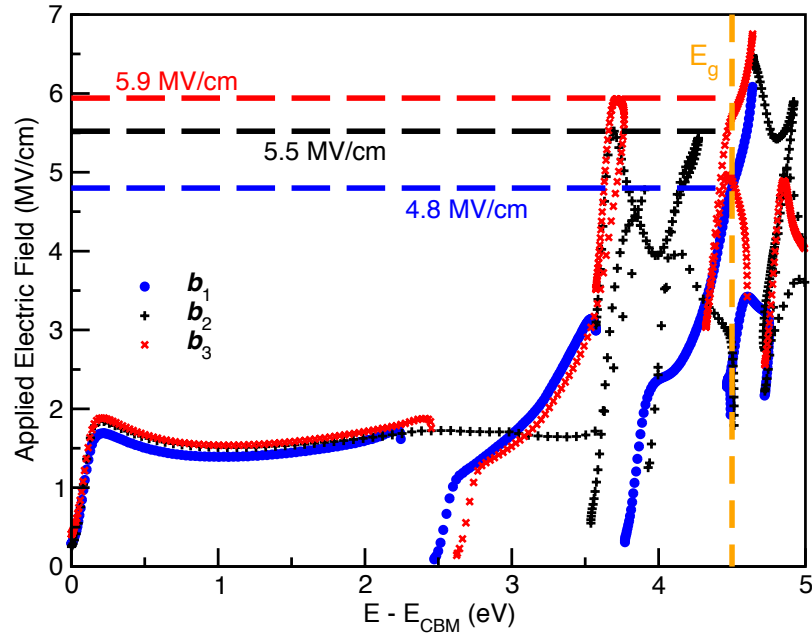
Figure 3.6: Calculated estimate of the breakdown field of $\beta$-$Ga_2O_3$ along each reciprocal-lattice vector direction. The estimated values account only for electron scattering by the longitudinal optical phonon modes, which amount for $\sim 80\%$ of the total electron-phonon interaction. The experimental band-gap value of 4.5 eV is used for the upper limit of the electron energies. The calculated directionally averaged breakdown field is 5.4 MV/cm and is corrected to 6.8 MV/cm if extrapolated to account for the remaining 20% of the total electron-phonon interaction strength.

report was 300 cm$^2$ V$^{-1}$ s$^{-1}$, which is actually an extrapolated experimental value.[23] However, recent reports in the literature place it in a lower range around $\sim$200 cm$^2$ V$^{-1}$ s$^{-1}$.[75,81,91,114,115] Assuming a mobility of 200 cm$^2$ V$^{-1}$ s$^{-1}$ and a breakdown field of 6.8 MV/cm, the low-frequency BFOM of Ga$_2$O$_3$ is $\sim$1,410 relative to Si, which is still 1.6 times greater than that of GaN. Despite the lower breakdown-field estimate (6.8 MV/cm) in combination with the lower mobilities recently measured, $\beta$-Ga$_2$O$_3$ still shows superior performance for power electronics compared to GaN.

Increasing the band gap even slightly by, *e.g.*, alloying or strain[116], is a promising method to increase the breakdown field and the BFOM. From Figure 3.6, for an energy equal to that of the conduction band minimum plus 4.5 eV (the experimental $E_g$), the average breakdown field is estimated to be 5.4 MV/cm, with values of 4.8, 5.5, and 5.9 MV/cm along the $b_1$, $b_2$, and $b_3$ directions, respectively. Increasing the band gap to 4.7 eV causes a 20% increase in the average breakdown field estimate (6.5 MV/cm), with direction-dependent values of 6.1, 6.5, and 6.8 MV/cm along the $b_1$, $b_2$, and $b_3$ directions. Accounting for the remaining 20% of the electron-phonon interaction would raise this value to $\sim$8.1 MV/cm, bringing the breakdown field estimate to the original estimate of 8 MV/cm. Possible methods to realize the larger band gap include strain engineering or alloying with aluminum. The latter of which has already been demonstrated, and a band gap range from 5.2-7.1 eV was measured when using 24%-100% Al.[117] For applications in high-power electronics, future work should be done to improve the breakdown field of $\beta$-Ga$_2$O$_3$ by increasing the band gap as well as increasing the electron mobility and thermal conductivity.

## 3.6   CONCLUSIONS

In summary, we investigated the phonon properties, phonon-phonon interactions, and electron-phonon scattering of $\beta$-Ga$_2$O$_3$ in the anisotropic monoclinic crystal. We derived the directionally dependent phonon dispersion curves, LO-TO splittings, sound velocities and found good agreement with experiment. Oxygen substitution by O$^{15}$ has the largest isotopic effects on the phonon frequencies. Our calculated Grüneisen parameters indicate that the optical modes show stronger anharmonicities than the acoustic ones and suppress the thermal conductivity of $\beta$-Ga$_2$O$_3$. We also determined that the low-symmetry crystal structure gives rise to a low-frequency polar-optical mode with a phonon energy of 29 meV that dominates electron scattering at room temperature and limits the mobility. Our value for the breakdown field of $\beta$-Ga$_2$O$_3$ is 6.8 MV/cm, which is in good agreement with empirical estimates that

use the revised band-gap value of 4.5 eV. We validate that $\beta$-Ga$_2$O$_3$ has a higher Baliga FOM compared to GaN. Our results identify the microscopic origins of the thermal and electron transport limits in $\beta$-Ga$_2$O$_3$ and propose strategies to increase the breakdown field to 8 MV/cm by increasing the band gap either by growth under strain or by alloying with Al$_2$O$_3$.

# CHAPTER IV

# Impact of the Stacking Sequence on the Band Gap and Luminescence Properties of Bulk, Bilayer, and Monolayer Hexagonal Boron Nitride

We examine the effects of stacking sequence and number of layers on the electronic and luminescence properties of hexagonal boron nitride structures with first-principles calculations based on density functional and many-body perturbation theory. We explored the variations of the magnitude and character (direct or indirect) of the quasiparticle band gap and interband optical matrix elements for bulk, bilayer, and monolayer stacking polytypes. Although the fundamental gap for most structures is indirect, phonon-assisted transitions are strong (typically 600 times stronger than bulk Si) and enable efficient deep-UV luminescence. The polarization of the emitted light is transverse electric, which facilitates light extraction perpendicularly to the h-BN basal plane. Random stacking in turbostratic BN breaks the crystal symmetry and enables optical transitions across the quasi-direct band gap, albeit with a weak matrix element. Our results demonstrate that h-BN is a promising material for efficient deep-UV light emitters.

## 4.1 INTRODUCTION

Hexagonal boron nitride (h-BN) is a light-emitting wide-band-gap semiconductor that has sparked significant interest for optoelectronic applications in the deep-ultraviolet part of the spectrum. Previous studies show that its luminescence properties are strongly influenced by excitonic[118–121] and phonon-assisted[119] effects, as well as its structural characteristics at the atomistic level. With a honeycomb-like structure similar to graphene, h-BN is connected by strong covalent bonds within the plane and weak van der Waals attraction between the planes. Experimental studies[122] have

51

demonstrated that the layers can be stacked in five stacking sequences enumerated in Figure 4.1. In the most stable structure (AA'), the hexagonal rings sit directly on top of each other, with B and N atoms alternating along the $c$-axis. In the AA stacking, the B atoms sit directly on top of B and N directly on top of N along $c$. In $AB_1$, $AB_2$, and $AB_3$ one layer is shifted within the basal plane so that half of the atoms sit on top of the empty hexagon centers. The h-BN stacking sequence has a strong effect on its electronic structure and provides an adjustable parameter to engineer the luminescence properties.[120–124] In addition, stacking faults and other deformations may occur and yield disordered stacking sequences.[121,123,125] *E.g.*, Bourrellier *et al.* characterized h-BN flakes via high resolution transmission electron microscopy and high angle annular dark field imaging (HAADF) and observed faceted double folds in the BN crystal with bended layers, crystal layer glides, and antiphase boundaries.[121] These deformations lead to $AB_1$ or $AB_2$ stackings along the bended regions and AA or $AB_3$ at the antiphase boundaries. Similarly, Warner *et al.* used high-resolution transmission electron microscopy to show that both AA' and AB stacking occur in BN bilayers.[123] The stacking sequence may also be random to form turbostratic boron nitride (t-BN).

Although the stacking sequence has only a minor effect on the total energy, it substantially impacts the overlap of atomic orbitals between adjacent planes and hence the electronic structure. Theoretical results show that the AA' stacking is the energetically most favorable, yet the energy differences between the various polytypes are small. *E.g.*, Constantinescu *et al.* used local second-order Møller-Plesset perturbation theory (LMP2) to compute the energy differences in the five stacking types both in bulk and bilayer form.[125] They found that the AA' and $AB_3$ stacking sequences have the lowest total energies (differing by only 0.4 meV per atom for the bulk and 0.1 meV per atom for the bilayer). This result agrees with predicted interlayer potential energy plots and coincides well with the most commonly seen sequences in experiment.[122] An investigation of the variation of the band gap as a function of increasing number of layers in addition to stacking sequence can be found in, *e.g.*, Ref. 126. Despite small energy differences, the stacking sequence has important effects on the electronic and optical properties. Sponza *et al.* calculated the band structures for the AA' and $AB_3$ structures with many-body perturbation theory (GW) and found that AA' ($AB_3$) stacking has an indirect gap of 5.80 eV (6.01 eV) and a smallest direct gap of 6.28 eV (6.13 eV).[120] Density functional theory (DFT), GW, and Bethe-Salpeter Equation (BSE) calculations by Bourellier *et al.* also show that the band gaps and exciton binding energies for the different h-BN polytypes vary to a notable extent.[121]

Figure 4.1: (top row) Crystal structures of the five possible stacking types of h-BN organized from thermodynamically most stable (left) to least stable (right) and their respective GW band structures for (middle row) bulk and (bottom row) bilayer structures.

For instance, the lowest exciton binding energy of AA' stacking is 5.75 eV, while that of the remaining four stacking types ranges from 5.2 eV ($AB_1$) to ~5.9 eV ($AB_3$). Luminescence in bulk h-BN (AA' stacking only) was recently explored by Cannuccia *et al.* using non-equilibrium Green's functions and time-dependent perturbation theory, taking into account phonons and excitonic effects.[127] They find that the peaks in the luminescence spectrum are split firstly into doublets due to LO-TO splitting and secondly, to a smaller degree, by excitons. Sponza *et al.* investigated the optical properties of various BN polymorphs (monolayer, AA', $AB_3$, and rhombohedral ABC stacking) with a focus on direct and indirect excitons, however, phonons were not taken into account.[120] The stacking sequence of h-BN has a significant impact on excitonic effects in the optical absorption spectrum as noted previously.[121]

Theoretical contributions have helped to explain the experimental luminescence of h-BN despite its indirect band gap, specifically with the help of phonons and/or excitons. However, many theoretical studies include only a small subset of the possible h-BN structures, or examine the band structures on the DFT level only, which severely underestimates the band gap. In this work, we investigate the effect of stacking sequence and quantum confinement on the quasiparticle band structures of h-BN. Our analysis includes the monolayer, all five possible stacking sequences of bulk and bilayer, as well as the randomly stacked t-BN. We examine the effect of stacking sequence on the character (direct/indirect) and magnitude of the band gap, as well as on the interband optical matrix elements. We find that most of the examined structures have indirect band gaps, yet the phonon-assisted optical matrix elements are strong and transverse-electric (TE) polarized. Our results reveal that the electronic and optical properties of h-BN can be engineered by controlling the number and stacking sequence of the atomic layers.

## 4.2   COMPUTATIONAL METHODS

Our first-principles calculations are based on density functional theory (DFT) and many-body perturbation theory. The studied h-BN polytypes include the five possible bulk and bilayer stacking sequences (Figure 4.1), the monolayer, and randomly stacked bulk t-BN.[128] Sufficient vacuum space was included in the out-of-plane direction of the few-layer structures to contain at least 99% of the charge density in half the unit cell. All structures were relaxed including van der Waals interactions with the optB86b-vdw functional[129–131] in VASP[99,100,132,133] until the stress of the bulk and in-plane stress of the few-layer structures were less than |0.5| kbar. The

relaxed structures were then used in the Quantum ESPRESSO code[62] to perform the band-structure calculations within the local-density approximation (LDA) and the GW method. A plane wave energy cutoff of 70 Ry converges the total system energy within 1 mRy/atom. The Brillouin zone (BZ) was sampled with a 24×24 grid within the plane and 24 (bulk AA), 12 (bulk AA', $AB_3$, $AB_1$, and $AB_2$), 2 (bulk t-BN), or 1 (bilayer and monolayer structures) points along the out-of-plane direction to achieve approximately even sampling for all structures. We then calculated quasiparticle energies with the $G_0W_0$ method and the BerkeleyGW software.[63,64,70] We employed the generalized plasmon-pole model,[64] the static-remainder approach,[70] and truncation of the long-ranged Coulomb interaction[134] for the monolayer and the bilayers. A screened Coulomb cutoff energy of 30 Ry was used for all structures. For the bulk structures, ∼700 bands are used for the dielectric function and ∼800 bands for the self-energy calculations. These numbers increase to ∼2,500 and ∼1,500 bands, respectively, for bilayer structures and ∼4,000 and ∼3,000 bands, respectively, for the monolayer. The BZ sampling grids for the $G_0W_0$ calculations are 12×12 in-plane and 12 (bulk AA), 6 (bulk AA', $AB_3$, $AB_1$, and $AB_2$), or 1 (bilayer and monolayer structures) out-of-plane. These parameters converge the electronic transition energies at high-symmetry k-points within 0.1 eV. The eigenenergies of the t-BN structures were corrected with a scissor shift, using parameters obtained by averaging the scissor-shift parameters of the five bulk, ordered BN polytypes. We subsequently applied the maximally localized Wannier function method[65] with the Wannier90 code[66] to obtain the band structures on finer BZ grids. We also calculated the interband velocity matrix elements (VMEs) (Ref. 135) for transitions from the top valence band to the bottom conduction band at the BZ locations of the valence band maximum (VBM), the conduction band minimum (CBM), and the smallest direct gap to determine the intensity of optical transitions. For the indirect-band-gap BN structures, we also calculated the generalized phonon-assisted optical matrix elements ($S^2$) according to:[136]

$$S^2 = \frac{v_{VBM}^2 g^2}{(\Delta E_C + \hbar\omega_{LO})^2} + \frac{v_{CBM}^2 g^2}{(\Delta E_V + \hbar\omega_{LO})^2}, \tag{4.1}$$

where $v$ is the VME at the VBM and CBM k-points, $g$ is the electron-phonon coupling matrix element between the VBM and CBM k-points as calculated with the Fröhlich model, $\Delta E_C$ ($\Delta E_V$) is the energy difference in the bottom conduction (top valence) band between the CBM and VBM k-points, and $\hbar\omega_{LO}$ is the energy of the highest longitudinal-optical phonon mode. The electron-phonon coupling constant $g^2$ was calculated for each structure with the expression:

$$g^2 = 2\pi\hbar\omega_{LO}\frac{1/\epsilon_\infty - 1/\epsilon_0}{V_{cell}q^2}, \tag{4.2}$$

where $V_{cell}$ is the total unit cell volume and $q$ is the magnitude of the vector connecting the VBM and CBM in reciprocal space. This model includes only the highest frequency longitudinal-optical mode, which has been shown to dominate in polar materials.[110] The material parameters needed for this calculation for each structure are given below in Table 4.1. For each structure, the wave vector (and its magnitude) that connects the VBM and CBM $k$-points was determined. Since h-BN is an anisotropic material, the value for the dielectric constant depends on direction. Both the static and high-frequency dielectric constants were determined with a weighted average of the in-plane and out-of-plane components of the $q$-vector determined above. The values used for the dielectric constants in this averaging were $\epsilon_{0,\|c} = 5.06$, $\epsilon_{0,\perp c} = 6.85$, $\epsilon_{\infty,\|c} = 4.10$, and $\epsilon_{\infty,\perp c} = 4.95$.[137] We considered bulk $AB_1$ to have a fundamental direct gap. Since the energy of the highest longitudinal-optical phonon mode ($\hbar\omega_{LO}$) should not vary drastically between the structures, we used the value for bulk AA' stacking from Ref. 35 for all structures.

Table 4.1 also lists the values for the electron-phonon coupling matrix element squared, the energy difference between the bottom conduction band between the CBM and VBM $k$-points, and the energy difference in the top valence band between the CBM and VBM $k$-points. Since bulk $AB_1$ has a direct gap, the value for the electron-phonon coupling matrix element is substantially larger than that of the indirect-gap polytypes, and the energy differences at those bands between the VBM and CBM $k$-points are very small. For this polytype, we determined the value for the optical matrix element at the K point where the direct gap is located using the equation for a direct-gap transition.

## 4.3 RESULTS AND DISCUSSION

### 4.3.1 Structural Properties

For the ordered, bulk structures, the five stacking types show minute differences in total energy per formula unit with respect to AA' (0.00 eV for $AB_3$ and $AB_1$ and 0.03 eV for $AB_2$ and AA). For the t-BN structures, the average difference is 0.01 eV per formula unit. The bilayer structures have even larger relative energies, between 0.07-0.09 eV per formula unit. This indicates that bulk t-BN is more stable than bulk AA and $AB_2$ and even more stable than all of the ordered, bilayer structures. Our relative

| Structure | $v_{VBM}$ | $v_{CBM}$ | $g^2$ ($\times 10^{-5}$ Ha) | $\Delta E_C$ (eV) | $\Delta E_V$ (eV) | $\hbar\omega_{LO}$ |
|---|---|---|---|---|---|---|
| bulk | | | | | | |
| AA' | 0.915 | 0.011 | 6.33 | 0.676 | 0.465 | 0.20 |
| $AB_3$ | 0.012 | 0.147 | 4.49 | 0.247 | 0.723 | 0.20 |
| $AB_1$ | 0.879 | 1.004 | 319.73 | 0.097 | 0.045 | 0.20 |
| $AB_2$ | 0.715 | 0.014 | 5.19 | 0.811 | 0.911 | 0.20 |
| AA | 1.075 | 1.260 | 5.01 | 2.012 | 1.920 | 0.20 |
| T1 | 0.025 | 0.025 | — | 0 | 0 | 0.20 |
| T2 | 0.018 | 0.018 | — | 0 | 0 | 0.20 |
| T3 | 0.014 | 0.004 | 1.08 | 0.049 | 0.806 | 0.20 |
| T4 | 0.028 | 0.027 | 1.07 | 0.049 | 0.865 | 0.20 |
| T5 | 0.046 | 0.046 | — | 0 | 0 | 0.20 |
| bilayer | | | | | | |
| AA' | 1.034 | 0.038 | 2.91 | 0.253 | 0.729 | 0.20 |
| $AB_3$ | 0.213 | 0.189 | 0.67 | 0.162 | 1.847 | 0.20 |
| $AB_1$ | 1.048 | 1.104 | — | 0 | 0 | 0.20 |
| $AB_2$ | 0.928 | 0.002 | 2.69 | 0.384 | 0.953 | 0.20 |
| AA | 0.005 | 0.005 | — | 0 | 0 | 0.20 |
| monolayer | | | | | | |
| | 1.595 | 0.267 | 0.45 | 0.263 | 1.868 | 0.20 |

Table 4.1: The material parameters for the calculation of the generalized phonon-assisted optical matrix elements $S^2$ as given by Equation (4.1) for the indirect-gap structures. These values include the interband velocity matrix element ($v$) at the VBM and CBM $k$-points, the electron-phonon coupling matrix element squared ($g^2$) between the VBM and CBM $k$-points as calculated with the Fröhlich model, the energy difference in the bottom conduction band between the CBM and VBM k-points ($\Delta E_C$), the energy difference in the top valence band between the CBM and VBM $k$-points ($\Delta E_V$), and the energy of the highest longitudinal-optical phonon mode ($\hbar\omega_{LO}$).

| Structure | Relative energy per formula unit (eV) | $|\vec{a}|$ (Å) | $|\vec{c}|$ (Å) | Average interplanar distance (Å) |
|---|---|---|---|---|
| bulk | | | | |
| AA' | 0.00 | 2.51 | 6.47 | 3.24 |
| $AB_3$ | 0.00 | 2.51 | 6.46 | 3.23 |
| $AB_1$ | 0.00 | 2.51 | 6.52 | 3.26 |
| $AB_2$ | 0.03 | 2.51 | 6.93 | 3.46 |
| AA | 0.03 | 2.51 | 7.00 | 3.50 |
| T1 | 0.02 | 2.51 | 33.84 | 3.38 |
| T2 | 0.01 | 2.51 | 33.41 | 3.34 |
| T3 | 0.01 | 2.51 | 33.32 | 3.33 |
| T4 | 0.01 | 2.51 | 33.64 | 3.36 |
| T5 | 0.01 | 2.51 | 33.08 | 3.31 |
| bilayer | | | | |
| AA' | 0.07 | 2.51 | 13.38 | 3.29 |
| $AB_3$ | 0.07 | 2.51 | 13.38 | 3.26 |
| $AB_1$ | 0.08 | 2.51 | 13.38 | 3.32 |
| $AB_2$ | 0.09 | 2.51 | 13.38 | 3.51 |
| AA | 0.09 | 2.51 | 13.38 | 3.56 |
| monolayer | | | | |
| — | 0.14 | 2.51 | 20.07 | — |

Table 4.2: Total energies and structural information for all h-BN and t-BN structures considered in this study after structural relaxations using a van der Waals functional. The five individual t-BN structures are labelled by Tx. The total energies per formula unit are references to the bulk AA' structure.

energy comparison suggests that it is more likely for multilayers of h-BN to have turbostratic disorder than adopt the AA or $AB_2$ stacking sequence. We also find that the relaxed lattice constants vary between the different stacking types in the bulk, and the sequences with higher energies compared to AA' have larger interlayer separation. Our relaxations including van der Waals forces show the interlayer separation for AA and $AB_2$ is 8.08% and 7.05% larger than AA', respectively, $AB_1$ is 0.75% larger, but $AB_3$ is actually 0.22% smaller. The unexpected result for $AB_3$ could be due to numerical noise in structural relaxations. The in-plane lattice parameter for all four stacking types is less than 0.07% smaller than that of AA', indicating that it is not sensitive to stacking order. Table 4.2 lists the lattice vectors, average interlayer distance, and total energies for all bulk, bilayer, randomly stacked, and monolayer structures we examined.

### 4.3.2 Electronic Properties

We then determine the impact of the different stacking sequences on the band structure both for bulk and for atomically thin bilayers. Figure 4.1 shows the $G_0W_0$ band structures at energies near the CBM and VBM for all five bulk (middle row) and all five bilayer (bottom row) h-BN structures. Wider energy ranges are shown in Figure 4.2. Many qualitative characteristics are similar for all polytypes. Each band structure has multiple local band extrema, primarily at or near the $\Gamma$, M, K, L, and H for the CB and K and H for the VB. Table 4.3 summarizes the BZ locations of the VBM, CBM, and smallest direct gaps as well as whether the fundamental band gap is direct or indirect. The specific locations of the VBM and CBM are quite diverse for the bulk structures. The VBM of the most stable stacking (AA') is located near K along the K-$\Gamma$ line, and the CBM is at M. For most other bulk stacking types the band gap is also indirect. The exception is the $AB_1$ stacking, for which the gap is nearly direct at K; although the VBM is located near K along the K-$\Gamma$ line (0.625, 0.667, 0), its energy is only $\sim$24 meV higher than K, which may be due to numerical noise by the interpolation of the band structure. Overall, there does not appear to be a correlation between structural stability and band-extrema location. However, a relationship between structural stability and value of the band gap is noticeable, since the two most stable structures (bulk AA' and $AB_3$) have significantly larger band gaps (6.10 eV and 6.23 eV, respectively) than the others (ranging between 5.33-5.39 eV). For the bilayers, the VBM for most stacking types is located at K, except the AA' stacking for which it lies near K along the K-$\Gamma$ line. Both bilayer $AB_1$ and AA have direct fundamental band gaps at K, but the band gaps for the other three bilayer structures remain indirect. The band gaps for the bilayers parallel the bulk values, with the more stable AA' and $AB_3$ stackings having larger gaps (7.10 eV and 7.09 eV, respectively) than the less stable structures (6.75-6.84 eV). We conclude from our analysis that the majority of the five h-BN stacking sequences have indirect fundamental band gaps in both bulk and bilayer form, and there is a strong correlation between structural stability and the magnitude of the band gap.

### 4.3.3 Optical Properties

We also explored the variation of the direct and phonon-assisted optical matrix elements (MEs) with respect to stacking sequence. Overall, we did not observe a correlation with respect to the structural stability or the magnitude of the gap. The MEs appear to increase by a factor of $\sim$2 for the bilayers compared to bulk. AA'

**Ordered**

**Bulk**

AA'  AB₃  AB₁  AB₂  AA

Γ M K  Γ A  L H  A  L M K H

**Bilayer**

Γ  M  K  Γ

**Random**  **T1**

**Monolayer**

Γ  M  K  Γ
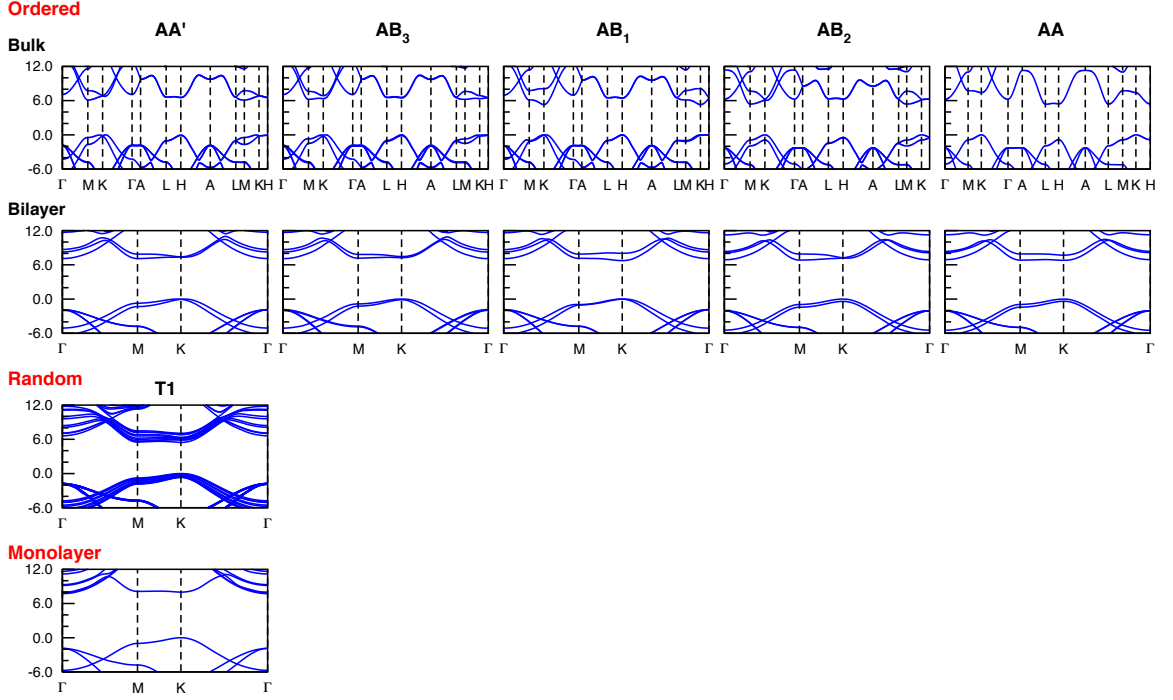
Figure 4.2: GW band structures for all five h-BN stacking sequences in bulk and bilayer in addition to one representative bulk t-BN structure (T1) and the monolayer. The energies of the bands are referenced to the valence band maximum (VBM).

| Structure | VBM location | CBM location | Smallest direct gap location | Fundamental band gap (eV) | Indirect (I) or direct (D) | Optical ME squared (a.u.) | Luminescence polarization |
|---|---|---|---|---|---|---|---|
| **Bulk** | | | | | | | |
| AA' | **K**–Γ | M | M | 6.10 | I | 0.050 | TE |
| AB₃ | H | **M**–L | K | 6.23 | I | 0.001 | TE |
| AB₁ | **K**–Γ (K) | K | K | 5.30 (5.33) | I (D) | 0.909 | TE |
| AB₂ | K | M | **K**–Γ | 5.39 | I | 0.019 | TE |
| AA | K | **L**–H | H | 5.38 | I | 0.021 | TE |
| t-BN | K | K | K | 5.44 | D | 0.001 | TE |
| **Bilayer** | | | | | | | |
| AA' | **K**–Γ | M | **K**–Γ | 7.10 | I | 0.112 | TE |
| AB₃ | K | Γ | K | 7.09 | I | 0.002 | TE |
| AB₁ | K | K | K | 6.75 | D | 1.117 | TE |
| AB₂ | K | M | **K**–Γ | 6.84 | I | 0.049 | TE |
| AA | K | K | K | 6.80 | D | 0.000 | TE |
| **Monolayer** | | | | | | | |
| — | K | Γ | K | 7.74 | I | 0.039 | TE |

Table 4.3: Band-extrema locations in the first Brillouin Zone, magnitude and character (direct or indirect) of the band gap, interband optical matrix elements (ME) (direct or phonon-assisted) of BN polytypes, and luminescence polarization (TE: transverse electric).

stacking has the strongest ME (except for the direct-gap $AB_1$ structure) and its value (0.050 a.u.) agrees with our previous calculation ($S^2 = 0.06$ a.u.) using experimental lattice parameters.[35] The ME for the $AB_3$ structure is 10-100 times smaller than the other polytypes, while the ME for the AA stacking is negligible in the bilayer. We note, however, that even the smallest generalized optical MEs in ordered bulk and bilayer h-BN polytypes are distinctly larger than typical values in other indirect-gap semiconductors (*e.g.*, $S^2 \approx 10^{-4}$ a.u. for bulk Si[138]), indicating that efficient luminescence is possible in h-BN despite its indirect gap. Moreover, the MEs for nearly all polytypes have larger components along the in-plane direction, which indicates that the deep-UV photons are primarily emitted with TE polarization (in contrast to AlN and Al-rich AlGaN alloys[139–142]), which facilitates light extraction from planar LEDs.

### 4.3.4 Monolayer BN

We also calculated the electronic properties for the h-BN monolayer to compare to the bulk and bilayer results. Interestingly, although the DFT-LDA band gap of the monolayer is direct (4.54 eV) at K (Figure 4.3(a)), GW corrections shift the CBM to $\Gamma$ and yield an indirect gap of 7.74 eV (Figure 4.3(b)). This behavior is also seen in previous GW calculations for monolayer h-BN.[143–145] Blase *et al.* showed that the self-energy correction is strongly $k$ dependent and affects states at K and M more than $\Gamma$, resulting in a reordering of conduction bands upon the GW correction. They also commented that these $\Gamma$ states are nearly-free-electron states, and, as such, their energies do not change significantly between DFT and GW.[143] We also find that GW corrections change the bottom three conduction bands at $\Gamma$. Within DFT-LDA, there is one conduction band around $\sim 4.7$ eV and two around $\sim 5.55$ eV above the VBM. After $G_0W_0$ corrections, these three conduction bands lie much closer in energy. In addition, Galvani *et al.* also noted that the transition matrix elements between the extended CBM and the localized valence band states are small.[145] Therefore, monolayer h-BN behaves essentially as a direct-gap material. Moreover, similar to the bulk and bilayer structures, the monolayer of h-BN has a rather strong optical ME (0.039 a.u.) that is nearly 400 times that of bulk Si. Our calculations therefore show that phonon-assisted optical transitions enable luminescence in nearly all ordered h-BN structures regardless of the number of layers or stacking sequence and despite their indirect gaps.
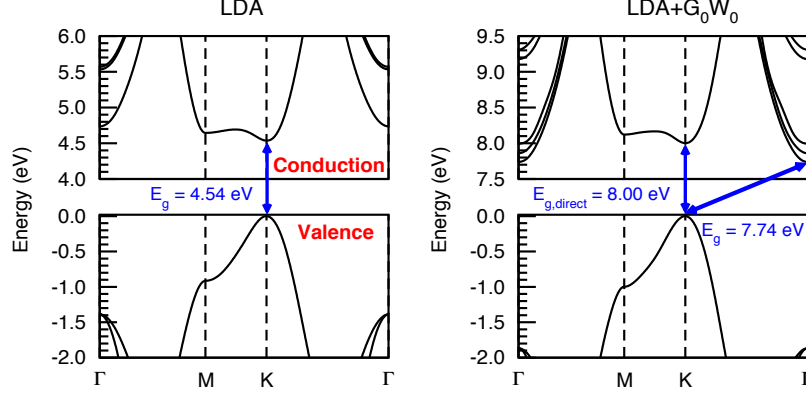
Figure 4.3: (a) DFT-LDA and (b) LDA+$G_0W_0$ band structures of monolayer h-BN.

### 4.3.5 Turbostratic BN

We further performed electronic-structure calculations for randomly stacked tur-
bostratic BN structures to uncover how stacking disorder impacts the band gap and
optical properties. We generated five different bulk t-BN structures consisting of ten
randomly chosen layers (20 atoms) each. The relaxed crystal coordinates for each of
these structures are shown in Table 4.4. One representative t-BN structure (hereafter
referred to as T1) is shown in Figure 4.4(a). Each monolayer in the t-BN structure
is arranged such that, with respect to the next monolayer out-of-plane, one of the
five possible stacking types from Figure 4.1 is adopted. We assumed that any of the
five possible stacking types between adjacent layers occurs with equal probability.
This random stacking sequence reduces the crystal symmetry and causes the gap to
become quasi-direct, with the VBM and CBM both located at K. All five tested t-BN
structures have their VBM at the K point. The CBM of three of them is at K, yield-
ing a direct gap, while the CBM for other two is located at M. However, the energy
difference between the fundamental indirect band gap and the direct gap at K for
these two t-BN structures is only 49 meV. The minimum gap (DFT + scissor shift)
for the five t-BN structures ranges from 5.25-5.51 eV (5.44 eV for T1) and is similar
to the smallest gaps of the five ordered polytypes. Despite its quasi-direct band gap,
t-BN displays a weak direct optical ME. Since the direct band gap is induced by
symmetry breaking, direct optical transitions are only weakly allowed (unlike bulk
$AB_1$, for which the direct band gap is accompanied by strong matrix elements). Our
analysis shows that even though the magnitude and character of the band gap of
h-BN can be controlled to a certain degree by introducing stacking faults, the sym-
metry breaking by the induced disorder is not expected to significantly increase the
radiative recombination rate, while it may be strongly detrimental to the transport
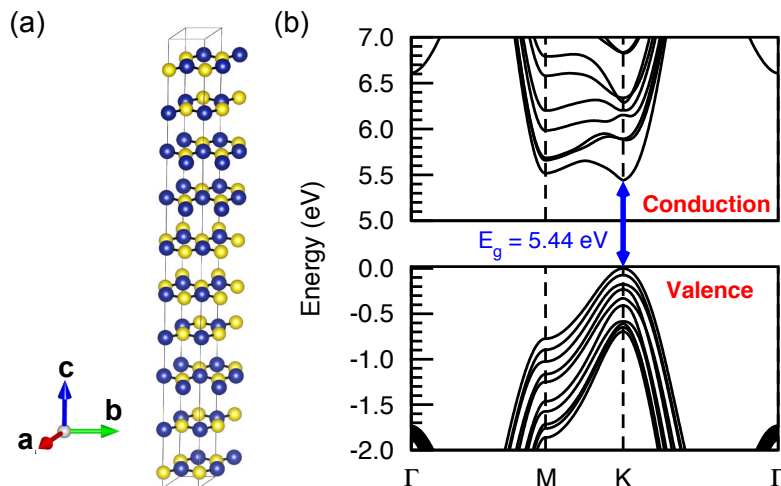
Figure 4.4: (a) Crystal structure and (b) scissor-shift-corrected band structure of a t-BN structure. B (N) atoms are represented in blue (yellow). Ten layers were randomly stacked to represent the t-BN structure with equal probability for the AA', AA, $AB_1$, $AB_2$, and $AB_3$ stacking types to occur between any two layers.

properties.

### 4.3.6 Discussion of Excitons

Our work sheds light on the radiative recombination of free carriers across the indirect band gap of h-BN polytypes. A full treatment of the luminescence properties should also consider the effect of exciton formation. We previously calculated the binding energy of the lowest-energy direct exciton in bulk AA' to be 0.83 eV,[35] which indicates that excitons are thermally stable at room temperature. Recent calculations by Sponza *et al.* find a minimum exciton binding energy of 0.30 eV and a maximum exciton binding energy of 0.67 eV.[120] An interesting feature of these calculations is that the lowest lying exciton in $AB_3$ is direct despite the material having an indirect band gap; therefore $AB_3$ should luminescence more strongly. Future work to quantify the luminescence spectra and lifetimes must consider the interplay of the strong phonon-assisted optical MEs with the direct and indirect exciton wave functions. Additional avenues to explore are the effects of substrate choice on the electronic and optical properties. For instance, a previous study on two-dimensional $MoSe_2$ showed that adding a monolayer to a bilayer graphene substrate decreased both the exciton binding energy and band gap of the material.[146]

63

| Structure | B atoms | N atoms |
|---|---|---|
| T1 | | |
| | (0.333, 0.667, 0.052) | (0.667, 0.333, 0.052) |
| | (0.667, 0.333, 0.147) | (0.333, 0.667, 0.148) |
| | (0.000, 0.000, 0.250) | (0.333, 0.667, 0.250) |
| | (0.667, 0.333, 0.352) | (0.333, 0.667, 0.352) |
| | (0.667, 0.333, 0.449) | (0.000, 0.000, 0.449) |
| | (0.667, 0.333, 0.552) | (0.000, 0.000, 0.552) |
| | (0.000, 0.000, 0.647) | (0.333, 0.667, 0.647) |
| | (0.000, 0.000, 0.750) | (0.333, 0.667, 0.750) |
| | (0.667, 0.333, 0.853) | (0.333, 0.667, 0.853) |
| | (0.333, 0.667, 0.948) | (0.667, 0.333, 0.948) |
| T2 | | |
| | (0.667, 0.333, 0.050) | (0.000, 0.000, 0.050) |
| | (0.000, 0.000, 0.146) | (0.333, 0.667, 0.146) |
| | (0.667, 0.333, 0.249) | (0.333, 0.667, 0.249) |
| | (0.667, 0.333, 0.353) | (0.333, 0.667, 0.353) |
| | (0.333, 0.667, 0.449) | (0.667, 0.333, 0.449) |
| | (0.333, 0.667, 0.553) | (0.667, 0.333, 0.553) |
| | (0.000, 0.000, 0.651) | (0.333, 0.667, 0.651) |
| | (0.667, 0.333, 0.749) | (0.000, 0.000, 0.749) |
| | (0.667, 0.333, 0.847) | (0.333, 0.667, 0.847) |
| | (0.667, 0.333, 0.952) | (0.333, 0.667, 0.952) |
| T3 | | |
| | (0.000, 0.000, 0.053) | (0.333, 0.667, 0.053) |
| | (0.333, 0.667, 0.149) | (0.667, 0.333, 0.149) |
| | (0.667, 0.333, 0.246) | (0.333, 0.667, 0.246) |
| | (0.000, 0.000, 0.350) | (0.333, 0.667, 0.350) |
| | (0.000, 0.000, 0.454) | (0.333, 0.667, 0.454) |
| | (0.667, 0.333, 0.551) | (0.000, 0.000, 0.550) |
| | (0.333, 0.667, 0.647) | (0.667, 0.333, 0.647) |
| | (0.333, 0.667, 0.753) | (0.667, 0.333, 0.753) |
| | (0.667, 0.333, 0.850) | (0.000, 0.000, 0.850) |
| | (0.000, 0.000, 0.947) | (0.333, 0.667, 0.947) |
| T4 | | |
| | (0.667, 0.333, 0.050) | (0.000, 0.000, 0.050) |
| | (0.333, 0.667, 0.147) | (0.667, 0.333, 0.147) |
| | (0.333, 0.667, 0.250) | (0.667, 0.333, 0.250) |
| | (0.333, 0.667, 0.353) | (0.667, 0.333, 0.353) |
| | (0.667, 0.333, 0.451) | (0.333, 0.667, 0.451) |
| | (0.333, 0.667, 0.549) | (0.667, 0.333, 0.549) |
| | (0.667, 0.333, 0.647) | (0.333, 0.667, 0.647) |
| | (0.000, 0.000, 0.749) | (0.333, 0.667, 0.749) |
| | (0.667, 0.333, 0.850) | (0.333, 0.667, 0.850) |
| | (0.667, 0.333, 0.953) | (0.333, 0.667, 0.953) |
| T5 | | |
| | (0.667, 0.333, 0.048) | (0.333, 0.667, 0.048) |
| | (0.000, 0.000, 0.153) | (0.333, 0.667, 0.153) |
| | (0.333, 0.667, 0.251) | (0.667, 0.333, 0.251) |
| | (0.667, 0.333, 0.349) | (0.000, 0.000, 0.349) |
| | (0.667, 0.333, 0.448) | (0.333, 0.667, 0.448) |
| | (0.000, 0.000, 0.552) | (0.333, 0.667, 0.552) |
| | (0.333, 0.667, 0.650) | (0.667, 0.333, 0.650) |
| | (0.000, 0.000, 0.747) | (0.333, 0.667, 0.747) |
| | (0.000, 0.000, 0.852) | (0.333, 0.667, 0.852) |
| | (0.667, 0.333, 0.950) | (0.000, 0.000, 0.950) |

Table 4.4: Relaxed atomic crystal coordinates for the five randomly stacked BN (t-BN) structures.

## 4.4  CONCLUSIONS

In summary, we investigated the impacts of stacking type and number of layers on the electronic and optical properties of bulk, bilayer, and monolayer h-BN polytypes with first-principles calculations. Most of the bulk band gaps are indirect with values ranging from 5.33-6.23 eV. The gaps of the bilayers are wider due to quantum confinement and cover the range from 6.75-7.10 eV. For both bulk and bilayer, there is a strong correlation between structural stability and the value of the band gap. For the h-BN monolayer the DFT gap is direct, but it becomes indirect after quasiparticle corrections. Most polytypes have significantly stronger phonon-assisted optical MEs than bulk Si, thus phonon-assisted optical transitions are important for luminescence in ordered h-BN structures. The emitted photons are primarily TE polarized, which facilitates light extraction in LEDs. The symmetry breaking by random stacking in t-BN results in a quasi-direct band gap that only weakly allows direct optical transitions. Our results show that the electronic and optical properties of h-BN materials can controlled by the stacking sequence and number of BN layers to engineer light-emitting devices in the deep-UV part of the spectrum.

# CHAPTER V

# Quasiparticle Band Structure and Optical Properties of Rutile GeO$_2$, an Ultrawide-Band-Gap Semiconductor

Rutile GeO$_2$ is a visible and near-ultraviolet-transparent oxide that has not been explored for semiconducting applications in electronic and optoelectronic devices. We investigate the electronic and optical properties of rutile GeO$_2$ with first-principles calculations based on density functional theory and many-body perturbation theory. Our band-structure calculations indicate a dipole-forbidden direct band gap at $\Gamma$ with an energy of 4.44 eV and effective masses equal to $m_{e\perp}{}^* = 0.43\ m_0$, $m_{e\parallel}{}^* = 0.23\ m_0$, $m_{h\perp}{}^* = 1.28\ m_0$, and $m_{h\parallel}{}^* = 1.74\ m_0$. In contrast to the self-trapped hole polarons by lattice distortions in other wide-band-gap oxides that reduce the hole mobility, holes in rutile GeO$_2$ are delocalized due to their small effective mass. The first allowed optical transitions at $\Gamma$ occur at 5.04 eV ($\overrightarrow{E} \perp \overrightarrow{c}$) and 6.65 eV ($\overrightarrow{E} \parallel \overrightarrow{c}$). We also evaluate the optical absorption coefficient and refractive index along both crystallographic directions. Our estimates for the exciton binding energies using the Bohr model are close to the reported experimental value. The ultrawide-band-gap and light carrier effective masses of rutile GeO$_2$, coupled with its optical transparency in the visible and near UV are promising for applications in UV-transparent conductors and solar-blind photodetectors.

## 5.1  INTRODUCTION

Germanium dioxide exists in multiple polytypes, such as the low-density $\alpha$-quartz (trigonal) phase with tetrahedrally coordinated Ge atoms and the octahedrally co-ordinated rutile (tetragonal) structure.[6,147,148] Rutile GeO$_2$, in particular, is chemically and structurally similar to other oxide materials such as SnO$_2$ and TiO$_2$, two

common materials in the transparent conducing oxide (TCO) and semiconductor industries which also crystallize in the rutile phase, among multiple polytypes.[149–151] Rutile belongs to the tetragonal Bravais lattice group with lattice parameters $a = b \neq c$ and $\alpha = \beta = \gamma = 90°$. The experimental lattice parameters of rutile $GeO_2$ are $a = 4.4066$ Å and $c = 2.8619$ Å.[6] The crystal structure is shown in Figure 5.1. Considering the anisotropy of the crystal structure, measurements are often performed along two axes, $\perp \vec{c}$ (*i.e.* along $\vec{a}$) and $\| \vec{c}$. One main issue that rutile $GeO_2$ could overcome is the dearth of *p*-type TCO materials, as many oxides exhibit flat valence bands that give rise to trapped hole polarons.[85,152] While $TiO_2$ and $SnO_2$ are difficult to *p*-type dope, rutile $GeO_2$ has recently been theoretically predicted to be ambipolarly dopable. Chae *et al.* showed through first-principles defect calculations that group-III metals such as Al on the Ge site are possible acceptors with rather large ionization energies of 0.45-0.54 eV, yet the codoping of group-III dopants with H and subsequent annealing allows the incorporation of high acceptor concentrations that enable *p*-type conduction through the impurity band.[153] The largest experimental band gap of rutile $GeO_2$ (4.68 eV)[7] is also wider than that of $TiO_2$ and $SnO_2$ (3.03 eV and 3.6 eV, respectively),[85,154–158] and falls in the UVC region of the electromagnetic spectrum (4.28-6.20 eV; 200-290 nm). This gap value is desirable for solar-blind photodetectors, which require materials that absorb wavelengths shorter than 290 nm while maintaining transparency at lower photon energies. Additionally, the UVC region is the most effective for germicidal applications, *e.g.* water purification and food sterilization.[27] The two properties of an ultra-wide-band gap in the UVC and the possibility of ambipolar doping motivate the study of rutile $GeO_2$ for optoelectronic applications.

The majority of previous work on $GeO_2$ focuses on the $\alpha$ (quartz) polytype. Also, most theoretical work on rutile $GeO_2$ does not go beyond density functional theory (DFT)[147,159–161] and suffers from the band-gap underestimation problem. Recently, Chae *et al.* and Samanta *et al.* reported band structures calculated with hybrid functionals and many-body perturbation theory (GW method), respectively.[13,153] Samanta *et al.* showed that varying the lattice parameters of r-$GeO_2$ significantly impacts the calculated value of the band gap, even more so than the type of functional used on the DFT level.[13] Even on the $G_0W_0$ level, the band gap can range from 4.05 eV to 5.78 eV by decreasing the volume from 55.91 Å$^3$ to 51.03 Å$^3$, all of which maintain a dynamically stable structure. Aside from the crystal and electronic structures, several studies have measured[7,148] or calculated[159,162] the complex dielectric function, refractive index, absorption coefficients, and other related properties. The theoreti-
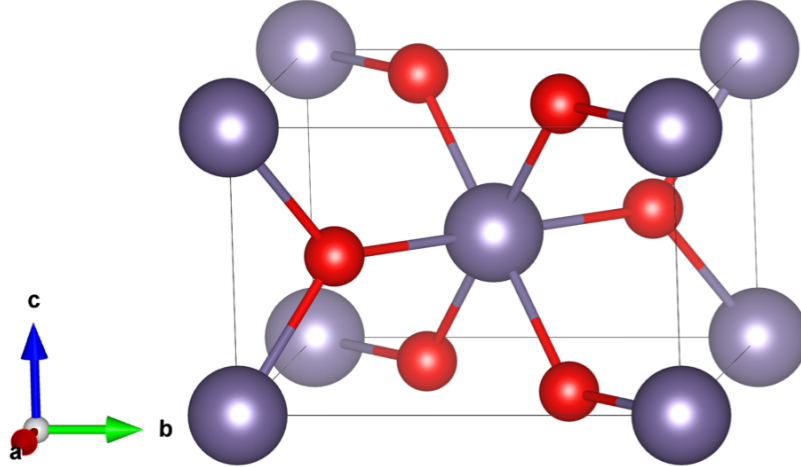
Figure 5.1: Crystal structure of r-GeO$_2$ (large grey atoms are Ge and small red atoms are O). Our calculations employed experimental lattice parameters and atomic positions from Ref. 6.

cal reports in the literature remain on the DFT level, which are affected by the gap underestimation and are not accurate for comparison to experiment.

In this work, we apply electronic-structure calculations based on many-body perturbation theory to characterize the electronic and optical properties of rutile GeO$_2$ (r-GeO$_2$) and enable accurate comparisons with experiment. We determine the band structure, band gap, and carrier effective masses. We explore the formation of self-trapped hole polarons to determine their possible impact on hole transport. We also calculate the interband optical matrix elements along both crystallographic directions and analyze the imaginary part of the dielectric function. We also obtain the real part of the dielectric function, refractive index, and absorption coefficient along both crystallographic directions. Our work provides atomistic insights on experimental measurements and can guide future studies on deep-UV optoelectronic and solar-blind photodetection applications.

## 5.2   COMPUTATIONAL METHODS

Our first-principles calculations are based on density functional and many-body perturbation theories. The experimental lattice parameters of r-GeO$_2$ ($a = 4.4066$ Å and $c = 2.8619$ Å)[6] were used for the electronic and optical properties calculations without structural relaxation to allow a direct comparison to experiment. First, the mean-field charge density, wave functions, and band eigenvalues were calculated within the local-density approximation (LDA)[163,164] with the Quantum ESPRESSO

code[62] before applying the $G_0W_0$ method with the BerkeleyGW software[63] to include electron self-energy effects on the band structure. Norm-conserving pseudopotentials[68] were used to describe the interactions of the valence electrons of the Ge ($4s$ and $4p$) and O ($2s$ and $2p$) atoms with the ionic cores. We employed a plane-wave basis set with a 90 Ry cutoff energy for the DFT wave-function calculations and sampled the Brillouin zone (BZ) with an $8\times8\times12$ grid, which converge the total energy of the system to within 1 mRy/atom. For the $G_0W_0$ calculations we used a plane-wave basis for the dielectric matrix up to a 35 Ry cutoff energy and sampled the BZ with a $4\times4\times6$ grid. We summed over 2,000 and 2,504 total bands for the dielectric-matrix and the self-energy calculations, respectively. The generalized plasmon-pole model[64] and the static-remainder approach[70] were incorporated to extrapolate the dielectric function to finite frequency and more rapidly converge the Coulomb-hole summation over unoccupied states, respectively. The convergence errors stemming from our choice of $G_0W_0$ calculation parameters are $\sim$5 meV from the total bands of the dielectric-matrix calculation, $\sim$10 meV from the total bands of the self-energy calculation, $\sim$50 meV from the screened Coulomb cutoff of 35 Ry, and $\sim$10 meV from the BZ sampling grid of $4\times4\times6$, resulting in a total estimated convergence error for our $G_0W_0$ calculations of $\sim$75 meV. The DFT and $G_0W_0$ band structures, as well as the velocity-operator matrix elements (VMEs) that describe band-to-band optical transitions,[135] were interpolated to fine BZ sampling grids (up to $160\times160\times240$) with the maximally localized Wannier function (MLWF) method[65] and the wannier90 code[66] to determine the imaginary part of the dielectric function, $\epsilon_2$.[67] The Bethe-Salpeter-equation (BSE) method as implemented in BerkeleyGW was also used to calculate $\epsilon_2$ on a $16\times16\times24$ BZ sampling grid, including twelve valence and two conduction bands, and using 0.2 eV Gaussian broadening to evaluate excitonic effects on the dielectric function. Self-trapped hole polarons are investigated using the Heyd-Scuseria-Ernzerhof (HSE06) functional, with the Hartree-Fock mixing parameter, BZ sampling, and the supercells described in Ref. 153. For the polaron calculations only we relaxed the crystal structure. Our relaxed lattice parameters ($a$ = 4.394 Å and $c$ = 2.866 Å) agree with experiment[6] within <0.3%. We evaluate the stability of self-trapped holes by evaluating the self-trapping energy (EST) as defined in Ref. 85.

## 5.3 ELECTRONIC PROPERTIES

### 5.3.1 Band Structure and Band Gap

The DFT-LDA and $G_0W_0$ band structures of r-GeO$_2$ (Figure 5.2) provide information about its fundamental electronic and optical properties. Both the DFT-LDA and $G_0W_0$ band structures exhibit direct fundamental band gaps at $\Gamma$. However, as shown in Table 5.1, the DFT band gap is only 1.96 eV, which is 56% smaller than the $G_0W_0$ band gap of 4.44 eV and 58% smaller than the experimental value of 4.68 eV.[7] Such a large difference is expected from the DFT calculation and exemplifies the need to include many-body effects; the $G_0W_0$ band gap differs by only 5% from experiment. Previous calculations by Chae *et al.* using HSE06 with 35% Hartree-Fock exchange found a band gap of 4.64 eV after relaxing the structure and obtaining lattice parameters $a = 4.394$ Å and $c = 2.866$ Å.[153] Samanta *et al.* investigated the pressure dependence of the band gap of r-GeO$_2$ and found that the structure is dynamically stable over a wide range of lattice volumes from -14% to +3% strain, referenced to the experimental volume of 55.57 Å$^3$.[6,13] They calculate and report several $G_0W_0$ band gaps from 4.05 eV to 5.78 eV using different unit-cell volumes reported in the literature, ranging from 51.03 Å$^3$ to 55.91 Å$^3$.[6,13,147] For this reason we performed our calculations using the experimental lattice parameters to avoid artifacts from the underestimation of the lattice constants by DFT-LDA.

### 5.3.2 Effective Masses and Polaron Properties

We also obtain the hole and electron effective masses by fitting the hyperbolic equation[165]:

$$E(k) = \frac{\mp 1 \pm \sqrt{1 + 4\alpha\hbar^2 k^2/(2m^*)}}{2\alpha + E_0}, \tag{5.1}$$

to the Wannier-interpolated $G_0W_0$ band structure along the $\Gamma\rightarrow$X and $\Gamma\rightarrow$Z directions for the top valence band (VB) and bottom conduction band (CB). The energy ranges from the corresponding band extrema used to perform the effective-mass fits and the associated wave-vector ranges are 0.5 eV for $m_{e\perp}{}^*$ (17.5% of the $\Gamma\rightarrow$X BZ segment), 0.8 eV for $m_{e\parallel}{}^*$ (11.4% of $\Gamma\rightarrow$Z), 0.4 eV for $m_{h\perp}{}^*$ (28.1% of $\Gamma\rightarrow$X BZ), and 0.3 eV for $m_{h\parallel}{}^*$ (18.2% of $\Gamma\rightarrow$Z BZ). In Equation 5.1, $E(k)$ is band energy as a function of crystal momentum $k$, $\alpha$ is the non-parabolicity fitting parameter, $\hbar$ is the reduced Planck constant, $m^*$ is the electron (-/+) or hole (+/-) effective mass, and $E_0$ is the energy of the VBM (-/+) or CBM (+/-). While the band gap changes signif-

icantly between DFT and $G_0W_0$, the curvatures of the bands remain approximately the same between the two levels of theory, especially at $\Gamma$. As such, the hole and electron effective masses calculated from both methods agree well, so we only report the $G_0W_0$ effective masses in Table 5.2. The electron effective mass along $\Gamma{\rightarrow}X$ ($m_{e\perp}{}^* = 0.43\ m_0$) is about a factor of 2 larger than along $\Gamma{\rightarrow}Z$ ($m_{e\parallel}{}^* = 0.23\ m_0$), but both are comparable to those of other wide-band-gap materials; rutile $SnO_2$ (r-$SnO_2$), a chemical and structural analogue to r-$GeO_2$, has essentially the same $m_{e\parallel}{}^*$ ($0.234\ m_0$) and slightly lighter $m_{e\perp}{}^*$ ($0.299\ m_0$).[166] Yan $et\ al.$ reported GaN electron effective masses of $m_{e\parallel}{}^* = 0.19\ m_0$ and $m_{e\perp}{}^* = 0.21\ m_0$.[112] The electron effective mass of $\beta$-$Ga_2O_3$ ranges from $\sim$0.23 $m_0$ to 0.34 $m_0$ depending on the crystallographic direction.[91,167] On the other hand, the hole effective mass of r-$GeO_2$ is notably small for such an ultra-wide-gap material. Our calculations show values of $m_{h\perp}{}^* = 1.28\ m_0$ and $m_{h\parallel}{}^* = 1.74\ m_0$. For comparison, for r-$SnO_2$ Schleife $et\ al.$ report $m_{h\perp}{}^* = 1.21\ m_0$ and $m_{h\parallel}{}^* = 1.47\ m_0$,[152] while Varley $et\ al.$ report $m_{h\perp}{}^* = 1.37\ m_0$ and $m_{h\parallel}{}^* = 1.61\ m_0$.[168] Other common ultra-wide-gap materials like AlN and $\beta$-$Ga_2O_3$ have significantly larger hole effective masses. For AlN, the heavy hole effective masses are $m_{hh\perp}{}^* = 10.42\ m_0$ and $m_{hh\parallel}{}^* = 3.53\ m_0$.[169] The valence bands of $\beta$-$Ga_2O_3$ are notoriously flat[78], resulting in a large hole effective mass of $\sim$40 $m_0$[88,170,171] that yields self-trapped hole polarons[85]. However, for r-$GeO_2$, we calculate the hole self-trapping energy (EST) to be 0.0094 eV, indicating that in the absence of impurities self-trapped hole polarons are only weakly bound and thermally dissociate to delocalized holes at room temperature (hole polarons in r-$GeO_2$ are more strongly bound to negatively-charged acceptors such as Al, however[153]). The delocalized nature of holes stems from their light effective mass and separates r-$GeO_2$ from other wide-gap oxides and is one reason why this material can also be $p$-type doped. Overall, the band structure provides the fundamental information about the electronic properties of this material such as its direct band gap of 4.44 eV and the small, anisotropic electron and hole effective masses, while it also serves as the starting point for investigating optical properties.

## 5.4 OPTICAL PROPERTIES

### 5.4.1 Absorption Onsets

We determined the character (allowed or forbidden) of optical transitions across the band gap of r-$GeO_2$, that ultimately control its optical spectra, by analyzing the band energies and interband VMEs. We examine the VMEs for transitions from the top six valence bands to the bottom conduction band at $\Gamma$ (Table 5.3), as these are the
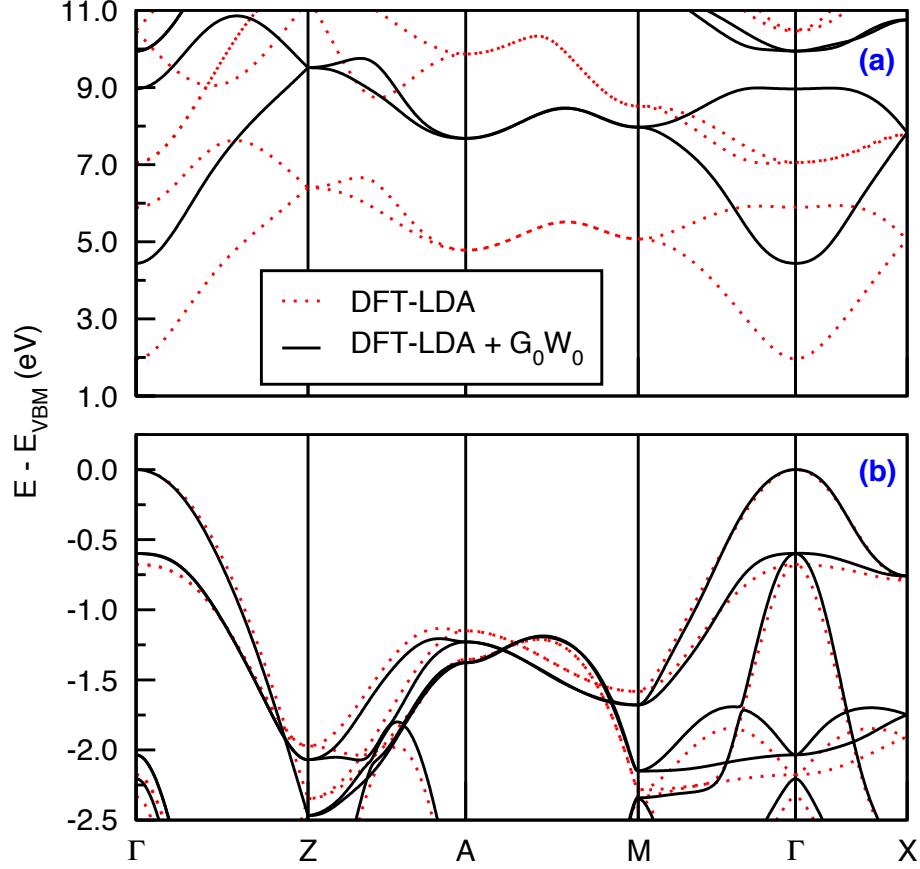
Figure 5.2: (a) Bottom conduction and (b) and top valence bands of r-GeO$_2$ within DFT-LDA (red dotted) and DFT-LDA + G$_0$W$_0$ (black solid). The band gap is direct at $\Gamma$ with a magnitude of 1.96 eV (LDA) and 4.44 eV (G$_0$W$_0$).

| Method | Band gap (eV) |
|---|---|
| DFT-PBE[13] | 1.80 |
| DFT-LDA (present work) | 1.96 |
| DFT-PBE + G$_0$W$_0$[13] | 4.20 |
| DFT-LDA + G$_0$W$_0$ (present work) | 4.44 |
| Experiment (UV-absorption)[7] | 4.68 |

Table 5.1: Magnitude of the direct band gap of r-GeO$_2$ at $\Gamma$ calculated with different methods and compared to experimental optical measurements. The four calculations shown used the same set of experimental lattice parameters: $a = 4.4066$ Å and $c = 2.8619$ Å.[6]

| Direction | $m_e^*$ ($m_0$) | $m_h^*$ ($m_0$) |
|---|---|---|
| $\Gamma \rightarrow$X | 0.43 | 1.28[a] |
| $\Gamma \rightarrow$Z | 0.23 | 1.74[a] |

[a]Values previously reported in Ref. 153.

Table 5.2: Effective masses of electrons and holes of r-GeO$_2$ along the $\Gamma \rightarrow$X and $\Gamma \rightarrow$Z directions calculated by a hyperbolic fit to the G$_0$W$_0$ band structure.

only bands that contribute to optical absorption for photon energies up to 10 eV, and find several noteworthy features. First, the VME is zero along both the $\perp \overrightarrow{c}$ and $\| \overrightarrow{c}$ directions for transitions from the top valence band to the bottom conduction band. This coincides with the small value for the imaginary part of the dielectric function $\epsilon_2$ (plotted in logarithmic scale in Figure 5.3) at photon energies near the band gap energy. We also show the VMEs for the top valence band to bottom conduction band transition for electron wave vectors along the $\Gamma \rightarrow$X and $\Gamma \rightarrow$Z BZ directions in Figure 5.4. While the $\overrightarrow{x}$ Cartesian component ($\perp \overrightarrow{c}$) of the VMEs near $\Gamma$ is zero along $\Gamma \rightarrow$Z and increases rapidly along $\Gamma \rightarrow$X , the $\overrightarrow{z}$ component ($\| \overrightarrow{c}$) VME remains negligible along both directions. This explains the stronger absorption onset for light polarized along the $\perp \overrightarrow{c}$ direction (Figure 5.3), which is determined by the interband VMEs in the vicinity of $\Gamma$. Ultraviolet absorption measurements performed by Stapelbroek *et al.* also pointed to a forbidden transition for the fundamental band gap of r-GeO$_2$,[7] and our calculations are in agreement with this previous analysis. For the second and third valence bands, which are degenerate at $\Gamma$, the VME is strong $\perp \overrightarrow{c}$ but not $\| \overrightarrow{c}$ (Table 5.3). Therefore, our calculations reveal that r-GeO$_2$ only absorbs weakly for photon energies between the band gap (4.44 eV) and the energy difference between the second valence band and the CBM (5.04 eV) due to the fundamental interband transition being dipole forbidden. The value for $\epsilon_2$ plateaus with increasing photon energy above 5.04 eV (Figure 5.3). Transitions for light polarized along $\overrightarrow{c}$ from the top five valence bands to the CBM are weak, with $\epsilon_2$ increasing slowly until the sixth valence band to CBM transition energy is reached at 6.65 eV, above which r-GeO$_2$ absorbs strongly also along $\overrightarrow{c}$.

### 5.4.2 Excitonic Effects

We also calculated excitonic effects on the imaginary part of the dielectric function using the BSE method, and the results are shown in Figure 5.5. Due to the computational cost of the BSE calculations, we used a coarser 16×16×24 BZ sampling grid to show the overall difference of the $\epsilon_2$ spectra both with and without excitonic effects

| Valence band index | $E_{CB} - E_{VB,i}$ (eV) | VME ($\perp \vec{c}$) | VME ($\parallel \vec{c}$) |
|---|---|---|---|
| 1 | 4.44 | 0.00 | 0.00 |
| 2 | 5.04 | 0.53 | 0.00 |
| 3 | 5.04 | 0.53 | 0.00 |
| 4 | 6.47 | 0.00 | 0.00 |
| 5 | 6.47 | 0.00 | 0.00 |
| 6 | 6.65 | 0.00 | 0.96 |

Table 5.3: Energies and matrix elements of optical transitions from the top six valence bands to the bottom conduction band of r-GeO$_2$ at $\Gamma$, calculated from the G$_0$W$_0$ band structure. The magnitudes of the velocity-operator matrix elements (in Hartree atomic units) for each band-to-band transition are shown for both the $\perp \vec{c}$ and $\parallel \vec{c}$ directions.
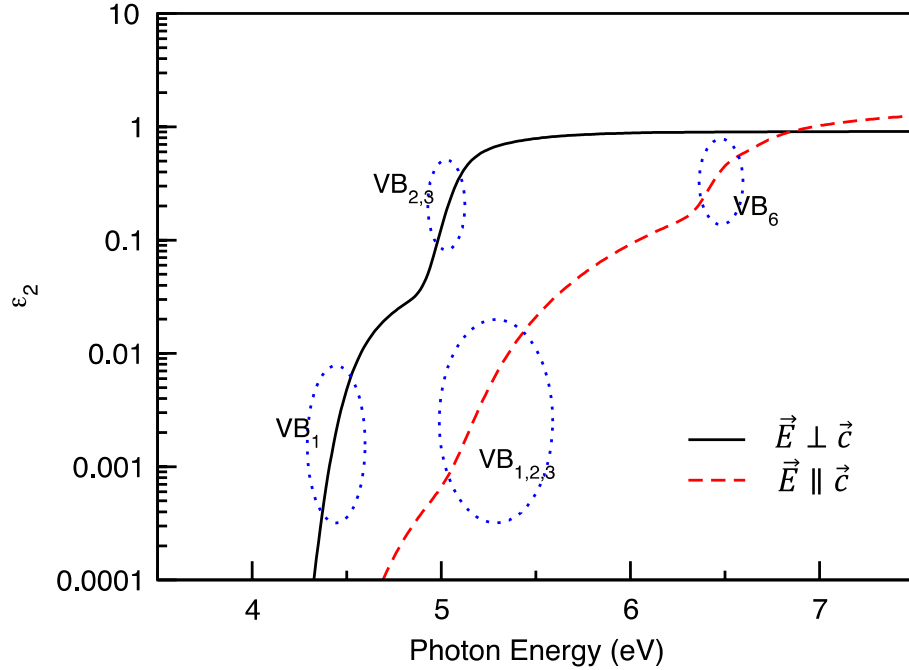


Figure 5.3: Imaginary part of the dielectric function of r-GeO$_2$ in logarithmic scale calculated using the maximally localized Wannier function method on a fine 160×160×240 BZ sampling grid. The spectra show multiple electronic transition onsets with increasing photon energy. The approximate onsets of specific valence-to-conduction band transitions are highlighted. While the fundamental band gap occurs at 4.44 eV, the corresponding optical transition is dipole-forbidden, resulting in a small value for $\epsilon_2$ at that photon energy.
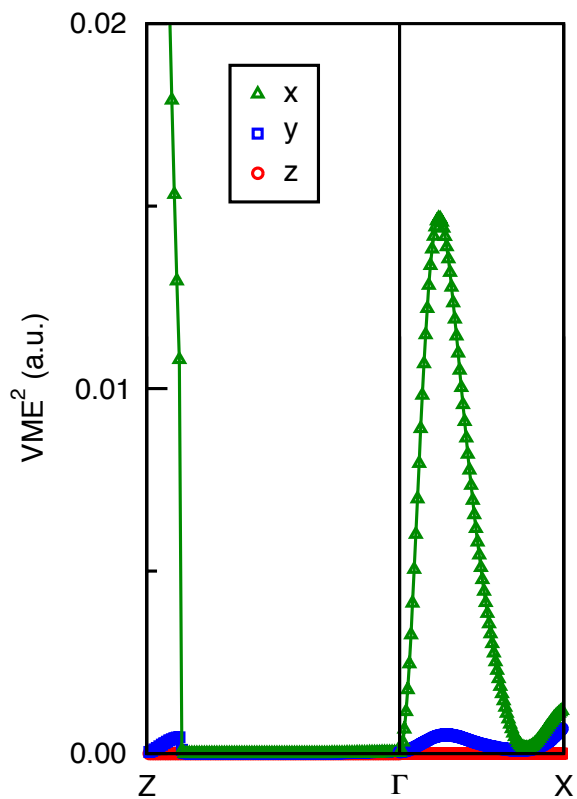
Figure 5.4: Velocity matrix elements squared (in Hartree atomic units) for electron wave vectors along the $\perp \vec{c}$ ($\Gamma \rightarrow$X) and $\| \vec{c}$ ($\Gamma \rightarrow$Z) directions of the BZ. Only the $\Gamma \rightarrow$X direction shows strong VMEs for light polarized $\perp \vec{c}$ near $\Gamma$, which explains the stronger absorption onset for the $\perp \vec{c}$ polarization in Figure 5.3.
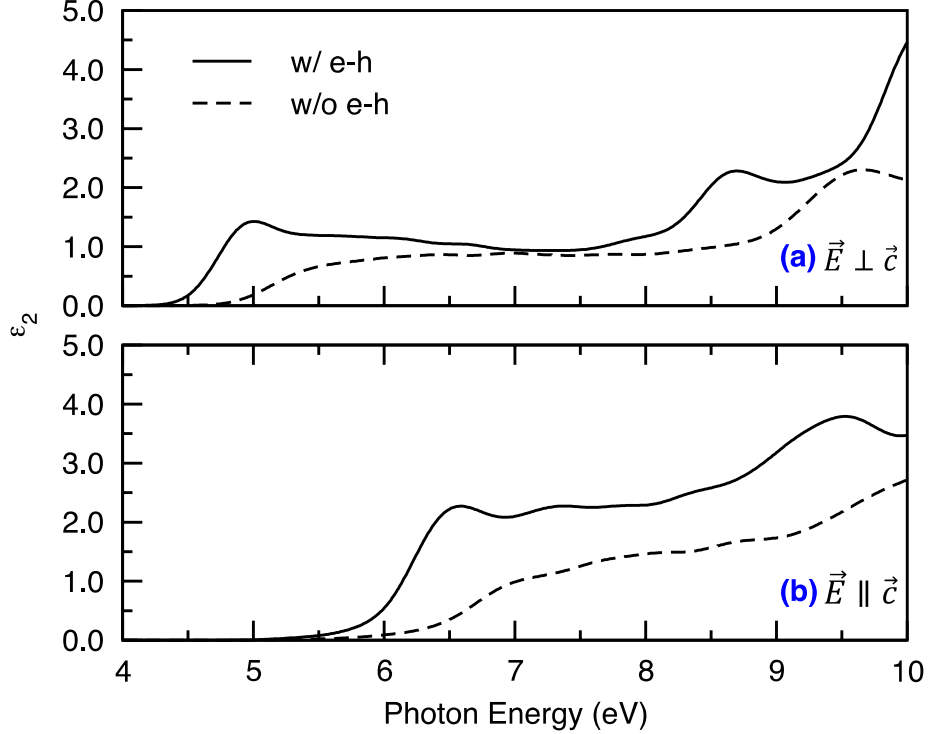
Figure 5.5: Imaginary part of the dielectric function of r-GeO$_2$ as calculated with the BSE on a 16×16×24 BZ sampling grid without (dashed) and with (solid) exitonic effects included. Panel (a) shows the results for light polarized perpendicular to $\vec{c}$ and (b) parallel to $\vec{c}$.

included (in comparison, the spectra calculated without excitonic effects in Figure 5.3 were obtained for a finer BZ sampling grid and exhibit sharper spectral features). The $\epsilon_2$ spectra are converged for this BZ sampling grid. The general shape and onsets of the $\epsilon_2$ spectra calculated both with and without excitonic effects are similar. As with the r-SnO$_2$ $\epsilon_2$ results,[152] we find that r-GeO$_2$ has anisotropic optical properties for light polarized along different crystallographic orientations, with the onset of absorption for $\vec{E}\perp\vec{c}$ at lower energies than $\vec{E}\|\vec{c}$ as discussed previously. Excitonic effects introduce an overall spectral-weight shift to lower energies. The $\epsilon_2$ curves including excitonic effects rise much quicker than those without excitonic effects. These excitonic corrections to the optical spectra do not originate from a shifting of the peak positions by the exciton binding energy (which is only of the order of 39 meV as we discuss below), but rather from the modification of the optical matrix elements due to the coherent coupling of excited states induced by electron-hole interactions.[172]

We also investigate the exciton binding energies for the lowest exciton states. Convergence for the fine $k$-point sampling grid within BSE are shown in Table 5.4 and Figure 5.6. Our calculations using a 16×16×24 BZ sampling grid result in an exciton

| Fine grid | Exciton binding energy (eV) |
| --- | --- |
| 8×8×12 | 0.280 |
| 12×12×18 | 0.210 |
| 16×16×24 | 0.184 |
| $\infty$ (extrapolated) | 0.152 |

Table 5.4: Lowest exciton binding energy along $\vec{E}\perp\vec{c}$ for different fine grids used in the Bethe-Salpeter-equation calculations to show its convergence with respect to $k$-point sampling.

binding energy of 184 meV for $\vec{E}\perp\vec{c}$ and 169 meV for $\vec{E}\|\vec{c}$, which significantly overestimate the experimental value for $\vec{E}\perp\vec{c}$ (39 meV).[7] We extrapolate a value of 152 meV for $\vec{E}\perp\vec{c}$ and an infinite BZ sampling grid (Figure 5.7). A similar result and discussion were presented by Schleife *et al.* for r-SnO$_2$, where they discuss the importance of ionic screening that is typically omitted in GW and BSE first-principles calculations.[152] Schleife *et al.* report exciton binding energies for r-SnO$_2$ of 222 meV for $\vec{E}\perp\vec{c}$ and 191 meV for $\vec{E}\|\vec{c}$, closely matching the values we calculate for r-GeO$_2$. While GW and BSE methods use the high-frequency dielectric constant $\epsilon_\infty$ which does not include ionic screening effects, the static dielectric constant does include ionic screening. By using the average static dielectric constants in the formula for the Wannier-Mott exciton, they estimate exciton binding energies equal to 19 meV ($\vec{E}\perp\vec{c}$) and 16 meV ($\vec{E}\|\vec{c}$), which are in much better agreement with the experimental value for SnO$_2$ of $\sim$30 meV.[173,174] Using the same Bohr model where $E_b = \frac{13.6eV \times \mu^*}{\epsilon_0^2}$ (where $\mu^*$ is the reduced effective mass, and $\epsilon_0$ is the static dielectric constant) and our previously calculated static dielectric constants $\epsilon_{0,\perp\vec{c}} = 16.02$ and $\epsilon_{0,\|\vec{c}} = 7.78$,[153] we estimate exciton binding energies of 17 meV ($\vec{E}\perp\vec{c}$) and 46 meV ($\vec{E}\|\vec{c}$). The reduced effective masses were calculated in both directions using the values from Table 5.2, where $\mu^*_{\perp\vec{c}} = 0.32$ and $\mu^*_{\|\vec{c}} = 0.20$. If we instead use the directionally averaged static dielectric constant 13.27 rather than the direction-dependent values, we obtain $E_b = 25$ meV ($\vec{c}\perp\vec{c}$) and 16 meV ($\vec{E}\|\vec{c}$). Therefore, the inclusion of ionic screening brings our calculated values in better agreement with experiment (39 meV).[7]

### 5.4.3 Optical Constants

We further utilized the Kramers-Kronig relation to obtain the real part of the dielectric function ($\epsilon_1$) of r-GeO$_2$ from the imaginary part ($\epsilon_2$) and hence determine the refractive index ($n$), extinction coefficient ($\kappa$), and absorption coefficient ($\alpha$) over
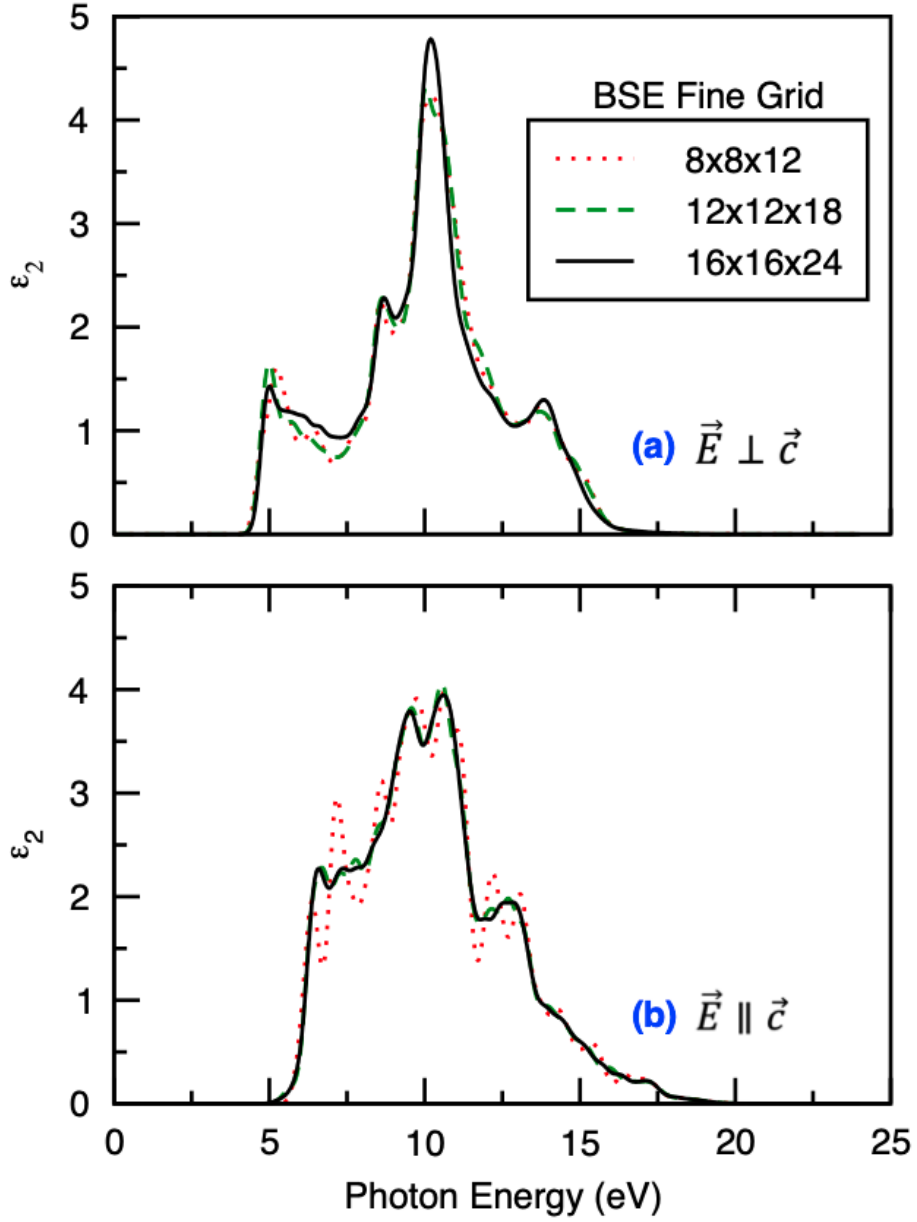
Figure 5.6: Imaginary part of the dielectric function of r-GeO$_2$ as calculated with the Bethe Salpeter Equation on various fine grids along (a) $\vec{E}\perp\vec{c}$ and (b) $\vec{E}\,\|\,\vec{c}$ to show convergence of the spectra with respect to $k$-point sampling.
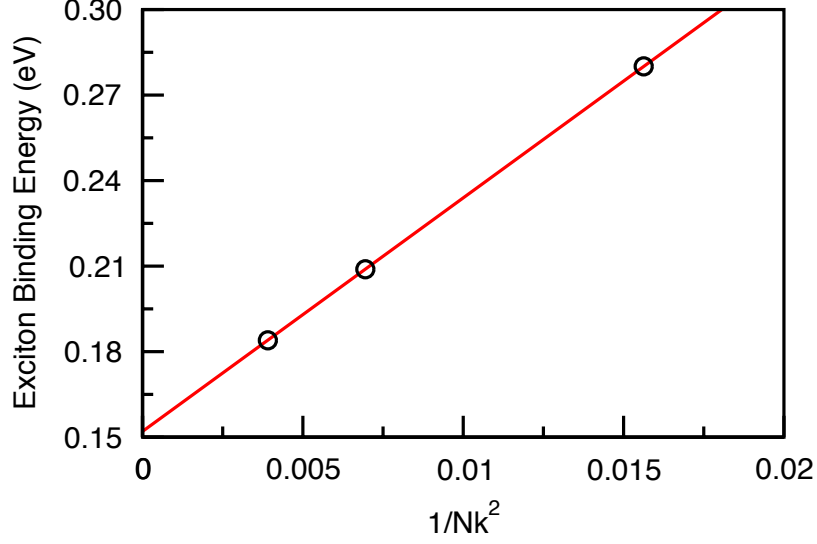
Figure 5.7: Extrapolation of the smallest direct exciton binding energy along $\overrightarrow{E} \perp \overrightarrow{c}$ as the number of $k$-points $(N_k)$ approaches infinity. The extrapolated value for an infinitely fine sampling mesh is 152 meV.

the 0-10 eV photon-energy range. (See also Ref. 175.) To ensure convergence of the real part in this energy range, the imaginary part was calculated and the Kramers-Kronig relation integrated for energies up to 45 eV. For this calculation, we used the $\epsilon_2$ without excitonic effects calculated from maximally localized Wannier functions on a 160×160×240 BZ sampling grid. While we did explore excitonic corrections to the imaginary dielectric function for photon energies up to 10 eV, the Kramers-Kronig transformation requires a much wider energy range to yield accurate values for the real part of the dielectric function (and, subsequently, the refractive index and the absorption coefficient), which is computational demanding. Figure 5.8 shows both components of the dielectric function from 0 eV to 10 eV. The refractive index $n$ and extinction coefficient $\kappa$ are determined according to:

$$n = \sqrt{\frac{\sqrt{\epsilon_1^2 + \epsilon_2^2} + \epsilon_1}{2}} \qquad (5.2)$$

and:

$$\kappa = \frac{\sqrt{\epsilon_1^2 + \epsilon_2^2} - \epsilon_1}{2}. \qquad (5.3)$$

The calculated refractive index is quite large, ranging from ∼1.9 to ∼2.5 between 0 eV to 10 eV. Our results agree well with those calculated using ultrasoft pseudopotentials within the generalized gradient approximation on the DFT level by Liu *et*

*al..*[159] The refractive indices of other well-known visible transparent semiconductors are 1.46-1.51 from 2.3 eV to 5.2 eV ($SiO_2$ glass)[156] and 2.36-2.78 from 1.2 eV to 3.4 eV (*w*-GaN)[176], for example. Between 1.77-3.10 eV (700 nm to 400 nm), the refractive index of r-$GeO_2$ changes by only 0.03 for both crystallographic directions. Such a small change in $n$ over the entire visible range is one sign that r-$GeO_2$ is a promising candidate for applications requiring low chromatic dispersion. For a direct comparison to experiment, we determined the absorption coefficient $\alpha$ via:

$$\alpha(E) = \frac{4\pi\kappa E}{hc}, \tag{5.4}$$

where $E$ is the photon energy, $h$ is the Planck constant, and $c$ is the speed of light. Figure 5.9 shows the calculated refractive index and absorption coefficient as a function of energy. Our calculations confirm the previous experimental finding by Stapelbroek *et al.* that the first band-to-band transition is dipole-forbidden and agree with the dichroism measured in the polarized edge absorption experiment.[7] This anisotropy is apparent in the absorption coefficient shown in Figure 5.9(b); $\alpha$ becomes sizable only above ~5 eV, the energy of the second VB to CBM transition. Although our calculated $G_0W_0$ band gap is 0.24 eV smaller than that reported experimentally, when we rigidly shift our absorption coefficient curves by this amount to align the band gaps, the calculated results closely match the 77 K experimental data, as shown in Figure 5.10.[7] We find that, just like the experiment, $\alpha$ for $\vec{E} \perp \vec{c}$ has a much steeper slope than for $\vec{E} \parallel \vec{c}$ at energies near the band gap. From the lack of strong VMEs of electronic transitions within 2 eV of the band gap along $\vec{c}$, this behavior is expected. Overall, the electronic and optical properties derived from the $G_0W_0$ band structure agree well with experimental results.

### 5.4.4  Applications in Solar-Blind Photodetection

The optical absorption of r-$GeO_2$ is important to consider for applications in solar-blind photodetection. An ideal solar-blind photodetector absorbs wavelengths shorter than 290 nm (4.28 eV) but is entirely transparent in the visible and near-UV ranges.[177] One promising solar-blind material is $\beta$-$Ga_2O_3$, which has a wide band gap (~4.5 eV) close to that of r-$GeO_2$.[56,57,60,78] $\beta$-$Ga_2O_3$ nanodevices have been shown to selectively absorb light in the desired solar-blind range. An advantage of nanoscale devices is the potential miniaturization of photodetectors, which opens future work for r-GeO2 devices. L. Li *et al.* fabricated bridged $\beta$-$Ga_2O_3$ nanobelts that have a high response at 250 nm that is ~$10^6$ higher than in the visible,[57] indicating an ex-
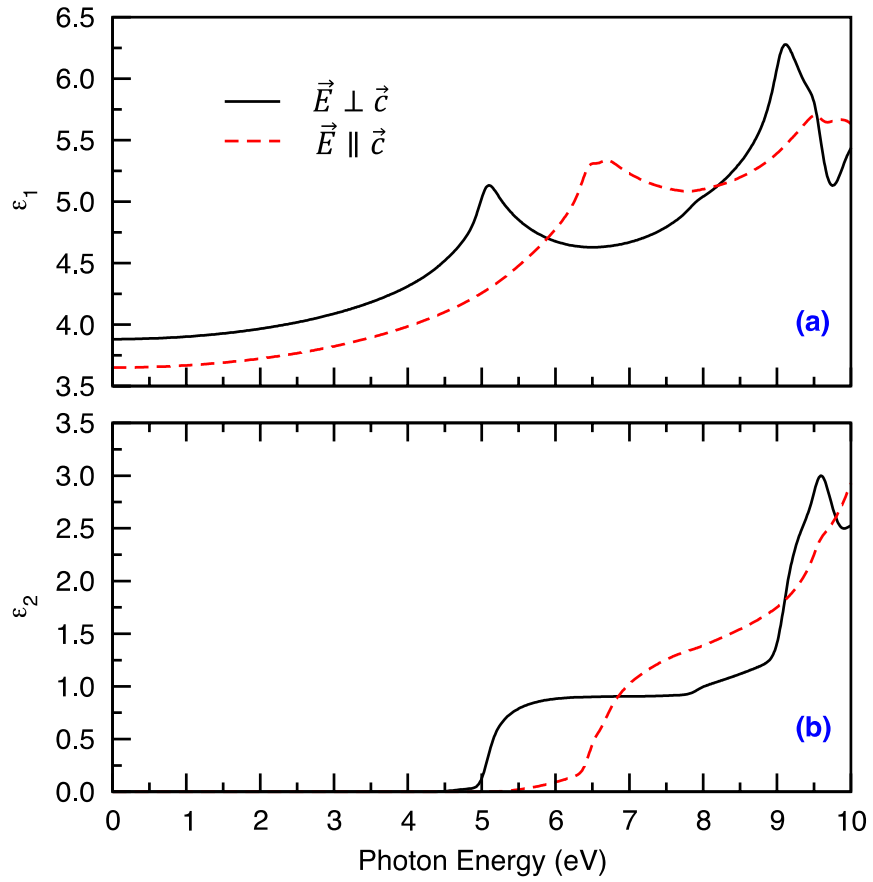
Figure 5.8: (a) Real and (b) imaginary part of the dielectric function of r-GeO$_2$ for electric-field polarizations along the two main crystallographic directions.
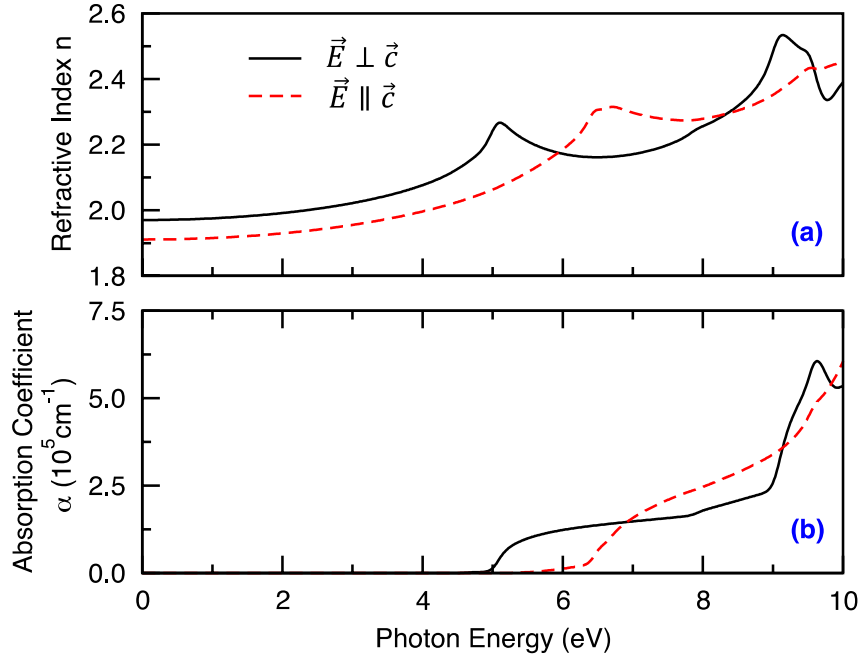
Figure 5.9: (a) Refractive index and (b) and absorption coefficient for the two main crystallographic directions of r-GeO$_2$.
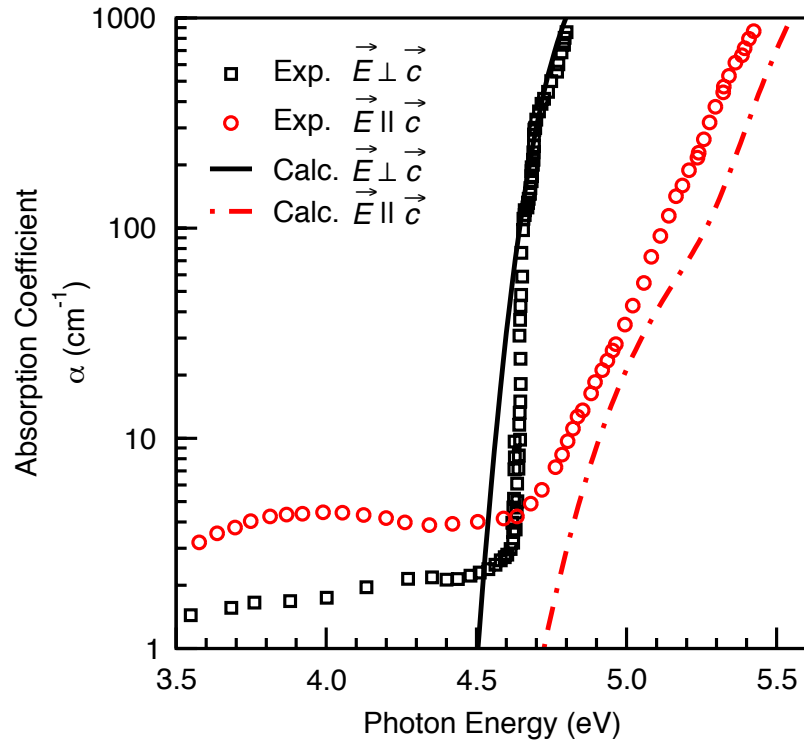


Figure 5.10: Comparison of our calculated (0 K simulation) absorption coefficient for r-GeO$_2$ along $\vec{E} \perp \vec{c}$ and $\vec{E} \parallel \vec{c}$ to experimental data from Stapelbroek *et al.* collected at 77 K (Ref. 7).

cellent solar-blind photoresponse for this material. To compare $\beta$-Ga$_2$O$_3$ directly to r-GeO$_2$, we examine their absorption coefficients at energies that are important for solar-blind applications. In the case of an annealed $\beta$-Ga$_2$O$_3$ film, the absorption coefficient ranges from $\sim$1-4$\times$10$^4$ cm$^{-1}$ for energies below the band gap and increases to $\sim$2$\times$10$^5$ cm$^{-1}$ at 5 eV (248 nm), for instance.[178] The cause of sub-band-gap absorption is the presence of defects and impurities.[34,178] In the present calculations on r-GeO$_2$ for the pristine, bulk crystal, $\alpha = 0$ cm$^{-1}$ for energies below the band gap. At 5 eV (0.56 eV above the calculated band gap), $\alpha = \sim$3$\times$10$^3$ cm$^{-1}$ for $\overrightarrow{E} \perp \overrightarrow{c}$, which is quite weak compared to the absorption coefficient at just 0.5 eV higher ($\sim$8$\times$10$^4$ cm$^{-1}$). The concentration of defects, impurities, and free carriers should be studied experimentally to better understand the ratio $\alpha_{E>4.28eV}/\alpha_{E<4.28eV}$ in real r-GeO$_2$ devices with defects and impurities for the purpose of solar-blind applications. An interesting similarity between $\beta$-Ga$_2$O$_3$ and r-GeO$_2$ is that each has an intrinsic feature in the band structure that suppresses optical absorption at the fundamental band gap. In the case of $\beta$-Ga$_2$O$_3$, the fundamental band gap is indirect, so absorption is weak until $\sim$30 meV above the band gap when the energy of the direct gap is reached.[78] As we have already shown for r-GeO$_2$, the electronic transition from the VBM to the CBM is forbidden, so absorption is suppressed for a 600 meV energy range until the second VB to CBM energy is reached. This behavior is notably different for dipole-allowed direct-gap materials such as GaN, for which the absorption coefficient increases strongly for energies above the band gap.[179] In contrast, the weak interband matrix elements of r-GeO$_2$ shift the absorption onset further into the UVC range, away from the solar-blind threshold of 290 nm. While $\beta$-Ga$_2$O$_3$ absorbs more strongly than r-GeO$_2$ since the first several optical transitions are dipole allowed, r-GeO$_2$ is more promising for solar-blind photodiodes because it can be ambipolarly doped and has lighter hole effective masses, which is indicative of high hole mobility.

## 5.5   CONCLUSIONS

In summary, we applied first-principles calculations to analyze the band structure, interband transitions, and optical properties in r-GeO$_2$ for potential applications in optoelectronic devices. We find a direct band gap of 4.44 eV at $\gamma$, while the carrier effective masses are similar to or smaller than other wide-band-gap semiconductors. Unlike many other wide-band-gap oxides, r-GeO$_2$ shows small hole self-trapping energy ($<$0.01 eV) that can be overcome at room tempertaure owing to their small effective mass. Our estimated exciton binding energies are in good agreement with

experiment. The optical matrix elements reveal that the transition from the top valence band to the conduction band minimum at $\gamma$ is forbidden, while the transition from the second VB to CBM is allowed for $\overrightarrow{E} \perp \overrightarrow{c}$ only. Absorption occurs for $\overrightarrow{E} \| \overrightarrow{c}$ starting at a higher energy of 6.65 eV. The short absorption onset wavelength of r-GeO$_2$ in addition to its semiconducting properties and ambipolar dopability support its applications as a UV-transparent conductor and in solar-blind photodetector devices.

# Transport within Rutile GeO$_2$: Charge Carrier Mobility and Thermal Conductivity

Rutile germanium dioxide (r-GeO$_2$) has a gap of 4.68 eV that places it among other ultrawide-band-gap semiconductors for potential uses in deep-ultraviolet optoelectronic and high-power-electronic devices. In either application, a high charge carrier mobility is desired to increase the electrical conductivity, and high thermal conductivity is desirable to remove generated waste heat. We use first-principles methods based on density functional and density functional perturbation theories to calculate the phonon dispersion of r-GeO$_2$. We analyze the electron- and hole-phonon coupling to understand how phonon absorption and emission via different phonon modes affects carrier scattering. Then, we theoretically predict the electron and hole mobility of r-GeO$_2$ as a function of temperature from 100 K to 1000 K at a carrier concentration of $10^{17}$ cm$^{-3}$. At 300 K, the carrier mobilities are $\mu_{elec}$ = 153.6 cm$^2$ V $^{-1}$ s$^{-1}$ ($\perp \overrightarrow{c}$), $\mu_{elec}$ = 74.1 cm$^2$ V $^{-1}$ s$^{-1}$ ($\| \overrightarrow{c}$), $\mu_{hole}$ = 4.7 cm$^2$ V $^{-1}$ s$^{-1}$ ($\perp \overrightarrow{c}$), and $\mu_{hole}$ = 2.2 cm$^2$ V $^{-1}$ s$^{-1}$ ($\| \overrightarrow{c}$). The thermal conductivities at 300 K are 37 W m$^{-1}$ K$^{-1}$ in-plane and 57 W m$^{-1}$ K$^{-1}$ out-of-plane, with a directional average of 44 W m$^{-1}$ K$^{-1}$. Last, we compare the Baliga's figure of merit (BFOM) for high-power-electronic applications and show that the BFOM for r-GeO$_2$ surpasses those of competing semiconductors.

## 6.1   INTRODUCTION

Power electronics are important for the control and conversion of electricity, but inefficiencies cause energy loss during each step in the conversion process, resulting in a combined efficiency of $\sim$80% or less.[180] In the United States, the existing electricity grid is outdated for modern electricity usage and must be replaced with power-conversion electronics that are able to control the power flow more efficiently. Ad-

dressing inefficiencies to improve energy sustainability motivates the ongoing search for new materials for power-electronics devices. Ultrawide-band-gap semiconductors with gaps wider than GaN (3.4 eV) have been the focus of power-electronics materials research.[19] Important material parameters to consider for power-electronics applications include the possibility of doping (usually $n$-type, but ambipolar dopability is also desirable for heteropolar devices), high carrier mobility $\mu$ for fast switching and efficient carrier transport, high thermal conductivity for efficient heat extraction, and a high critical dielectric breakdown field $E_C$ and dielectric constant $\epsilon_0$ to enable high-voltage operation. The Baliga figure of merit $BFOM=\frac{1}{4}\epsilon_0\mu E_C{}^3$ quantifies the performance of a material in power-electronic devices.[44,45] The $BFOM$ depends most strongly on the breakdown field, which increases superlinearly with increasing band gap and motivates the search for ultrawide-gap dopable semiconductors.

The $\beta$ polymorph of gallium oxide ($\beta$-Ga$_2$O$_3$) has been the recent focus of attention thanks to the availability of native substrates and the n-type dopability with Si or Ge.[19] While its electron mobility is lower than Si, SiC, or GaN, its ultrawide-band-gap of ~4.5 eV produces a high breakdown field and a $BFOM$ superior to these incumbent technologies.[20,52,58,78,181] However, its low thermal conductivity that prevents heat extraction and the impossibility of $p$-type doping (due to the formation of self-trapped hole polarons[85]) limit its applicability.[85,88,182] To overcome these challenges and advance the frontier of power electronics, new ultrawide-band-gap semiconducting materials must be identified and characterized.

Recently, Chae $et$ $al.$ found that rutile germanium dioxide (r-GeO$_2$) is a promising ambipolarly dopable semiconductor[153] with an ultrawide band gap (4.68 eV). Donors such as Sb$_{Ge}$ and F$_O$ are shallow (activation energy ~25 meV), while Al$_{Ge}$ and Ga$_{Ge}$ acceptors are deeper with ionization energies of ~0.4-0.5 eV. However, high acceptor concentrations, through the co-incorporation with hydrogen and subsequent annealing, can exceed the Mott-transition limit and enable $p$-type conduction. Rutile GeO$_2$ displays similar chemical and structural properties as rutile SnO$_2$, an established $n$-type transparent conductor.[152,157] However, the wider band gap of r-GeO$_2$ is promising for deep-ultraviolet (UV) luminescence and efficient power-electronics applications.[7,153,183] Yet, the carrier mobilities of r-GeO$_2$, and thus its viability and efficiency for power-electronics applications, remain unexplored.

In this work, we apply predictive atomistic calculations to determine the phonon-limited electron and hole mobilities of r-GeO$_2$ as a function of temperature and crystallographic orientation. We quantify the intrinsic phonon and carrier-phonon-coupling properties that impact carrier transport. Our results demonstrate that r-

GeO$_2$ exhibits a superior *BFOM* than current semiconductor technologies such as Si, SiC, GaN, and $\beta$-Ga$_2$O$_3$ in power-electronics applications.

## 6.2 COMPUTATIONAL METHODS

### 6.2.1 Electron and Hole Mobility

To accurately predict the electron and phonon properties of r-GeO$_2$, we use first-principles calculations based on density functional (DFT) and density functional perturbation theories (DFPT) within the Quantum ESPRESSO[62] code and the Boltzmann transport equation (BTE) within the EPW[184,185] code. Using the experimental lattice parameters $a = 4.4066$ Å and $c = 2.8619$ Å,[6] the band structure was calculated using the local-density approximation (LDA)[163,164] on the DFT level, and the eigenvalues were corrected with many-body perturbation theory using the G$_0$W$_0$ method as implemented in the BerkeleyGW software. Details for these calculations were previously reported.[183] The lattice parameters and atomic positions were relaxed for the phonon calculations to prevent imaginary phonon frequencies. The structural relaxation resulted in the lattice parameters $a = 4.516$ Å and $c = 2.978$ Å, which differ from the experimental values[6] by 2.5% and 4.1%, respectively. Both the electronic band structure and phonon dispersion were calculated on 4×4×6 Brillouin zone (BZ) sampling grids, using the charge density generated on an 8×8×12 BZ sampling grid for higher accuracy. Within EPW, the velocity operator[135,186] was utilized to evaluate the carrier velocities, and since r-GeO$_2$ is a polar material, the electron-phonon coupling matrix elements $g$ were calculated including the Fröhlich correction.[187] The electronic transport module was used to calculate the electron and hole mobilities over a wide temperature range from 100 K to 1000 K at a carrier concentration of $10^{17}$ cm$^{-3}$.[188] The electron and hole mobilities were converged for fine electron and phonon BZ sampling grids of 120×120×180. We sampled states within energy windows of 225 meV around the electron and hole Fermi energies, which accounts for energy differences during scattering of up to $\hbar\omega_{max}+5k_B T$ at room temperature, where $\hbar\omega_{max}$ is the highest polar optical phonon energy and $k_B$ is the Boltzmann constant.[189]

### 6.2.2 Thermal Conductivity

Our calculation for the thermal conductivity is based on the full Boltzmann transport equation (BTE) as implemented in the almaBTE software.[94] Necessary inputs for this calculation include the atomic structure information, the second-order and third-

order interatomic force constants (IFCs), and the Born effective charges (since r-GeO$_2$ is a polar material).[190] The IFCs were calculated within Quantum ESPRESSO[62] using density functional and density functional perturbation theories (DFT and DFPT) under the local-density approximation (LDA).[163,164] The difference between these calculations and those conducted for the charge carrier mobility is that a Ge$^{4+}$ (3$d$ electrons in the valence) rather than Ge$^0$ pseudopotential was used. The O pseudopotential includes the 2$s$ and 2$p$ electrons in the valence. The plane wave cutoff energy of 140 Ry converges the total energy of the system to within 1 mRy/atom. First, the experimental lattice parameters[6] $a$ = 4.4066 Å and $c$ = 2.8619 Å were relaxed until the total pressure in the unit cell was 0.01 kbar. The relaxed parameters $a$ = 4.3736 Å and $c$ = 2.8674 Å differ from experiment by only 0.7% and 0.2%, respectively. The electronic structure and phonon dispersion were calculated on a 6×6×9 Brillouin zone (BZ) sampling grid, thus producing second order IFCs on the same supercell size. As necessitated by the almaBTE software, the second-order IFCs were calculated without the non-analytical term correction (NAC), however, the NAC was applied to obtain the Born effective charges. The third-order IFCs were calculated using finite displacements on a 4×4×4 supercell by manually shifting select atoms and calculating the produced forces on surrounding atoms. A 0.5 nm nearest-neighbor distance cutoff was applied. The calculated relaxed structure, IFCs, and Born effective charges were applied within the almaBTE software, where an 18×18×27 BZ sampling grid was used to calculate the thermal conductivity of r-GeO2.

## 6.3   RESULTS AND DISCUSSION

### 6.3.1   Electron and Hole Mobility

In addition to the electronic band structure, the charge carrier mobility of a material depends heavily on the phonon dispersion.[191] Figure 6.1 shows the wave vector dependence of each mode along the $\perp \vec{c}$ and $\| \vec{c}$ directions. The minimum optical phonon frequency occurs at $\Gamma$ with a frequency of 98 cm$^{-1}$. In the in-plane direction, all phonon modes with frequencies above 179 cm$^{-1}$ are optical modes, while the acoustic modes extend to a higher frequency (391 cm$^{-1}$) in the out-of-plane direction. Table 6.1 lists the phonon frequencies of all modes, including the transverse optical (TO) and longitudinal optical (LO) splitting for each of the four infrared (IR)-active modes. Also shown is additional data from two computational studies and three experimental studies. In 1970, Scott published the first polarized Raman spectra for r-GeO$_2$ as well as the corresponding symmetry assignments.[17] Mernagh *et al.* pub-

lished the temperature dependence of the Raman spectrum nearly 30 years later with excellent agreement (within 4 cm$^{-1}$).[192] The $E_g$ frequency is notably different ($+21\%$) from the predicted value. Recently, Sanson *et al.* reexamined the Raman spectra via careful control over the crystal orientation and detected this peak at 525 cm$^{-1}$, which differs from our calculated $E_g$ peak value by only 2%. This additional information resolved the uncertainty in analysis of the four Raman-active modes of r-GeO$_2$. One discrepancy between our calculations and other reports is the Raman-active B$_{1g}$ frequency, which is $\sim40\%$ lower from our calculations versus other reports. Samanta *et al.* notably calculate a value more similar to ours ($\sim10\%$ different).[13] Their analysis of strain effects on the r-GeO$_2$ lattice shows that the phonon dispersion changes noticeably with a change in lattice volume (especially for the B$_{1g}$ mode) and can help explain the difference in our calculation and other reports as our relaxed lattice constants are larger than the experimental values.

One year after Scott reported the Raman data, the IR spectra including LO-TO splitting became available for the first time by Kahan *et al.*[15] All four LO-TO pairs were identified. Other reports came after but have been incomplete. The study by Madon *et al.* shows very ambiguous IR peaks, making it impossible to identify peak position properly.[193] Kaindl *et al.* made both IR and Raman measurements, however not all optical peaks were identified.[14] In Table 6.1, we assigned the three E$_u$ LO-TO pairs measured by Kahan *et al.* in order of increasing value. However, the frequencies of 652 cm$^{-1}$ and 680 cm$^{-1}$ are significantly higher than our calculations and those of the other theoretical reports, and to the best of our knowledge, no other experimental reports have identified the values for these IR modes. The reported experimental TO (LO) mode is 44% (41%) larger than our calculation. A lack of available studies with all IR peaks observed points toward the difficulty of this measurement in r-GeO$_2$ or perhaps that there have been limited efforts put toward this potential high-power electronic material. Nevertheless, phonon frequencies play a critical role in material properties such as charge carrier mobility and thermal conductivity and should be resolved. The limited experimental data on the IR spectrum of r-GeO$_2$ leaves the final analysis of the LO-TO peak positions open for future work.

We analyzed the phonon-mode-dependent carrier-phonon coupling to understand carrier scattering by phonons in r-GeO$_2$. We first determined the carrier-phonon coupling matrix elements for the bottom conduction and top valence bands for wave vectors along the $\Gamma$—X and $\Gamma$—Z directions [Figure 6.2 (a,d)]. Our results show that polar optical modes exhibit the strongest carrier-phonon coupling, as expected in polar materials. However, the higher-frequency modes are not as effective at scat-
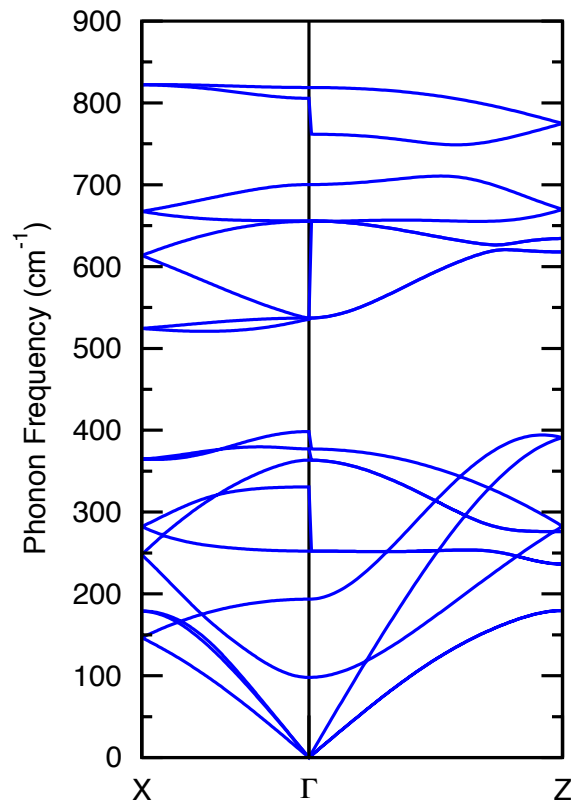
Figure 6.1: Phonon dispersion of rutile GeO$_2$ along the $\Gamma$ —X ($\overrightarrow{c}$) and $\Gamma$ —Z ($\overrightarrow{c}$) directions, including LO-TO splitting.

| Mode Type | Activity | Present work | (a) | (b) | (c) | (d) | (e) | (f) |
|---|---|---|---|---|---|---|---|---|
| | | Calculated | | | Experimental | | | |
| $B_{1g}$ | R | 97.96 | 109 | 182 | 170 | | 171 | 170 |
| $B_{1u}$ | — | 193.56 | 211 | 219 | | | | |
| $E_u$ | I (TO) | 252.32 | 293 | 317 | | 334 | | |
| $E_u$ | I (LO, $\Gamma \rightarrow X$) | 330.7 | | 362 | | 484 | | |
| $E_u$ | I (TO) | 363.49 | 383 | 364 | | 652 | | |
| $E_u$ | I (LO, $\Gamma \rightarrow X$) | 398.42 | | 474 | | 680 | | |
| $A_{2g}$ | — | 377.13 | 447 | 479 | 476 | | | |
| $A_{2u}$ | I (TO) | 535.35 | 543 | 521 | 496 | 522 | | |
| $A_{2u}$ | I (LO, $\Gamma \rightarrow Z$) | 761.8 | | 801 | 792 | 816 | | |
| $E_g$ | R | 537.11 | 549 | 546 | | | 525 | ~680[a] |
| $B_{1u}$ | — | 655.21 | 553 | 672 | 680, 687 | | | |
| $E_u$ | I (TO) | 655.96 | 679 | 665 | 648 | 709 | | |
| $E_u$ | I (LO, $\Gamma \rightarrow X$) | 805.64 | | 837 | 849 | 852 | | |
| $A_{1g}$ | R | 700.22 | 693 | 711 | 700 | | 700 | 702 |
| $B_{2g}$ | R | 818.86 | 880 | 869 | 874 | | 873 | 870 |

[a]There is uncertainty in the exact value and assignment of this peak because it is a shoulder off of the dominating $A_{1g}$ peak.

Table 6.1: Calculated phonon frequencies (in cm$^{-1}$) at $\Gamma$ for r-GeO$_2$. The activity of each mode is indicated as R (Raman-active), IR (infrared-active), or — (silent). The TO and LO frequencies for the IR-active modes, including the direction of splitting, are indicated. Our theoretical values are compared to other computed results by (a) Samanta *et al.*[13] and (b) Kaindl *et al.*[14] as well as several experimental results by (c) Kaindl *et al.*[14], (d) Kahan *et al.*[15], (e) Sanson *et al.*[16], and (f) Scott[17].

tering carriers; they either require high temperatures to enable appreciable phonon occupation numbers and scatter carriers by phonon absorption or high carrier energies to scatter electrons to lower-energy states by phonon emission. Taking the thermal occupation of phonon modes at room temperature ($k_B T$=26 meV) into account, we find the dominant modes for phonon-absorption [$g^2 n_q$, Figure 6.2 (b,e)] and phonon-emission [$g^2(n_q+1)$, Figure 6.2 (c,f)] carrier scattering. Electrons and holes most strongly absorb the polar-optical LO modes with frequencies of 44, 50, 95, and 101 meV. Electrons also strongly absorb the transverse-acoustic (TA) modes. As with phonon absorption, carriers scatter most strongly by phonon emission by the polar-optical LO phonons as well as the Raman-active modes at 85 meV and 100 meV. However, the frequencies of most of these phonon modes are high, and carriers are unlikely to possess sufficient thermal energy near room temperature to emit such phonons and scatter to lower-energy states. We thus predict that holes primarily scatter by absorption of the $A_{2u}$ and the three $E_u$ LO modes and emission of the two lower-frequency $E_u$ LO modes at 44 and 50 meV, while electrons are additionally scattered strongly by the TA modes.

We next discuss the mobility obtained from the iterative solution of the BTE. Figure 6.3 shows the convergence of the electron (a) and hole (b) mobilities at 300 K along both crystallographic axes as a function of electron and phonon BZ sampling. We apply a linear extrapolation based on the two finest grids and extrapolate the mobilities with infinite BZ sampling. The converged carrier mobilities at 300 K are $\mu_{elec} = 154$ cm$^2$ V$^{-1}$ s$^{-1}$ ($\perp \vec{c}$), $\mu_{elec} = 74$ cm$^2$ V$^{-1}$ s$^{-1}$ ($\| \vec{c}$), $\mu_{hole} = 5$ cm$^2$ V$^{-1}$ s$^{-1}$ ($\perp \vec{c}$), and $\mu_{hole} = 2$ cm$^2$ V$^{-1}$ s$^{-1}$ ($\| \vec{c}$). Qualitatively, we expect a lower mobility for transport directions in which carriers have more than one strong perpendicular scattering direction. Our carrier-phonon coupling results show that carrier scattering in r-GeO$_2$ is stronger for scattering along Γ—X than Γ—Z, which indicates that the carrier mobility is higher for in-plane ($\perp \vec{c}$) than out-of-plane ($\| \vec{c}$) transport since the carriers propagating along $\vec{c}$ have two strong scattering (Γ—X) directions, while carriers propagating $\perp \vec{c}$ have one stronger (Γ—X) and one weaker (Γ—Z) scattering direction. This analysis is validated by our calculated carrier mobilities, which demonstrate that the electron and hole mobilities are approximately twice as high along $\perp \vec{c}$ than $\| \vec{c}$.

Typically, the polar-optical modes limit the room temperature mobility in oxide materials, but our electron-phonon coupling results combined with the mobility calculations indicate that the acoustic modes must play a larger role for r-GeO$_2$. This is consistent with the results of Samanta *et al.*, who found a strong sensitivity of the
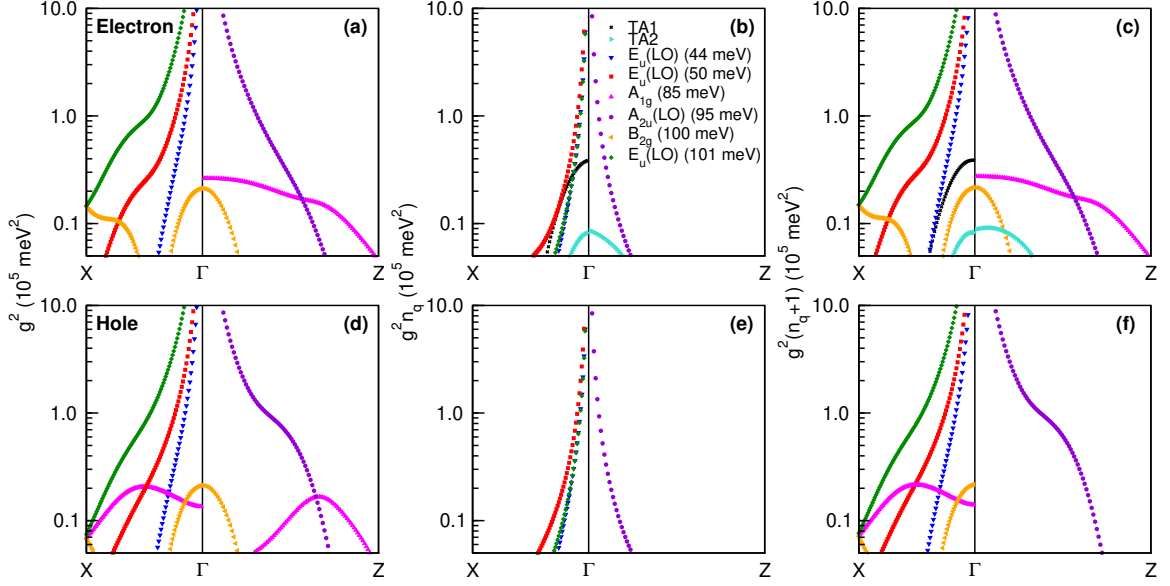
Figure 6.2: (a-c) Square of the intraband electron-phonon coupling matrix element g and scattering of electrons via phonon absorption $(g^2_{el-ph} n_q)$ and phonon emission $(g^2_{el-ph}(n_q+1))$ for the bottom conduction band from $\Gamma$ to $q$ as a function of the phonon wave vector $q$ along the $\Gamma$—X $(\perp \overrightarrow{c})$ and $\Gamma$—Z $(\parallel \overrightarrow{c})$ directions, showing the phonon modes with the largest coupling strengths. Phonon occupations are calculated using room temperature $(k_B T = 26$ meV). Panels (d-f) contain the same information for hole-phonon interactions (*i.e.* the top valence band). All four IR-active modes show strong electron or hole-LO-phonon (polar-optical) coupling near $\Gamma$, while the strongest-coupled Raman-active modes show a weak dependence with respect to $q$ (optical deformation potential coupling).
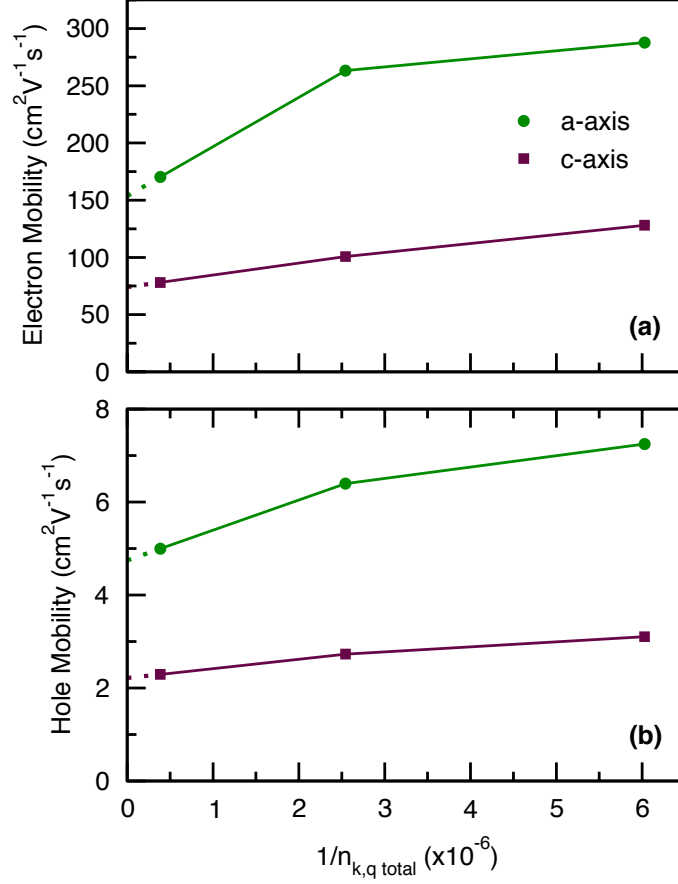
Figure 6.3: (a) Electron and (b) hole mobility $\mu$ of r-GeO$_2$ at 300 K along the $a$-axis $(\perp \vec{c})$ and $c$-axis $(\| \vec{c})$ directions as a function of the inverse of the total number of electron and phonon Brillouin-zone sampling points (the two grids are equally dense in each calculation) for carrier densities of $10^{17}$ cm$^{-3}$. The extrapolated room-temperature mobility values for rutile GeO$_2$ for infinitely fine sampling grids (dotted lines) are $\mu_{elec} = 153.6$ cm$^2$ V$^{-1}$ s$^{-1}$ $(\perp \vec{c})$, $\mu_{elec} = 74.1$ cm$^2$ V$^{-1}$ s$^{-1}$ $(\| \vec{c})$, $\mu_{hole} = 4.7$ cm$^2$ V$^{-1}$ s$^{-1}$ $(\perp \vec{c})$, and $\mu_{hole} = 2.2$ cm$^2$ V$^{-1}$ s$^{-1}$ $(\| \vec{c})$.

| Parameters | Electron, $\perp \vec{c}$ | Electron, $\parallel \vec{c}$ | Hole, $\perp \vec{c}$ | Hole, $\parallel \vec{c}$ |
|:---:|:---:|:---:|:---:|:---:|
| $a$ | $4.46 \times 10^{-7}$ | $1.26 \times 10^{-6}$ | $6.99 \times 10^{-5}$ | $1.02 \times 10^{-3}$ |
| $b$ | $4.27 \times 10^{-14}$ | $1.61 \times 10^{-13}$ | $1.32 \times 10^{-10}$ | $9.61 \times 10^{-10}$ |
| $n$ | 1.66 | 1.62 | 1.34 | 0.99 |
| $m$ | 3.77 | 3.64 | 3.48 | 3.30 |

Table 6.2: Fitted parameters for the power-law resistivity model given by $\mu(T) = 1/(aT^n + bT^m)$ where $\mu$ is in units of cm$^2$ V$^{-1}$ s$^{-1}$ and $T$ in K to describe the mobility versus temperature for electrons and holes along the two main crystallographic directions.

band gap on strain (*i.e.*, acoustic deformation).[13] Figure 6.4 shows the temperature dependence of the mobility, including a power-law resistivity model fit to each curve. From Matthiessen's rule, we set the mobility as the sum of two resistivity contributions:

$$\mu(T) = 1/(aT^n + bT^m), \tag{6.1}$$

where $a$, $b$, $n$, and $m$ correspond to fitting parameters. Table 6.2 shows the values obtained for each carrier and direction. We find that at all temperatures studied (100 K to 1000 K) and for both crystal directions, the $aT^n$ term dominates the electron mobility. This is visualized in Figure 6.4, which shows the calculated mobility data along with the $aT^n$ and $bT^m$ terms. The value of $n$ for electrons is approximately 3/2, which is typically associated with deformation-potential acoustic-phonon scattering. Visually, the slope of the electron $\mu(T)$ appears constant (Figure 6.4), which indicates that acoustic phonons dominate carrier scattering at all investigated temperatures. For the holes, however, there is an obvious change in slope for the hole mobility from the $aT^n$ term (with an exponent similar to 3/2 for acoustic-phonon scattering) that dominates below 473 K along $\perp \vec{c}$ (413 K for $\parallel \vec{c}$) to the $bT^m$ term (with an exponent of $\sim$3, characteristic of optical-phonon scattering) dominating at higher temperatures (Figure 6.4). Our mobility results are consistent with the carrier-phonon coupling data (Figure 6.2), which show that acoustic-phonon scattering is weaker for holes than for electrons and only dominates at low temperatures.

## 6.3.2 Thermal Conductivity

Phonon transport is the fundamental physics phenomenon which governs heat transport in a crystal. Thus, to guide the analysis of experimental thermal conductivity measurements from the atomic level, we compute the phonon dispersion of r-GeO$_2$
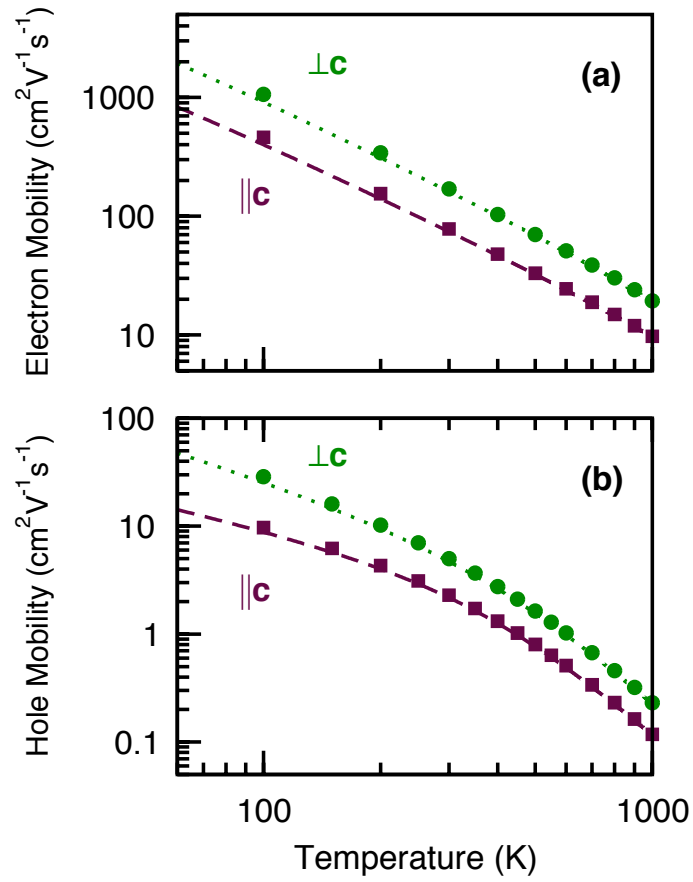
Figure 6.4: Electron and hole mobility $\mu$ of r-GeO$_2$ along the $\perp \vec{c}$ and $\| \vec{c}$ directions as a function of temperature for a carrier concentration of $n = 10^{17}$ cm$^{-3}$.
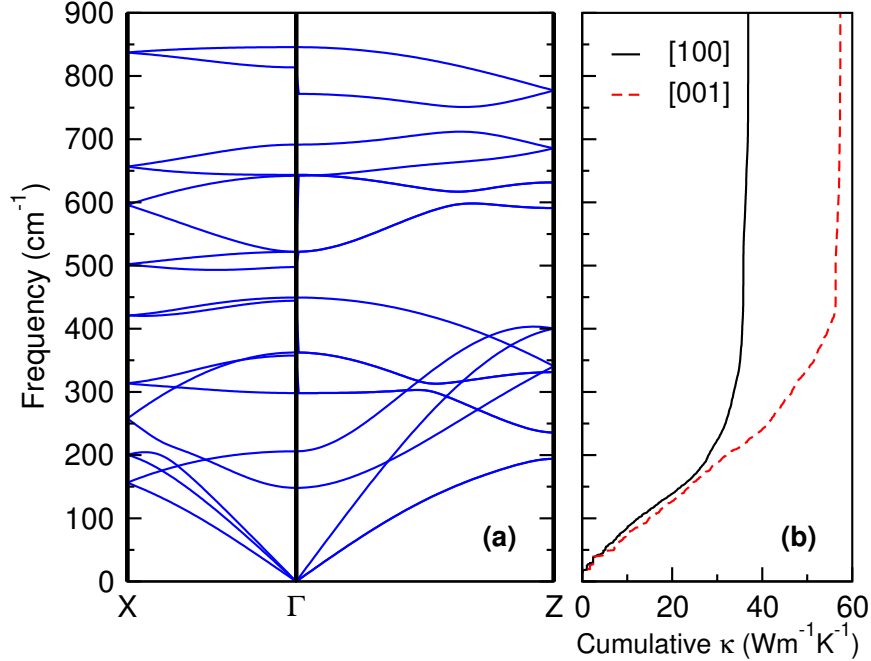
Figure 6.5: (a) Phonon dispersion of r-GeO$_2$, including polar LO-TO splitting, and (b) cumulative thermal conductivity at 300 K along the in-plane (Γ—X) and out-of-plane (Γ—Z) directions. The acoustic modes appear to have the largest contribution to thermal conductivity in both crystallographic directions. At the highest phonon frequencies in each direction, the maximum thermal conductivities are reached: 37 W m$^{-1}$ K$^{-1}$ in-plane and 57 W m$^{-1}$ K$^{-1}$ out-of-plane.

as shown in Figure 6.5(a). Polar effects from the crystal structure are included via the NAC, and Born effective charges of 4.45 (Ge) and -2.23 (O) are obtained. Significant LO-TO splitting at Γ is observed for the four IR-active modes, with three of the modes splitting in the Γ—X direction and one in the Γ—Z direction. An interesting feature of the phonon dispersion is that the acoustic mode frequencies in the Γ—Z direction extend to twice the values of the Γ—X direction, with maximum values in each direction equal to 400.14 cm$^{-1}$ and 204.55 cm$^{-1}$, respectively. At the edge of the BZ along Γ—Z, the frequency of the longitudinal-acoustic (LA) mode surpasses those of six optical modes.

Figure 6.5(b) shows how the thermal conductivity $\kappa$ increases with the activation of each phonon mode at 300 K. While several optical modes are mixed with the acoustic modes near the zone edges, a significant portion of the total cumulative thermal conductivity is reached at the maximum acoustic frequencies. Along [100], 77% of the total thermal conductivity is reached by the frequency 204.55 cm$^{-1}$. The percentage is even larger along [001], with 95% of the total thermal conductivity achieved by 400.14 cm$^{-1}$. There is a large phonon band gap between this mode and

97
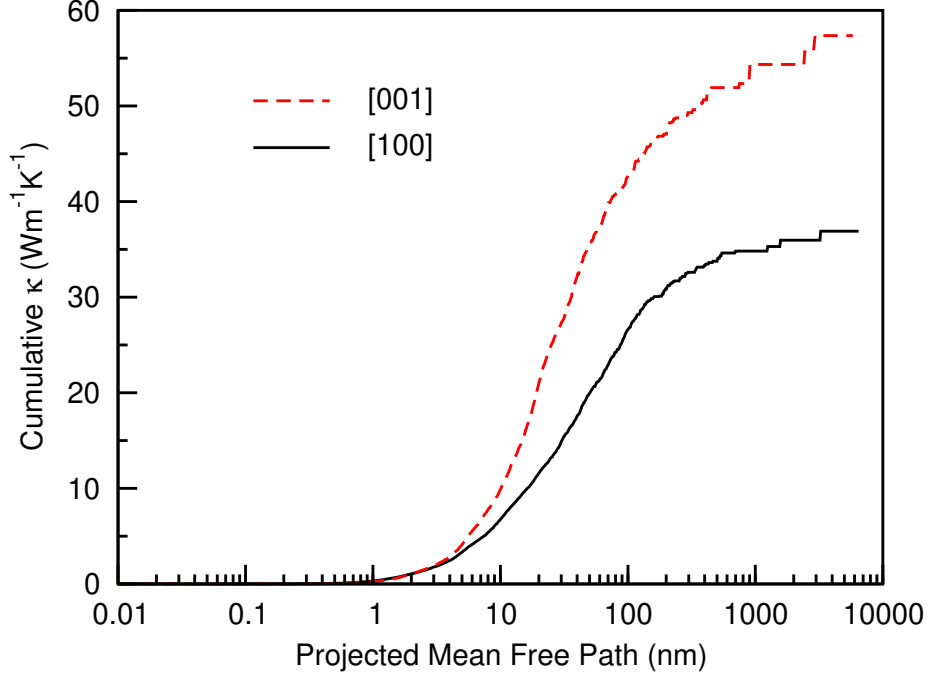
Figure 6.6: Cumulative thermal conductivity of r-GeO$_2$ at 300 K as a function of the phonon mean free path. The maximum thermal conductivity along each direction is reached at mean free paths of 3.3 $\mu$m (in-plane) and 2.9 $\mu$m (out-of-plane).

the next lowest mode in this direction of 191 cm$^{-1}$ (24 meV) at the zone edge. We have not conducted a mode-specific analysis for $\kappa$ within the range of frequencies where optical and acoustic modes mix, however, determining the individual contributions of each phonon mode is an interesting avenue for future work. The maximum thermal conductivity at 300 K is 37 W m$^{-1}$ K$^{-1}$ along [100] and 57 W m$^{-1}$ K$^{-1}$ along [001], resulting in a directional average of 44 W m$^{-1}$ K$^{-1}$.

Another useful analysis of the cumulative thermal conductivity is how $\kappa$ increases with phonon mean free path (MFP). Such a consideration is important in the event that a device incorporates a thin (or ultra-thin) layer of r-GeO$_2$ such that its phonon MFP is limited compared to the bulk case. This is also crucial for devices that contain polycrystalline r-GeO$_2$ rather than single crystalline material. In this case, the grain size is important to consider, and is the case of our experimental sample. The r-GeO$_2$ sample used in our experimental thermal conductivity measurements is polycrystalline with an average grain size of $\sim$1 $\mu$m (with individual grains ranging from 200 nm to 2 $\mu$m). Figure 6.6 shows how the thermal conductivity at 300 K increases in both the [100] and [001] directions with increasing phonon MFP. Along $\Gamma$—X ($\Gamma$—Z), the maximum $\kappa$ is reached at 3.3 $\mu$m (2.9 $\mu$m). With this information, we can conclude that our measured thermal conductivity is just short of $\kappa_{bulk}$.
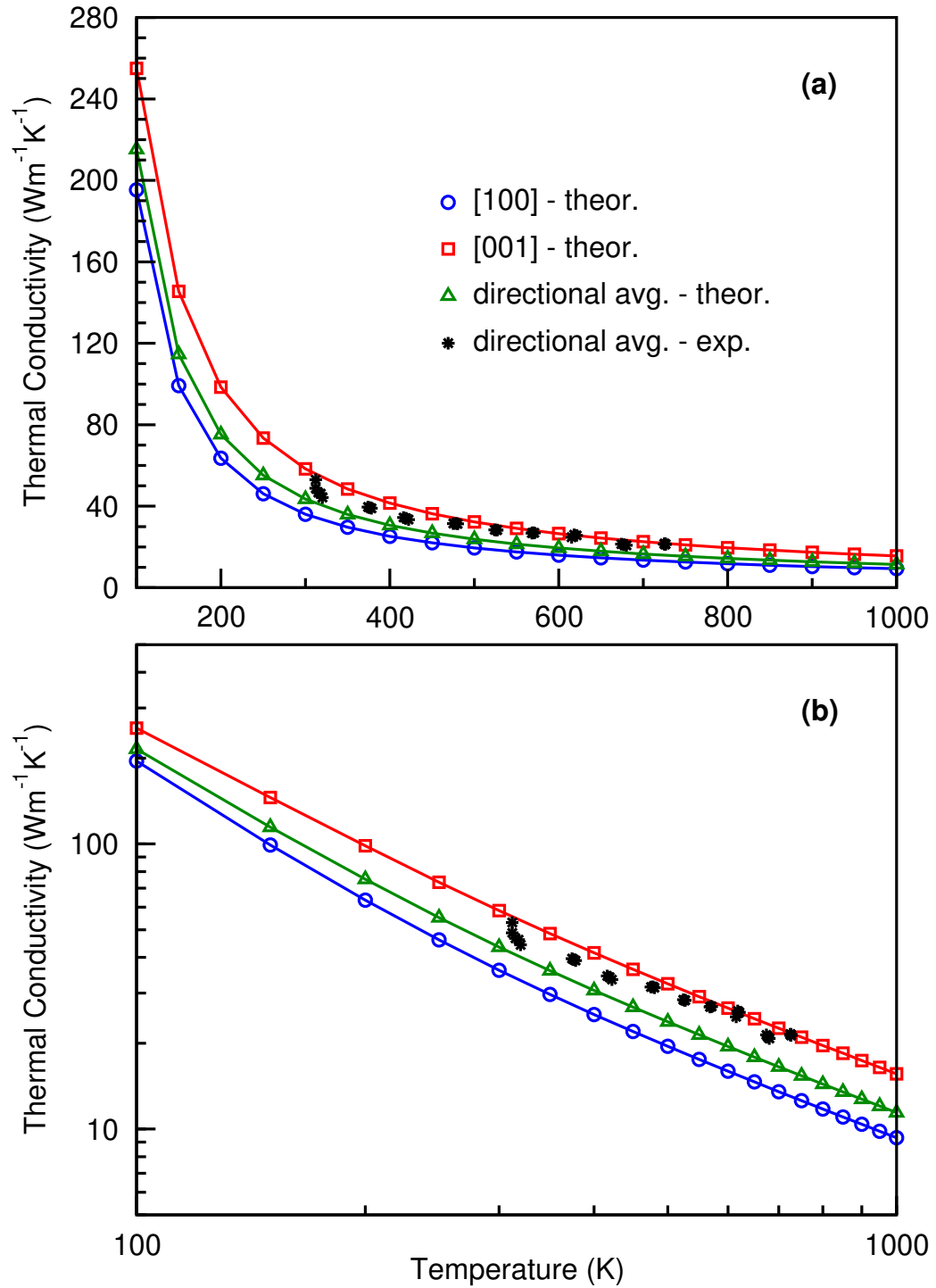
Figure 6.7: Experimental and theoretical thermal conductivity from 100 K to 1000 K in (a) linear scale and (b) log-log scale. The theoretical $\kappa$ was calculated along both crystallographic directions, with $\kappa_{avg} = \frac{2}{3}\kappa_a + \frac{1}{3}\kappa_c$. Experimental measurements were performed on a polycrystalline r-GeO$_2$ sample with grain sizes ranging from 200 nm to 2 $\mu$m.

Last we calculate how the thermal conductivity of r-GeO$_2$ changes with temperature and compare to our experimentally measured values. Figure 6.7 shows the calculated thermal conductivity from 100 K to 1000 K along the [100] and [001] directions as well as the crystallographically averaged values ($\kappa_{avg} = \frac{2}{3}\kappa_a + \frac{1}{3}\kappa_c$). As expected, $\kappa$ depends on temperature as $\propto T^{-1}$, which can be visualized in Figure 6.7(a). Figure 6.7(b) contains the same $\kappa$ versus $T$ data but in log-log scale to clearly show the values at high temperature. Our experimental measurements were conducted between 312 K to 726 K and are plotted against the theoretical predictions for comparison. The experimental data fall just above the theoretical directional average curve. Since experimental samples always contain defects and impurities, we would expect the measured $\kappa$ to be slightly lower than the calculated $\kappa$, but we see the opposite occur. This error could be due to the calculated interatomic force constants or phonon dispersion. If we compare the phonon frequencies calculated with the Ge$^0$ pseudopotential as in Figure 6.1 to that calculated with the Ge$^{4+}$ ion pseudopotential (Figure 6.5), there are noticeable differences. First, the lowest optical frequency at $\Gamma$ in the Ge$^0$ phonon dispersion occurs near 100 cm$^{-1}$ but near 150 cm$^{-1}$ for the Ge$^{4+}$ dispersion. Another significant difference is in the full-zone phonon band gap of just over 100 cm$^{-1}$ (between ∼400 cm$^{-1}$ and ∼500 cm−1) for the Ge$^0$ calculation but a much smaller gap of less than 50 cm$^{-1}$ in the Ge$^{4+}$ dispersion. These differences could indicate that one Ge pseudopotential is better for calculating the structural properties of r-GeO$_2$. A more thorough analysis of the effects of the chosen pseudopotentials could be conducted in the future.

### 6.3.3 Baliga Figure of Merit

Electron and hole mobility as well as thermal conductivity are important material parameters to consider for any semiconductor that will be incorporated into an electrical device. Materials used in high-power electronic devices require a large band gap to enable a large dielectric breakdown field. Baliga's figure of merit ($BFOM$) for potential high-power materials at low frequencies is given as:

$$BFOM = \frac{1}{4}\epsilon_0 \mu E_C^3, \tag{6.2}$$

where $\epsilon_0$ is the static dielectric constant and $E_C$ is the critical dielectric breakdown field.[44,45] The ultrawide-band-gap of r-GeO$_2$ (4.68 eV)[7] makes the material especially suited for high-power and high-temperature applications.[153,183] Table 6.3 lists the material parameters of r-GeO$_2$ relevant for $n$-type power electronics and compares

| Material | Static dielectric constant, $\epsilon_0$ | Electron mobility, $\mu$ (cm$^2$ V$^{-1}$ s$^{-1}$) | Dielectric breakdown field, $E_C$ (MV cm$^{-1}$) | BFOM (10$^6$ V$^2$ $\Omega^{-1}$ cm$^{-2}$) |
|---|---|---|---|---|
| Si | 11.9 [ 198 ] | 1240 (d) [ 195 ] | 0.3 [ 52 ] | 8.8 |
| 4H-SiC | 9.7 [ 195 ] | 980 (d) [ 195 ] | 2.5 [ 52 ] | 3,300 |
| GaN | 10.4 ($\parallel \vec{c}$) [ 199 ] | 1000 (d) [ 196 ] | 3.3 [ 52 ] | 8,300 |
| $\beta$-Ga$_2$O$_3$ | 10.0 [ 200 ] | 180 (H) [ 194 ] | 6.4$^a$ [ 52 ] | 10,000 |
| | | 80 (d) [ 115 ] | | 4,400 |
| r-GeO$_2$ | 14.5 ($\perp \vec{c}$) [ 201 ] | 153.6 (d) | 7.0$^a$ | 17,000 |

$^a$The breakdown fields $E_C$ of $\beta$-Ga$_2$O$_3$ ($E_g = 4.5$ eV) and r-GeO$_2$ ($E_g = 4.68$ eV) are estimated using the breakdown field versus band gap curve by Higashiwaki *et al.*[52]

Table 6.3: Baliga's figure of merit (BFOM $= \frac{1}{4}\epsilon_0 \mu E_C^3$) for silicon and common ultrawide-band-gap semiconductors. Electron mobilities and dielectric breakdown fields for all materials are for carrier densities of $10^{16}$ cm$^{-3}$ except those of $\beta$-Ga$_2$O$_3$ ($10^{12}$ cm$^{-3}$ for $\mu_{Hall}$ and $10^{17}$ cm$^{-3}$ for $\mu_{drift}$) and r-GeO$_2$ ($10^{17}$ cm$^{-3}$). Mobilities are designated as drift (d) or Hall (H) mobilities.

them to incumbent technologies. The breakdown fields of $\beta$-Ga$_2$O$_3$ (with a gap of 4.5 eV) and r-GeO$_2$ are evaluated using the breakdown field versus band gap relation by Higashiwaki *et al.*[52] The electron mobility of r-GeO$_2$ is lower than Si, SiC, and GaN by over 80%[194–196] but higher than $\beta$-Ga$_2$O$_3$. Although the experimental electron mobilities of Ga$_2$O$_3$ have typically been obtained with Hall measurements, it is the drift mobility that should be applied to evaluate the *BFOM*. A drift mobility of 80 cm$^2$ V$^{-1}$ s$^{-1}$ was measured[115] in $\beta$-Ga$_2$O$_3$ at 300 K, while the highest Hall mobility at 300 K is 184 cm$^2$ V$^{-1}$ s$^{-1}$.[194,197] However, if the Hall factor at 300 K ($r_H$=1.68)[91] is applied to convert the Hall to drift mobility ($\mu_{Hall}=\mu_{drift}r_H$), the highest measured room-temperature drift mobility of Ga$_2$O$_3$ is 109 cm$^2$ V$^{-1}$ s$^{-1}$. Overall, r-GeO$_2$ displays the largest *BFOM* out of the materials considered here as it exhibits the largest $E_C$ value (since it has the widest band gap) the highest $\epsilon_0$, and a higher electron mobility than Ga$_2$O$_3$. The combination of a higher *BFOM* with the prediction of $p$-type doping and the possibility of hole conduction demonstrate the promise of r-GeO$_2$ as a superior semiconductor compared to incumbent technologies such as $\beta$-Ga$_2$O$_3$ for high-power electronic applications.

## 6.4 CONCLUSIONS

Transport in materials is critical to consider and understand for applications in electrical devices. We analyze and report for the first time two intrinsic and fundamental transport properties of rutile germanium dioxide: electron and hole mobility and thermal conductivity.

Charge carrier mobility is an important material parameter for many device applications. We calculate the phonon dispersion and compare our results to other theo-

retical and experimental phonon frequencies. The electron and hole-phonon coupling are determined in the $\perp \vec{c}$ and $\parallel \vec{c}$ directions, and we show via a two-power-law model that acoustic scattering dominates for all temperatures (100 K to 1000 K) for electrons and only at temperatures below ~450 K for holes. Using the Boltzmann transport equation, we reveal the temperature dependence of the charge carrier mobilities and provide insights on the phonon-scattering mechanisms for both electrons and holes. Both the electron and hole mobilities for r-GeO$_2$ are reasonably large to qualify the material as an outstanding competitor to other wide-band-gap semiconductors, especially since its dielectric breakdown field is larger than other competing materials such as Si, SiC, GaN, and $\beta$-Ga$_2$O$_3$. We calculate the BFOM for r-GeO$_2$ to be $17{,}000 \times 10^6$ V$^2$ $\Omega^{-1}$ cm$^{-2}$, which is more than double that of GaN and nearly four times larger than that of $\beta$-Ga$_2$O$_3$ if the drift mobility rather than Hall mobility is considered.

We also use the Boltzmann transport equation for phonons to estimate the thermal transport in r-GeO$_2$. Our calculations at 300 K show that the maximum thermal conductivity is 37 W m$^{-1}$ K$^{-1}$ along [100] and 57 W m$^{-1}$ K$^{-1}$ along [001] (directional average of 44 W m$^{-1}$ K$^{-1}$). We also plot experimental data collected using a polycrystalline r-GeO$_2$ sample (200 nm to 2 $\mu$m grain sizes) and show that it agrees well with our calculations. When we compare our calculated thermal conductivity to a major competing material for high-power-electronic applications, $\beta$-Ga$_2$O$_3$, we show that r-GeO$_2$ has the higher $\kappa$. Thus, not only are the electron and hole mobilities or r-GeO$_2$ larger than those of $\beta$-Ga$_2$O$_3$, but we also show that the thermal conductivity is higher. At 300 K (for instance), even the smallest value of $\kappa$ for r-GeO$_2$ (37 W m$^{-1}$ K$^{-1}$) is still larger than the highest value of $\kappa$ for $\beta$-Ga$_2$O$_3$ (27 W m$^{-1}$ K$^{-1}$).[5] The ability to dissipate heat quickly is important to consider for materials that will be used in devices operating at high voltages or frequencies which generate waste heat as a consequence.

Our first-principles results for the transport properties of r-GeO$_2$ indicate that this material shows great promise for use in high-power-electronic devices and is the superior choice compared with other widely used (or studied) ultrawide-band-gap materials such as $\beta$-Ga$_2$O$_3$.

*All experimental work referenced in Chapter 5 as part of this study was conducted by Sieun Chae.*

# CHAPTER VII

# Summary and Future Work

## 7.1 Summary

This dissertation has focused on three ultrawide-band-gap semiconductors for applications in deep-ultraviolet luminescence and high-power electronics. Density functional theory and density functional perturbation theory formed the basis for our predictive-first-principles calculations. Additional theories and methods were utilized to capture additional physics and to calculate fundamental materials properties. The results presented provide a substantial foundation for the intrinsic physics of $\beta$-Ga$_2$O$_3$, h-BN, and r-GeO$_2$. We weigh the desirable material characteristics with the downsides to each material and show that each of these semiconductors shows significant promise for the above applications. Each chapter compares our calculated results with existing theoretical and experimental data in addition to significantly expanding the available knowledge. The results contained herein advance the field of ultrawide-band-gap semiconductors in materials science and provide a basis for future experimental work which can implement these materials in electronic devices.

In Chapters II and III, we investigate the electronic, optical, and vibrational properties of $\beta$-Ga$_2$O$_3$. Chapter II focuses on the electronic and optical properties of this material. Our direction-dependent calculations for the dielectric function and optical matrix elements show that the anisotropy in the electronic and optical properties is significant, and this can explain the broad range of experimentally reported band gap values that exist in the literature. These results elucidate the band gap value as well as the near-band-edge optical properties. The significant anisotropy also emphasizes the importance of measuring properties with various polarizations to ensure the properties of low-symmetry crystal structures are fully explored. We have shown that deep-ultraviolet luminescence is possible despite $\beta$-Ga$_2$O$_3$ being an indirect-gap material. In Chapter III, we focus on the vibrational properties of $\beta$-Ga$_2$O$_3$ and determine

the specific phonon mode that limits the room-temperature mobility by closely examining the electron-phonon coupling. We also provide a non-empirical analysis and calculation of the dielectric breakdown field, finding that the value is lower than the value previously estimated using a basic model (6.0 MV/cm rather than 8.0 MV/cm).

In Chapter IV, we examine how the electronic and optical properties of h-BN depend on the basal-plane stacking sequence and number of layers (*i.e.* monolayer, bilayer, or bulk). We present the Brillouin-zone locations of the valence band maxima and conduction band minima as well as the value of fundamental band gap and its direct versus indirect character. Our resuls show that the band gap increases by $\sim 1$ eV in each step as the structure thickness decreases from bulk to bilayer to monolayer. We identified trends in the properties that affect the band gap: (1) as the energy per formula unit increases, the band gap decreases; (2) as the number of layers decreases, the band gap increases; and (3) as the number of layers decreases, the generalized phonon-assisted optical matrix element increases by a factor of $\sim 2$ (except for the unstable AA stacking). No discernible trends exist with respect to different stacking sequences for the direct versus indirect character of the fundamental band gap or the magnitude of the generalized phonon-assisted optical matrix element. A key finding from this Chapter is that all of the structures tested have transverse-electric polarized light emission, which is critical for efficient light extraction in devices. In summary, we show that changing the stacking sequence and number of layers of h-BN structures provides control over obtaining desired electronic and optical properties for deep-ultraviolet luminescence applications.

Chapters V and VI provide novel insights to r-GeO$_2$, an ultrawide-band-gap semiconductor that has been minimally investigated and unexplored for high-power electronic applications. Chapter V parallels Chapter II in that electronic and optical properties are discussed. We theoretically calculate the band gap and exciton binding energy as well as the real and imaginary parts of the dielectric function, refractive index, and absorption coefficient. We compare our calculated absorption coefficient with the previous experimental spectra and show excellent agreement along both crystallographic directions. In Chapter VI, we expand the fundamental knowledge of r-GeO$_2$ by calculating two properties for this material which, to the best of the author's knowledge, have never been calculated or measured previously. Namely, we theoretically predict the electron and hole mobilities as well as the thermal conductivity as functions of temperature. Combining the various material properties of r-GeO2, we determine the efficacy of this semiconductor for use in high-power electronics using Baliga's figure of merit (BFOM). While the electron mobility of r-GeO$_2$ is lower than

that of other competing materials, the breakdown field is larger, and BFOM goes as $E_C{}^3$ but only $\mu^1$ (BFOM $= \epsilon_0 \mu E_C{}^3/4$). We compare the properties of r-GeO$_2$ and existing materials to determine which is the most promising semiconductor for use in power devices. The BFOM for r-GeO$_2$ is significantly greater than that of competing materials, including the material $\beta$-Ga$_2$O$_3$ highlighted in Chapters II and III, showcasing the promise of r-GeO$_2$ as the superior semiconductor for high-power electronic applications.

## 7.2   Future Work

The results of this dissertation have expanded the available knowledge of ultrawide-band-gap semiconductors and have opened avenues for future work. I suggest several ideas for future computationalists and experimentalists to pursue in the hopes of furthering energy efficiency for the benefit of society:

1. Investigate the electronic, optical, and vibrational properties of the other polymorphs of Ga$_2$O$_3$ to determine the efficacy of the other crystal structures for deep-ultraviolet or high-power electronic applications.

2. Design, develop, and experimentally implement light-emitting devices with various controlled stacking sequences of h-BN.

3. Explore the charge carrier mobilities and dielectric breakdown fields of c-BN and w-BN (which may exceed those of h-BN) for applications in high-power electronics.

4. Thoroughly analyze the electronic and vibrational properties of other rutile metal dioxides (*e.g.* r-SnO$_2$ and r-SiO$_2$) for applications in high-power electronics.

5. Develop a rigorous yet computationally reasonable first-principles method for predicting the dielectric breakdown field of any material.

# BIBLIOGRAPHY

# BIBLIOGRAPHY

[1] H. Hayashi, "The materials of our dreams, compound semiconductors," 2012. [Online]. Available: https://global-sei.com/sn/2012/417/3a.html

[2] E. I. Lipatov, E. A. Sosnin, and S. M. Avdeev, "The inactivation of helminth eggs with the narrow-bandwidth radiation of excimer lamps," *Russian Journal of Parasitology*, vol. 35, no. 1, pp. 107–113, 2016.

[3] S. Nakamura, "Nobel Lecture: Background Story of the Invention of Efficient Blue InGaN Light Emitting Diodes," University of California, Santa Barbara, Santa Barbara, Tech. Rep., 2014. [Online]. Available: https://www.nobelprize.org/uploads/2018/06/nakamura-lecture.pdf

[4] U.S. Energy Information Administration, "How electricity is delivered to consumers," 2019. [Online]. Available: https://www.eia.gov/energyexplained/electricity/delivery-to-consumers.php

[5] Z. Guo, A. Verma, X. Wu, F. Sun, A. Hickman, T. Masui, A. Kuramata, M. Higashiwaki, D. Jena, and T. Luo, "Anisotropic thermal conductivity in single crystal $\beta$-gallium oxide," *Applied Physics Letters*, vol. 106, p. 111909, 2015.

[6] A. A. Bolzan, C. Fong, B. J. Kennedy, and C. J. Howard, "Structural Studies of Rutile-Type Metal Dioxides," *Acta Cryst.*, vol. B53, pp. 373–380, 1997.

[7] M. Stapelbroek and B. D. Evans, "Exciton structure in the U.V.-absorption edge of tetragonal $GeO_2$," *Solid State Communications*, vol. 25, no. 11, pp. 959–962, 1978.

[8] J. Åhman, G. Svensson, and J. Albertsson, "A reinvestigation of $\beta$-gallium oxide," *Acta Crystallographica Section C: Crystal Structure Communications*, vol. 52, no. 6, pp. 1336–1338, 1996.

[9] B. Liu, M. Gu, and X. Liu, "Lattice dynamical, dielectric, and thermodynamic properties of $\beta$-$Ga_2O_3$ from first principles," *Applied Physics Letters*, vol. 91, p. 172102, 2007.

[10] M. Schubert, R. Korlacki, S. Knight, T. Hofmann, S. Schöche, V. Darakchieva, E. Janzén, B. Monemar, D. Gogova, Q.-T. Thieu, R. Togashi, H. Murakami, Y. Kumagai, K. Goto, A. Kuramata, S. Yamakoshi, and M. Higashiwaki, "Anisotropy, phonon modes, and free charge carrier parameters in monoclinic

$\beta$-gallium oxide single crystals," *Physical Review B*, vol. 93, no. 12, p. 125209, 2016.

[11] T. Onuma, S. Saito, K. Sasaki, K. Goto, T. Masui, T. Yamaguchi, T. Honda, A. Kuramata, and M. Higashiwaki, "Temperature-dependent exciton resonance energies and their correlation with IR-active optical phonon modes in $\beta$-$Ga_2O_3$ single crystals," *Applied Physics Letters*, vol. 108, no. 10, p. 101904, 2016. [Online]. Available: http://dx.doi.org/10.1063/1.4943175

[12] D. Machon, P. F. McMillan, B. Xu, and J. Dong, "High-pressure study of the $\beta$-to-$\alpha$ transition in $Ga_2O_3$," *Physical Review B*, vol. 73, p. 094125, 2006.

[13] A. Samanta, M. Jain, and A. K. Singh, "Ultra-sensitive pressure dependence of bandgap of rutile-$GeO_2$ revealed by many body perturbation theory," *Journal of Chemical Physics*, vol. 143, no. 6, p. 064703(6), 2015.

[14] R. Kaindl, D. M. Többens, S. Penner, T. Bielz, S. Soisuwan, and B. Klötzer, "Quantum mechanical calculations of the vibrational spectra of quartz- and rutile-type GeO2," *Physics and Chemistry of Minerals*, vol. 39, no. 1, pp. 47–55, 2012.

[15] A. Kahan, J. W. Goodrum, R. S. Singh, and S. S. Mitra, "Polarized reflectivity spectra of tetragonal $GeO_2$," *Journal of Applied Physics*, vol. 42, no. 11, pp. 4444–4446, 1971.

[16] A. Sanson, G. S. Pokrovski, M. Giarola, and G. Mariotto, "Vibrational dynamics of rutile-type $GeO_2$ from micro-Raman spectroscopy experiments and first-principles calculations," *EPL*, vol. 109, no. 2, 2015.

[17] J. F. Scott, "Raman spectra of $GeO_2$," *Physical Review B*, vol. 1, no. 8, pp. 3488–3493, 1970.

[18] J. Bardeen and W. Brattain, "Three-Electrode Circuit Element Utilizing Semiconductive Materials," United States Patent 2524035, Oct. 3, 1950.

[19] J. Y. Tsao, S. Chowdhury, M. A. Hollis, D. Jena, N. M. Johnson, K. A. Jones, R. J. Kaplar, S. Rajan, C. G. Van de Walle, E. Bellotti, C. L. Chua, R. Collazo, M. E. Coltrin, J. A. Cooper, K. R. Evans, S. Graham, T. A. Grotjohn, E. R. Heller, M. Higashiwaki, M. S. Islam, P. W. Juodawlkis, M. A. Khan, A. D. Koehler, J. H. Leach, U. K. Mishra, R. J. Nemanich, R. C. Pilawa-Podgurski, J. B. Shealy, Z. Sitar, M. J. Tadjer, A. F. Witulski, M. Wraback, and J. A. Simmons, "Ultrawide-Bandgap Semiconductors: Research Opportunities and Challenges," *Advanced Electronic Materials*, vol. 4, no. 1, pp. 1–49, 2018.

[20] S. Fujita, "Wide-bandgap semiconductor materials: For their full bloom," *Japanese Journal of Applied Physics*, vol. 54, p. 030101, 2015.

[21] M. Liao, Y. Koide, and L. Sang, "Nanostructured Wide-bandgap Semiconductors for Ultraviolet Detection," *Austin Journal of Nanomedicine & Nanotechnology*, vol. 2, no. 5, p. 1029, 2014. [Online]. Available: http://www.austinpublishinggroup.com/nanomedicine-nanotechnology/fulltext/ajnn-v2-id1029.pdf

[22] W. Tian, H. Lu, and L. Li, "Nanoscale ultraviolet photodetectors based on onedimensional metal oxide nanostructures," *Nano Research*, vol. 8, no. 2, pp. 382–405, 2015.

[23] M. Higashiwaki, K. Sasaki, A. Kuramata, T. Masui, and S. Yamakoshi, "Development of gallium oxide power devices," *Physica Status Solidi A*, vol. 211, no. 1, pp. 21–26, 2014.

[24] C. Kittel, *Introduction to Solid State Physics*, 8th ed. John Wiley & Sons, 2005.

[25] B. K. Ridley, *Quantum Processes in Semiconductors*, 5th ed. New York: Oxford University Press, 2013.

[26] American Cancer Society, "Ultraviolet (UV) Radiation," 2019. [Online]. Available: https://www.cancer.org/content/cancer/en/cancer/cancer-causes/radiation-exposure/uv-radiation.html

[27] J.-Y. Shin, S.-J. Kim, D.-K. Kim, and D.-H. Kang, "Fundamental Characteristics of Deep-UV Light-Emitting Diodes and Their Application to Control Foodborne Pathogens," *Applied and Environmental Microbiology*, vol. 82, no. 1, pp. 2–10, 2016.

[28] Centers for Disease Control and Prevention, "Burden of Foodborne Illness: Findings," 2018. [Online]. Available: https://www.cdc.gov/foodborneburden/2011-foodborne-estimates.html

[29] S. Nakamura, T. Mukai, and M. Senoh, "Candela-class high-brightness InGaN/AlGaN double-heterostructure blue-light-emitting diodes," *Applied Physics Letters*, vol. 64, no. 13, pp. 1687–1689, 1994.

[30] H. Amano, K. Hiramatsu, M. Kito, N. Sawaki, and I. Akasaki, "Zn related electroluminescent properties in MOVPE grown GaN," *Journal of Crystal Growth*, vol. 93, no. 1-4, pp. 79–82, 1988.

[31] M. A. Würtele, T. Kolbe, M. Lipsz, A. Külberg, M. Weyers, M. Kneissl, and M. Jekel, "Application of GaN-based ultraviolet-C light emitting diodes — UV LEDs — for water disinfection," *Water Research*, vol. 45, no. 3, pp. 1481–1489, 2011.

[32] K. Oguma, R. Kita, H. Sakai, M. Murakami, and S. Takizawa, "Application of UV light emitting diodes to batch and flow-through water disinfection

systems," *Desalination*, vol. 328, pp. 24–30, 2013. [Online]. Available: http://dx.doi.org/10.1016/j.desal.2013.08.014

[33] Y. Zhang, Y. Zheng, R. Meng, C. Sun, K. Tian, C. Geng, Z. H. Zhang, G. Liu, and W. Bi, "Enhancing Both TM- and TE-Polarized Light Extraction Efficiency of AlGaN-Based Deep Ultraviolet Light-Emitting Diode via Air Cavity Extractor with Vertical Sidewall," *IEEE Photonics Journal*, vol. 10, no. 4, pp. 1–9, 2018.

[34] H. Peelaers and C. G. Van de Walle, "Sub-band-gap absorption in $\beta$-Ga$_2$O$_3$," *Applied Physics Letters*, vol. 111, no. 18, p. 182104(5), 2017.

[35] D. A. Laleyan, K. Mengle, S. Zhao, Y. Wang, E. Kioupakis, and Z. Mi, "Effect of growth temperature on the structural and optical properties of few-layer hexagonal boron nitride by molecular beam epitaxy," *Opt. Express*, vol. 26, no. 18, pp. 23 031–23 039, 2018. [Online]. Available: http://www.opticsexpress.org/abstract.cfm?URI=oe-26-18-23031

[36] J. E. Northrup, C. L. Chua, Z. Yang, T. Wunderer, M. Kneissl, N. M. Johnson, and T. Kolbe, "Effect of strain and barrier composition on the polarization of light emission from AlGaN/AlN quantum wells," *Applied Physics Letters*, vol. 100, no. 2, pp. 1–5, 2012.

[37] E. F. Pecora, W. Zhang, J. Yin, R. Paiella, L. D. Negro, and T. D. Moustakas, "Polarization properties of deep-ultraviolet optical gain in Al-rich algan structures," *Applied Physics Express*, vol. 5, no. 3, pp. 5–7, 2012.

[38] D. Bayerl and E. Kioupakis, "Visible-wavelength polarized-light emission with small-diameter InN nanowires," *Nano Letters*, vol. 14, no. 7, pp. 3709–3714, 2014.

[39] N. Sanders, D. Bayerl, G. Shi, K. A. Mengle, and E. Kioupakis, "Electronic and Optical Properties of Two-Dimensional GaN from First-Principles," *Nano Letters*, vol. 17, no. 12, pp. 7345–7349, 2017.

[40] D. Bayerl, S. Islam, C. M. Jones, V. Protasenko, D. Jena, and E. Kioupakis, "Deep ultraviolet emission from ultra-thin GaN/AlN heterostructures," *Applied Physics Letters*, vol. 109, no. 24, 2016.

[41] U.S. Energy Information Administration, "How much electricity is lost in electricity transmission and distribution in the United States?" 2019. [Online]. Available: https://www.eia.gov/tools/faqs/faq.php?id=105{&}t=3

[42] S. Gerrity and A. Lantero, "Understanding the Grid," 2014. [Online]. Available: https://www.energy.gov/articles/infographic-understanding-grid

[43] Union of Concerned Scientists, "How the Electricity Grid Works," 2015. [Online]. Available: https://www.ucsusa.org/resources/how-electricity-grid-works

[44] B. J. Baliga, "Semiconductors for high-voltage, vertical channel field-effect transistors," *Journal of Applied Physics*, vol. 53, no. 3, pp. 1759–1764, 1982.

[45] ——, "Power Semiconductor Device Figure of Merit for High-Frequency Applications," *IEEE Electron Device Letters*, vol. 10, no. 10, pp. 455–457, 1989.

[46] Y. Sun, S. A. Boggs, and R. Ramprasad, "The intrinsic electrical breakdown strength of insulators from first principles," *Applied Physics Letters*, vol. 101, p. 132906, 2012.

[47] P. Hohenberg and W. Kohn, "Inhomogeneous electron gas," *Physical Review*, vol. 136, no. 3B, pp. B864–B871, 1964.

[48] L. Hedin, "New Method for Calculating the One-Particle Green's Function with Application to the Electron-Gas Problem," *Physical Review*, vol. 139, no. 3A, pp. A796–A823, 1965.

[49] X. Gonze and C. Lee, "Dynamical matrices, Born effective charges, dielectric permittivity tensors, and interatomic force constants from density-functional perturbation theory," *Physical Review B - Condensed Matter and Materials Physics*, vol. 55, no. 16, pp. 10 355–10 368, 1997.

[50] P. Giannozzi, S. De Gironcoli, P. Pavone, and S. Baroni, "Ab initio calculation of phonon dispersions in semiconductors," *Physical Review B*, vol. 43, no. 9, pp. 7231–7242, 1991.

[51] N. Marzari and D. Vanderbilt, "Maximally localized generalized Wannier functions for composite energy bands," *Physical Review B - Condensed Matter and Materials Physics*, vol. 56, no. 20, pp. 12 847–12 865, 1997.

[52] M. Higashiwaki, K. Sasaki, A. Kuramata, T. Masui, and S. Yamakoshi, "Gallium oxide ($Ga_2O_3$) metal-semiconductor field-effect transistors on single-crystal $\beta$-$Ga_2O_3$ (010) substrates," *Applied Physics Letters*, vol. 100, no. 1, pp. 20–23, 2012.

[53] M. Higashiwaki, K. Sasaki, T. Kamimura, M. Hoi Wong, D. Krishnamurthy, A. Kuramata, T. Masui, and S. Yamakoshi, "Depletion-mode $Ga_2O_3$ metal-oxide-semiconductor field-effect transistors on $\beta$-$Ga_2O_3$ (010) substrates and temperature dependence of their device characteristics," *Applied Physics Letters*, vol. 103, no. 12, p. 123511, 2013. [Online]. Available: http://aip.scitation.org/doi/10.1063/1.4821858

[54] W. S. Hwang, A. Verma, H. Peelaers, V. Protasenko, S. Rouvimov, H. G. Xing, A. Seabaugh, W. Haensch, C. V. de Walle, Z. Galazka, M. Albrecht, R. Fornari, and D. Jena, "High-voltage field effect transistors with wide-bandgap $\beta$-$Ga_2O_3$ nanomembranes," *Applied Physics Letters*, vol. 104, no. 20, p. 203111, 2014. [Online]. Available: http://aip.scitation.org/doi/10.1063/1.4879800

[55] K. Sasaki, M. Higashiwaki, A. Kuramata, T. Masui, and S. Yamakoshi, "MBE grown $Ga_2O_3$ and its power device applications," *Journal of Crystal Growth*, vol. 378, pp. 591–595, 2013. [Online]. Available: http://dx.doi.org/10.1016/j.jcrysgro.2013.02.015

[56] P. Feng, J. Y. Zhang, Q. H. Li, and T. H. Wang, "Individual $\beta$-$Ga_2O_3$ nanowires as solar-blind photodetectors," *Applied Physics Letters*, vol. 88, no. 15, p. 153107(3), 2006. [Online]. Available: http://aip.scitation.org/doi/10.1063/1.2193463

[57] L. Li, E. Auer, M. Liao, X. Fang, T. Zhai, U. K. Gautam, A. Lugstein, Y. Koide, Y. Bando, and D. Golberg, "Deep-ultraviolet solar-blind photoconductivity of individual gallium oxide nanobelts," *Nanoscale*, vol. 3, pp. 1120–1126, 2011. [Online]. Available: http://xlink.rsc.org/?DOI=c0nr00702a

[58] T. Onuma, S. Saito, K. Sasaki, T. Masui, T. Yamaguchi, T. Honda, and M. Higashiwaki, "Valence band ordering in $\beta$-$Ga_2O_3$ studied by polarized transmittance and reflectance spectroscopy," *Jpn. J. Appl. Phys*, vol. 54, p. 112601, 2015.

[59] S. Ghose, M. S. Rahman, J. S. Rojas-Ramirez, M. Caro, R. Droopad, A. Arias, and N. Nedev, "Structural and optical properties of $\beta$-$Ga_2O_3$ thin films grown by plasma-assisted molecular beam epitaxy," *Journal of Vacuum Science & Technology B, Nanotechnology and Microelectronics: Materials, Processing, Measurement, and Phenomena*, vol. 34, no. 2, p. 02L109, 2016. [Online]. Available: http://avs.scitation.org/doi/10.1116/1.4942045

[60] Y. Li, T. Tokizono, M. Liao, M. Zhong, Y. Koide, I. Yamada, and J. J. Delaunay, "Efficient assembly of bridged $\beta$-$Ga_2O_3$ nanowires for solar-blind photodetection," *Advanced Functional Materials*, vol. 20, no. 22, pp. 3972–3978, 2010.

[61] T. Onuma, S. Fujioka, T. Yamaguchi, M. Higashiwaki, K. Sasaki, T. Masui, and T. Honda, "Correlation between blue luminescence intensity and resistivity in $\beta$-$Ga_2O_3$ single crystals," *Applied Physics Letters*, vol. 103, no. 4, pp. 2011–2014, 2013.

[62] P. Giannozzi, S. Baroni, N. Bonini, M. Calandra, R. Car, C. Cavazzoni, D. Ceresoli, G. L. Chiarotti, M. Cococcioni, I. Dabo, A. Dal Corso, S. De Gironcoli, S. Fabris, G. Fratesi, R. Gebauer, U. Gerstmann, C. Gougoussis, A. Kokalj, M. Lazzeri, L. Martin-Samos, N. Marzari, F. Mauri, R. Mazzarello, S. Paolini, A. Pasquarello, L. Paulatto, C. Sbraccia, S. Scandolo, G. Sclauzero, A. P. Seitsonen, A. Smogunov, P. Umari, and R. M. Wentzcovitch, "QUANTUM ESPRESSO: A modular and open-source software project for quantum simulations of materials," *Journal of Physics: Condensed Matter*, vol. 21, no. 39, p. 395502(10), 2009.

[63] J. Deslippe, G. Samsonidze, D. A. Strubbe, M. Jain, M. L. Cohen, and S. G. Louie, "BerkeleyGW: A massively parallel computer package for the calculation

of the quasiparticle and optical properties of materials and nanostructures," *Computer Physics Communications*, vol. 183, no. 6, pp. 1269–1289, 2012.

[64] M. S. Hybertsen and S. G. Louie, "Electron correlation in semiconductors and insulators: Band gaps and quasiparticle energies," *Phys. Rev. B*, vol. 34, no. 8, pp. 5390–5413, 1986.

[65] N. Marzari, A. A. Mostofi, J. R. Yates, I. Souza, and D. Vanderbilt, "Maximally localized Wannier functions: Theory and applications," *Reviews of Modern Physics*, vol. 84, no. 4, pp. 1419–1475, 2012.

[66] A. A. Mostofi, J. R. Yates, Y. S. Lee, I. Souza, D. Vanderbilt, and N. Marzari, "wannier90: A tool for obtaining maximally-localised Wannier functions," *Computer Physics Communications*, vol. 178, no. 9, pp. 685–699, 2008.

[67] E. Kioupakis, Q. Yan, D. Steiauf, and C. G. Van de Walle, "Temperature and carrier-density dependence of Auger and radiative recombination in nitride optoelectronic devices," *New Journal of Physics*, vol. 15, p. 125006(14), 2013.

[68] N. Troullier and J. L. Martins, "Efficient pseudopotentials for plane-wave calculations. II. Operators for fast iterative diagonalization," *Physical Review B*, vol. 43, no. 11, pp. 8861–8869, 1991.

[69] M. L. Tiago, S. Ismail-Beigi, and S. G. Louie, "Effect of semicore orbitals on the electronic band gaps of Si, Ge, and GaAs within the GW approximation," *Physical Review B - Condensed Matter and Materials Physics*, vol. 69, no. 12, pp. 1–5, 2004.

[70] J. Deslippe, G. Samsonidze, M. Jain, M. L. Cohen, and S. G. Louie, "Coulomb-hole summations and energies for GW calculations with limited number of empty orbitals: A modified static remainder approach," *Physical Review B*, vol. 87, no. 16, p. 165124(6), 2013.

[71] B. C. Shih, Y. Xue, P. Zhang, M. L. Cohen, and S. G. Louie, "Quasiparticle band gap of ZnO: High accuracy from the conventional G0W0 approach," *Physical Review Letters*, vol. 105, no. 14, pp. 1–4, 2010.

[72] W. Setyawan and S. Curtarolo, "High-throughput electronic band structure calculations: Challenges and tools," *Computational Materials Science*, vol. 49, no. 2, pp. 299–312, 2010. [Online]. Available: http://dx.doi.org/10.1016/j.commatsci.2010.05.010

[73] J. Furthmüller and F. Bechstedt, "Quasiparticle bands and spectra of $Ga_2O_3$ polymorphs," *Physical Review B*, vol. 93, no. 11, p. 115204, 2016. [Online]. Available: https://link.aps.org/doi/10.1103/PhysRevB.93.115204

[74] H. Peelaers and C. G. Van de Walle, "Brillouin zone and band structure of $\beta$-$Ga_2O_3$," *Physica Status Solidi B*, vol. 252, no. 4, pp. 828–832, 2015.

[75] C. Janowitz, V. Scherer, M. Mohamed, A. Krapf, H. Dwelk, R. Manzke, Z. Galazka, R. Uecker, K. Irmscher, R. Fornari, M. Michling, D. Schmeißer, J. R. Weber, J. B. Varley, and C. G. V. de Walle, "Experimental electronic structure of $In_2O_3$ and $Ga_2O_3$," *New Journal of Physics*, vol. 13, no. 8, p. 085014, 2011. [Online]. Available: http://stacks.iop.org/1367-2630/13/i=8/a=085014?key=crossref.724f2b675d24d0496f7f5bcd57f75f54

[76] Y. Xu and M. A. A. Schoonen, "The Absolute Energy Positions of Conduction and Valence Bands of Selected Semiconducting Minerals," *American Mineralogist*, vol. 85, no. 3-4, pp. 543–556, 2000. [Online]. Available: http://ammin.geoscienceworld.org/content/85/3-4/543{%}0Ahttp://ammin.geoscienceworld.org/content/85/3-4/543.full.pdf{%}0Ahttp://ammin.geoscienceworld.org/content/85/3-4/543.full.pdf+html?frame=sidebar

[77] M. Mohamed, K. Irmscher, C. Janowitz, Z. Galazka, R. Manzke, and R. Fornari, "Schottky barrier height of Au on the transparent semiconducting oxide $\beta$-$Ga_2O_3$," *Applied Physics Letters*, vol. 101, no. 13, pp. 3–8, 2012.

[78] K. A. Mengle, G. Shi, D. Bayerl, and E. Kioupakis, "First-principles calculations of the near-edge optical properties of $\beta$-$Ga_2O_3$," *Applied Physics Letters*, vol. 212104, pp. 2–6, 2016.

[79] H. Tippins, "Optical Absorption and Photoconductivity in the Band Edge of Beta-Ga2O3," *Physical Review*, vol. 140, no. 1A, pp. A316–A319, 1965. [Online]. Available: http://link.aps.org/doi/10.1103/PhysRev.140.A316

[80] T. Matsumoto, M. Aoki, A. Kinoshita, and T. Aono, "Absorption and reflection of vapor grown single crystal platelets of $\beta$-$Ga_2O_3$," *Japanese Journal of Applied Physics*, vol. 13, no. 10, pp. 1578–1582, 1974.

[81] N. Ueda, H. Hosono, R. Waseda, and H. Kawazoe, "Anisotropy of electrical and optical properties in $\beta$-$Ga_2O_3$ single crystals," *Applied Physics Letters*, vol. 71, no. 7, pp. 933–935, 1997. [Online]. Available: http://aip.scitation.org/doi/10.1063/1.119693

[82] F. Ricci, F. Boschi, A. Baraldi, A. Filippetti, M. Higashiwaki, A. Kuramata, V. Fiorentini, and R. Fornari, "Theoretical and experimental investigation of optical absorption anisotropy in $\beta$-$Ga_2O_3$," *Journal of Physics: Condensed Matter*, vol. 28, p. 224005, 2016. [Online]. Available: http://arxiv.org/abs/1511.02601

[83] C. Sturm, J. Furthmüller, F. Bechstedt, R. Schmidt-Grund, and M. Grundmann, "Dielectric tensor of monoclinic $Ga_2O_3$ single crystals in the spectral range 0.5-8.5 eV," *APL Materials*, vol. 3, no. 10, pp. 0–9, 2015. [Online]. Available: http://arxiv.org/abs/1507.05401{%}0Ahttp://dx.doi.org/10.1063/1.4934705

[84] A. McAllister, D. Bayerl, and E. Kioupakis, "Radiative and Auger recombination processes in indium nitride," *Applied Physics Letters*, vol. 112, p. 251108, 2018. [Online]. Available: http://dx.doi.org/10.1063/1.5038106

[85] J. B. Varley, A. Janotti, C. Franchini, and C. G. Van de Walle, "Role of self-trapping in luminescence and p-type conductivity of wide-band-gap oxides," *Physical Review B*, vol. 85, no. 8, p. 081109(4), 2012.

[86] S. Fratini and P. Quemerais, "Polaron crystallization and melting: Effects of the long-range Coulomb forces," *Modern Physics Letters B*, vol. 12, no. 24, pp. 1003–1012, 1998.

[87] B. Hoeneisen, C. A. Mead, and M.-A. Nicolet, "Permittivity of $\beta$-Ga$_2$O$_3$ at low frequencies," *Solid State Electronics*, vol. 14, pp. 1057–1059, 1971.

[88] M. Higashiwaki and G. H. Jessen, "Guest Editorial: The dawn of gallium oxide microelectronics," *Applied Physics Letters*, vol. 112, no. 6, p. 060401(4), 2018.

[89] S. I. Stepanov, V. I. Nikolaev, V. E. Bougrov, and A. E. Romanov, "Gallium Oxide: Properties and Applications- A Review," *Rev. Adv. Mater. Sci.*, vol. 44, pp. 63–86, 2016.

[90] K. Sasaki, D. Wakimoto, Q. T. Thieu, Y. Koishikawa, A. Kuramata, M. Higashiwaki, and S. Yamakoshi, "First Demonstration of Ga$_2$O$_3$ Trench MOS-Type Schottky Barrier Diodes," *IEEE Electron Device Letters*, vol. 38, no. 6, pp. 783–785, 2017. [Online]. Available: http://linkinghub.elsevier.com/retrieve/pii/S1359645417307279

[91] N. Ma, N. Tanen, A. Verma, Z. Guo, T. Luo, H. G. Xing, and D. Jena, "Intrinsic electron mobility limits in $\beta$-Ga$_2$O$_3$," *Applied Physics Letters*, vol. 109, no. 21, p. 212101(5), 2016.

[92] K. Ghosh and U. Singisetti, "*Ab initio* calculation of electron–phonon coupling in monoclinic $\beta$-Ga$_2$O$_3$ crystal," *Applied Physics Letters*, vol. 109, no. 7, p. 072102, 2016. [Online]. Available: http://aip.scitation.org/doi/10.1063/1.4961308

[93] Y. Kang, K. Krishnaswamy, H. Peelaers, and C. G. Van de Walle, "Fundamental limits on the electron mobility of $\beta$-Ga$_2$O$_3$," *Journal of Physics: Condensed Matter*, vol. 29, no. 23, p. 234001, 2017. [Online]. Available: http://stacks.iop.org/0953-8984/29/i=23/a=234001?key=crossref.516282c8fc64ac071e84ed149f885284

[94] J. Carrete, B. Vermeersch, A. Katre, A. van Roekeghem, T. Wang, G. K. Madsen, and N. Mingo, "almaBTE : A solver of the space–time dependent Boltzmann transport equation for phonons in structured materials," *Computer Physics Communications*, vol. 220C, pp. 351–362, 2017.

[95] S. Baroni, S. De Gironcoli, A. Dal Corso, and P. Giannozzi, "Phonons and related crystal properties from density functional perturbation theory," *Rev. Mod. Phys.*, vol. 73, pp. 515–562, 2001. [Online]. Available: http://dx.doi.org/10.1103/RevModPhys.73.515

[96] E. Kioupakis, P. Rinke, A. Schleife, F. Bechstedt, and C. G. Van De Walle, "Free-carrier absorption in nitrides from first principles," *Physical Review B - Condensed Matter and Materials Physics*, vol. 81, no. 24, p. 241201, 2010.

[97] J. P. Perdew, K. Burke, and M. Ernzerhof, "Generalized gradient approximation made simple," *Physical Review Letters*, vol. 77, no. 18, pp. 3865–3868, 1996.

[98] X. Gonze, F. Jollet, F. Abreu Araujo, D. Adams, B. Amadon, T. Applencourt, C. Audouze, J.-M. Beuken, J. Bieder, A. Bokhanchuk, E. Bousquet, F. Bruneval, D. Caliste, M. Cote, F. Dahm, F. Da Pieve, M. Delaveau, M. Di Gennaro, B. Dorado, C. Espejo, G. Geneste, L. Genovese, A. Gerossier, M. Giantomassi, Y. Gillet, D. R. Hamann, L. He, G. Jomard, J. Laflamme Janssen, S. Le Roux, A. Levitt, A. Lherbier, F. Liu, I. Lukacevic, A. Martin, C. Martins, M. J. T. Oliveira, S. Ponce, Y. Pouillon, T. Rangel, G.-M. Rignanese, A. H. Romero, B. Rousseau, O. Rubel, A. A. Shukri, M. Stankovski, M. Torrent, M. J. Van Setten, B. Van Troeye, M. J. Verstraete, D. Waroquier, J. Wiktor, B. Xu, A. Zhou, and J. W. Zwanziger, "Recent developments in the ABINIT software package," *Computer Physics Communications*, vol. 205, pp. 106–131, 2016.

[99] G. Kresse and J. Hafner, "*Ab initio* molecular dynamics for liquid metals," *Physical Review B*, vol. 47, no. 1, pp. 558–561, 1993.

[100] G. Kresse and J. Furthmüller, "Efficiency of *ab-initio* total energy calculations for metals and semiconductors using a plane-wave basis set," *Computational Materials Science*, vol. 6, no. 1, pp. 15–50, 1996.

[101] T. Onuma, S. Fujioka, T. Yamaguchi, Y. Itoh, M. Higashiwaki, K. Sasaki, T. Masui, and T. Honda, "Polarized Raman spectra in $\beta$-$Ga_2O_3$ single crystals," *Journal of Crystal Growth*, vol. 401, pp. 330–333, 2014. [Online]. Available: http://linkinghub.elsevier.com/retrieve/pii/S0022024814000475

[102] J. B. Khurgin, D. Jena, and Y. J. Ding, "Isotope disorder of phonons in GaN and its beneficial effect on high power field effect transistors," *Applied Physics Letters*, vol. 93, p. 032110, 2008.

[103] K. Sarasamak, S. Limpijumnong, and W. R. Lambrecht, "Pressure-dependent elastic constants and sound velocities of wurtzite SiC, GaN, InN, ZnO, and CdSe, and their relation to the high-pressure phase transition: A first-principles study," *Physical Review B*, vol. 82, p. 035201, 2010.

[104] X. L. Chen, J. K. Liang, Y. P. Xu, T. Xu, P. Z. Jiang, Y. D. Yu, and K. Q. Lu, "Structure and Debye temperature of wurtzite GaN," *Modern Physics Letters B*, vol. 13, no. 9-10, pp. 285–290, 1999.

[105] F. D. Murnaghan, *Finite Deformations of an Elastic Solid.* New York: Dover, 1967.

[106] L. Vočadlo, J. P. Poirer, and G. D. Price, "Grüneisen parameters and isothermal equations of state," *American Mineralogist*, vol. 85, no. 2, pp. 390–395, 2000.

[107] V. Y. Vaschenko and V. N. Zubarev, "Concerning the Grüneisen constant," *Sov. Phys. Solid State*, vol. 5, p. 653, 1963.

[108] A. R. Goñi, H. Siegle, K. Syassen, C. Thomsen, and J.-M. Wagner, "Effect of pressure on optical phonon modes and transverse effective charges in GaN and AlN," *Physical Review B*, vol. 64, no. 3, p. 035205, 2001. [Online]. Available: https://link.aps.org/doi/10.1103/PhysRevB.64.035205

[109] M. Higashiwaki, K. Sasaki, H. Murakami, Y. Kumagai, A. Koukitu, A. Kuramata, T. Masui, and S. Yamakoshi, "Recent progress in $Ga_2O_3$ power devices," *Semiconductor Science and Technology*, vol. 31, no. 3, p. 034001, 2016. [Online]. Available: http://stacks.iop.org/0268-1242/31/i=3/a=034001?key=crossref.69c77612f652ba66218063819530aaa0

[110] H. Peelaers, E. Kioupakis, and C. G. Van de Walle, "Free-carrier absorption in transparent conducting oxides: Phonon and impurity scattering in $SnO_2$," *Physical Review B*, vol. 92, p. 235201(9), 2015.

[111] K. Ghosh and U. Singisetti, "Impact ionization in $\beta$-$Ga_2O_3$," *Journal of Applied Physics*, vol. 124, no. 8, p. 085707, 2018. [Online]. Available: http://aip.scitation.org/doi/10.1063/1.5034120

[112] Q. Yan, E. Kioupakis, D. Jena, and C. G. Van de Walle, "First-principles study of high-field-related electronic behavior of group-III nitrides," *Physical Review B*, vol. 90, no. 12, p. 121201(R), 2014.

[113] J. L. Hudgins, G. S. Simin, E. Santi, and M. A. Khan, "An assessment of wide bandgap semiconductors for power devices," *IEEE Transactions on Power Electronics*, vol. 18, no. 3, pp. 907–914, 2003.

[114] Z. Galazka, K. Irmscher, R. Uecker, R. Bertram, M. Pietsch, A. Kwasniewski, M. Naumann, T. Schulz, R. Schewski, D. Klimm, and M. Bickermann, "On the bulk $\beta$-$Ga_2O_3$ single crystals grown by the Czochralski method," *Journal of Crystal Growth*, vol. 404, pp. 184–191, 2014. [Online]. Available: http://dx.doi.org/10.1016/j.jcrysgro.2014.07.021{%}5Cnhttp://linkinghub.elsevier.com/retrieve/pii/S0022024814005193

[115] A. Parisini and R. Fornari, "Analysis of the scattering mechanisms controlling the electron mobility in $\beta$-$Ga_2O_3$ crystals," *Semiconductor Science and Technology*, vol. 31, p. 035023, 2016. [Online]. Available: http://dx.doi.org/10.1088/0268-1242/31/3/035023

[116] L. Williams and E. Kioupakis, "BInGaN alloys nearly lattice-matched to GaN for high-power high-efficiency visible LEDs," *Applied Physics Letters*, vol. 111, p. 211107, 2017. [Online]. Available: http://dx.doi.org/10.1063/1.4997601

[117] F. Zhang, K. Saito, T. Tanaka, M. Nishio, M. Arita, and Q. Guo, "Wide bandgap engineering of $(AlGa)_2O_3$ films," *Applied Physics Letters*, vol. 105, p. 162107, 2014. [Online]. Available: http://aip.scitation.org/doi/10.1063/1.4900522

[118] K. Watanabe, T. Taniguchi, and H. Kanda, "Direct-bandgap properties and evidence for ultraviolet lasing of hexagonal boron nitride single crystal," *Nature Materials*, vol. 3, no. 6, pp. 404–409, 2004.

[119] G. Cassabois, P. Valvin, and B. Gil, "Hexagonal boron nitride is an indirect bandgap semiconductor," *Nature Photonics*, vol. 10, no. 4, pp. 262–266, 2016. [Online]. Available: http://dx.doi.org/10.1038/nphoton.2015.277

[120] L. Sponza, H. Amara, C. Attaccalite, S. Latil, T. Galvani, F. Paleari, L. Wirtz, and F. Ducastelle, "Direct and indirect excitons in boron nitride polymorphs: A story of atomic configuration and electronic correlation," *Physical Review B*, vol. 98, no. 12, p. 125206(17), 2018. [Online]. Available: http://arxiv.org/abs/1806.06201

[121] R. Bourrellier, M. Amato, L. H. Galvão Tizei, C. Giorgetti, A. Gloter, M. I. Heggie, K. March, O. Stéphan, L. Reining, M. Kociak, and A. Zobelli, "Nanometric Resolved Luminescence in h-BN Flakes: Excitons and Stacking Order," *ACS Photonics*, vol. 1, no. 9, pp. 857–862, 2014.

[122] C.-J. J. Kim, L. Brown, M. W. Graham, R. Hovden, R. W. Havener, P. L. McEuen, D. A. Muller, and J. Park, "Stacking order dependent second harmonic generation and topological defects in h-BN bilayers," *Nano Letters*, vol. 13, no. 11, pp. 5660–5665, 2013.

[123] J. H. Warner, M. H. Rümmeli, A. Bachmatiuk, and B. Büchner, "Atomic Resolution Imaging and Topogarphy of Boron Nitride Sheet Produced by Chemical Exfoliation," *ACS Nano*, vol. 4, no. 3, pp. 1299–1304, 2010.

[124] Y. Fujimoto and S. Saito, "Band engineering and relative stabilities of hexagonal boron nitride bilayers under biaxial strain," *Physical Review B*, vol. 94, no. 24, p. 245427(8), 2016.

[125] G. Constantinescu, A. Kuc, and T. Heine, "Stacking in bulk and bilayer hexagonal boron nitride," *Physical Review Letters*, vol. 111, no. 3, p. 036104(5), 2013.

[126] D. Wickramaratne, L. Weston, and C. G. Van De Walle, "Monolayer to Bulk Properties of Hexagonal Boron Nitride," *Journal of Physical Chemistry C*, vol. 122, no. 44, pp. 25 524–25 529, 2018.

[127] E. Cannuccia, B. Monserrat, and C. Attaccalite, "Theory of phonon-assisted luminescence in solids: application to hexagonal boron nitride," *Physical Review B*, vol. 99, no. 8, p. 081109(R), 2019. [Online]. Available: http://arxiv.org/abs/1807.11797

[128] S. Alkoy, C. Toy, T. Gönül, and A. Tekin, "Crystallization behavior and characterization of turbostratic boron nitride," *Journal of the European Ceramic Society*, vol. 17, no. 12, pp. 1415–1422, 1997. [Online]. Available: http://linkinghub.elsevier.com/retrieve/pii/S095522199700040X

[129] M. Dion, H. Rydberg, E. Schröder, D. C. Langreth, and B. I. Lundqvist, "Van der Waals density functional for general geometries," *Physical Review Letters*, vol. 92, no. 24, p. 246401(4), 2004.

[130] J. Klimeš, D. R. Bowler, and A. Michaelides, "Chemical accuracy for the van der Waals density functional," *Journal of Physics Condensed Matter*, vol. 22, no. 2, p. 022201(5), 2010.

[131] ——, "Van der Waals density functionals applied to solids," *Physical Review B*, vol. 83, no. 19, p. 195131(13), 2011.

[132] G. Kresse and J. Furthmüller, "Efficient iterative schemes for *ab initio* total-energy calculations using a plane-wave basis set," *Physical Review B*, vol. 54, no. 16, p. 11169(18), 1996.

[133] G. Kresse and J. Hafner, "*Ab initio* molecular-dynamics simulation of the liquid-metal–amorphous-semiconductor transition in germanium," *Physical Review B*, vol. 49, no. 20, p. 14251(19), 1994. [Online]. Available: http://link.aps.org/doi/10.1103/PhysRevB.49.14251

[134] S. Ismail-Beigi, "Truncation of periodic image interactions for confined systems," *Physical Review B*, vol. 73, no. 23, p. 233103(4), 2006.

[135] J. R. Yates, X. Wang, D. Vanderbilt, and I. Souza, "Spectral and Fermi surface properties from Wannier interpolation," *Physical Review B*, vol. 75, no. 19, p. 195121(11), 2007.

[136] J. Noffsinger, E. Kioupakis, C. G. Van De Walle, S. G. Louie, and M. L. Cohen, "Phonon-assisted optical absorption in silicon from first principles," *Physical Review Letters*, vol. 108, no. 16, p. 167402(5), 2012.

[137] R. Geick, C. Perry, and G. Rupprecht, "Normal Modes in Hexagonal Boron Nitride," *Physical Review*, vol. 146, no. 2, pp. 543–547, 1966.

[138] G. Shi and E. Kioupakis, "Electronic and optical properties of nanoporous silicon for solar-cell applications," *ACS Photonics*, vol. 2, pp. 208–215, 2015.

[139] J. Rass and N. Lobo-Ploch, "Optical Polarization and Light Extraction from UV LEDs," in *III-Nitride Ultraviolet Emitters: Technology and Applications*, M. Kneissl and J. Rass, Eds.   Springer, 2016, ch. 6, pp. 137–170.

[140] L. Williams and E. Kioupakis, "BAlGaN alloys nearly lattice-matched to AlN for efficient UV LEDs," *Applied Physics Letters*, vol. 115, p. 231103, 2019.

[141] D. Bayerl and E. Kioupakis, "Room-temperature stability of excitons and transverse-electric polarized deep-ultraviolet luminescence in atomically thin GaN quantum wells," *Applied Physics Letters*, vol. 115, p. 131101, 2019.

[142] K. Greenman, L. Williams, and E. Kioupakis, "Lattice-constant and band-gap tuning in wurtzite and zincblende BInGaN alloys," *Journal of Applied Physics*, vol. 126, p. 055702, 2019.

[143] X. Blase, A. Rubio, S. G. Louie, and M. L. Cohen, "Quasiparticle band structure of bulk hexagonal boron nitride and related systems," *Physical Review B*, vol. 51, no. 11, p. 6868(8), 1995.

[144] K. T. Winther and K. S. Thygesen, "Band structure engineering in van der Waals heterostructures via dielectric screening: the G$\Delta$W method," *2D Materials*, vol. 4, p. 025059(8), 2017.

[145] T. Galvani, F. Paleari, H. P. Miranda, A. Molina-Sánchez, L. Wirtz, S. Latil, H. Amara, and F. Ducastelle, "Excitons in boron nitride single layer," *Physical Review B*, vol. 94, no. 12, p. 125303(15), 2016.

[146] M. M. Ugeda, A. J. Bradley, S.-F. Shi, F. H. da Jornada, Y. Zhang, D. Y. Qiu, W. Ruan, S.-K. Mo, Z. Hussain, Z.-X. Shen, F. Wang, S. G. Louie, and M. F. Crommie, "Giant bandgap renormalization and excitonic effects in a monolayer transition metal dichalcogenide semiconductor," *Nature Materials*, vol. 13, pp. 1091–1095, 2014.

[147] C. Sevik and C. Bulutay, "Theoretical study of the insulating oxides and nitrides: $SiO_2$, $GeO_2$, $Al_2O_3$, $Si_3N_4$, and $Ge_3N_4$," *Journal of Materials Science*, vol. 42, no. 16, pp. 6555–6565, 2007.

[148] A. Trukhin, M. Kink, Y. Maksimov, J. Jansons, and R. Kink, "Luminescence of $GeO_2$ glass, rutile-like and $\alpha$-quartz-like crystals," *Journal of Non-Crystalline Solids*, vol. 352, no. 2, pp. 160–166, 2006.

[149] S. R. Shieh, A. Kubo, T. S. Duffy, V. B. Prakapenka, and G. Shen, "High-pressure phases in $SnO_2$ to 117 GPa," *Physical Review B*, vol. 73, no. 1, p. 014105(7), 2006.

[150] J. Haines and J. M. Léger, "X-ray diffraction study of the phase transitions and structural evolution of tin dioxide at high pressure: Relationships between structure types and implications for other rutile-type dioxides," *Physical Review B*, vol. 55, no. 17, pp. 11 144–11 154, 1997.

[151] D. Bayerl and E. Kioupakis, "Theoretical limits of thermoelectric figure of merit in n-type $TiO_2$ polymorphs," *Physical Review B*, vol. 91, no. 16, p. 165104(5), 2015.

[152] A. Schleife, J. B. Varley, F. Fuchs, C. Rödl, F. Bechstedt, P. Rinke, A. Janotti, and C. G. Van de Walle, "Tin dioxide from first principles: Quasiparticle electronic states and optical properties," *Physical Review B*, vol. 83, no. 3, p. 035116(9), 2011.

[153] S. Chae, J. Lee, K. A. Mengle, J. T. Heron, and E. Kioupakis, "Rutile $GeO_2$: An ultrawide-band-gap semiconductor with ambipolar doping," *Applied Physics Letters*, vol. 114, p. 102104(5), 2019.

[154] W. H. Strehlow and E. L. Cook, "Compilation of Energy Band Gaps in Elemental and Binary Compound Semiconductors and Insulators," *Journal of Physical and Chemical Reference Data*, vol. 2, no. 1, pp. 163–199, 1973.

[155] G. L. Tan, M. F. Lemon, D. J. Jones, and R. H. French, "Optical properties and London dispersion interaction of amorphous and crystalline $SiO_2$ determined by vacuum ultraviolet spectroscopy and spectroscopic ellipsometry," *Physical Review B*, vol. 72, no. 20, p. 205117(10), 2005.

[156] J. Matsuoka, N. Kitamura, S. Fujinaga, T. Kitaoka, and H. Yamashita, "Temperature dependence of refractive index of $SiO_2$ glass," *Journal of Non-Crystalline Solids*, vol. 135, no. 1, pp. 86–89, 1991.

[157] M. Nagasawa and S. Shionoya, "Exciton structure in optical absorption of $SnO_2$ crystals," *Physics Letters*, vol. 22, no. 4, pp. 409–410, 1966. [Online]. Available: http://www.degruyter.com/view/j/apeiron

[158] J. Pascual, J. Camassel, and H. Mathieu, "Resolved Quadrupolar Transition in $TiO_2$," *Physical Review Letters*, vol. 39, no. 23, pp. 1490–1493, 1977.

[159] Q.-J. Liu, Z.-T. Liu, L.-P. Feng, and H. Tian, "First-principles study of structural, elastic, electronic and optical properties of rutile $GeO_2$ and $\alpha$-quartz $GeO_2$," *Solid State Sciences*, vol. 12, no. 10, pp. 1748–1755, 2010.

[160] A. N. Trukhin, "Luminescence of $SiO_2$ and $GeO_2$ crystals with rutile structure. Comparison with $\alpha$-quartz crystals and relevant glasses (Review Article)," *Low Temperature Physics*, vol. 42, no. 7, pp. 561–569, 2016. [Online]. Available: http://aip.scitation.org/doi/10.1063/1.4959014

[161] P. Hermet, A. Lignie, G. Fraysse, P. Armand, and P. Papet, "Thermodynamic properties of the $\alpha$-quartz-type and rutile-type $GeO_2$ from first-principles calculations," *Physical Chemistry Chemical Physics*, vol. 15, no. 38, pp. 15 943–15 948, 2013. [Online]. Available: http://xlink.rsc.org/?DOI=c3cp52741g

[162] M. Sahnoun, C. Daul, R. Khenata, and H. Baltache, "Optical properties of germanium dioxide in the rutile structure," *European Physical Journal B*, vol. 45, no. 4, pp. 455–458, 2005.

[163] D. M. Ceperley and B. J. Alder, "Ground State of the Electron Gas by a Stochastic Method," *Physical Review Letters*, vol. 45, no. 7, pp. 566–569, 1980.

[164] J. P. Perdew and A. Zunger, "Self-interaction correction to density-functional approximations for many-electron systems," *Physical Review B*, vol. 23, no. 10, pp. 5048–5079, 1981.

[165] K. Bushick, K. Mengle, N. Sanders, and E. Kioupakis, "Band structure and carrier effective masses of boron arsenide: effects of quasiparticle and spin-orbit coupling corrections," *Applied Physics Letters*, vol. 114, p. 022101(5), 2019. [Online]. Available: https://arxiv.org/pdf/1809.09549.pdf

[166] M. Feneberg, C. Lidig, K. Lange, M. E. White, M. Y. Tsai, J. S. Speck, O. Bierwagen, and R. Goldhahn, "Anisotropy of the electron effective mass in rutile $SnO_2$ determined by infrared ellipsometry," *Physica Status Solidi A*, vol. 211, no. 1, pp. 82–86, 2014.

[167] H. Peelaers and C. G. Van de Walle, "Lack of quantum confinement in $Ga_2O_3$ nanolayers," *Physical Review B*, vol. 96, no. 8, pp. 1–5, 2017.

[168] J. B. Varley, A. Janotti, and C. G. Van de Walle, "Group-V impurities in $SnO_2$ from first-principles calculations," *Physical Review B*, vol. 81, no. 24, p. 245216(7), 2010.

[169] M. Suzuki and T. Uenoyama, "Strain effect on electronic and optical properties of GaN/AlGaN quantum-well lasers," *Journal of Applied Physics*, vol. 80, no. 12, pp. 6868–6874, 1996.

[170] H. He, R. Orlando, M. A. Blanco, R. Pandey, E. Amzallag, I. Baraille, and M. Rérat, "First-principles study of the structural, electronic, and optical properties of $Ga_2O_3$ in its monoclinic and hexagonal phases," *Physical Review B*, vol. 74, no. 19, p. 195123(8), 2006.

[171] J. B. Varley, J. R. Weber, A. Janotti, and C. G. Van de Walle, "Oxygen vacancies and donor impurities in $\beta$-$Ga_2O_3$," *Applied Physics Letters*, vol. 97, no. 14, p. 142106(3), 2010.

[172] M. Rohlfing and S. G. Louie, "Electron-hole excitations and optical spectra from first principles," *Physical Review B*, vol. 62, no. 8, pp. 4927–4944, 2000.

[173] K. Reimann and M. Steube, "Experimental determination of the electronic band structure of $SnO_2$," *Solid State Communications*, vol. 105, no. 10, pp. 649–652, 1998.

[174] C. Schweitzer, K. Reimann, and M. Steube, "Two-photon spectroscopy of $SnO_2$ under hydrostatic pressure," *Solid State Communications*, vol. 110, no. 12, pp. 697–700, 1999.

[175] B. Song, K. Chen, K. Bushick, K. A. Mengle, F. Tian, G. Gamage, Z. Ren, E. Kioupakis, and G. Chen, "Optical properties of cubic boron nitride," *arXiv:1911.04914 [cond-mat.mtrl-sci]*.

[176] M. Lin, B. Sverdlov, S. Strite, H. Morkoç, and A. Drakin, "Refractive indices of wurtzite and zincblende GaN," *Electronics Letters*, vol. 29, no. 20, pp. 1759–1761, 1993.

[177] S. Das, G. Shi, N. Sanders, and E. Kioupakis, "Electronic and Optical Properties of Two-Dimensional $\alpha$-PbO from First Principles," *Chemistry of Materials*, vol. 30, no. 20, pp. 7124–7129, 2018.

[178] K. Takakura, D. Koga, H. Ohyama, J. M. Rafi, Y. Kayamoto, M. Shibuya, H. Yamamoto, and J. Vanhellemont, "Evaluation of the crystalline quality of $\beta$-$Ga_2O_3$ films by optical absorption measurements," *Physica B*, vol. 404, pp. 4854–4857, 2009. [Online]. Available: http://dx.doi.org/10.1016/j.physb.2009.08.167

[179] J. F. Muth, J. H. Lee, I. K. Shmagin, R. M. Kolbas, H. C. Casey, B. P. Keller, U. K. Mishra, and S. P. DenBaars, "Absorption coefficient, energy gap, exciton binding energy, and recombination lifetime of GaN obtained from transmission measurements," *Applied Physics Letters*, vol. 71, no. 18, pp. 2572–2574, 1997.

[180] K. Afridi, S. Ang, J. Bock, S. Chowdhury, S. Datta, K. Evans, J. Flicker, M. Hollis, N. Johnson, K. Jones, P. Kogge, S. Krishnamoorthy, M. Marinella, T. Monson, S. Narumanchi, P. Ohodnicki, R. Ramesh, M. Schuette, J. Shalf, S. Shahedipour-Sandvik, J. Simmons, V. Taylor, and T. Theis, "Basic Research Needs for Microelectronics," Department of Energy Office of Science, Tech. Rep., 2018.

[181] K. A. Mengle and E. Kioupakis, "Vibrational and electron-phonon coupling properties of $\beta$-Ga $_2$ O $_3$ from first-principles calculations: Impact on the mobility and breakdown field," *AIP Advances*, vol. 9, no. 1, p. 015313, 2019. [Online]. Available: http://aip.scitation.org/doi/10.1063/1.5055238

[182] A. Kyrtsos, M. Matsubara, and E. Bellotti, "On the feasibility of p-type Ga2O3," *Applied Physics Letters*, vol. 112, no. 3, 2018.

[183] K. A. Mengle, S. Chae, and E. Kioupakis, "Quasiparticle band structure and optical properties of rutile $GeO_2$, an ultra-wide-band-gap semiconductor," *Journal of Applied Physics*, vol. 126, no. 8, p. 085703, 2019. [Online]. Available: http://aip.scitation.org/doi/10.1063/1.5111318

[184] S. Poncé, E. R. Margine, C. Verdi, and F. Giustino, "EPW: Electron–phonon coupling, transport and superconducting properties using maximally localized Wannier functions," *Computer Physics Communications*, vol. 209, pp. 116–133, 2016.

[185] F. Giustino, M. L. Cohen, and S. G. Louie, "Electron-phonon interaction using Wannier functions," *Physical Review B*, vol. 76, no. 16, p. 165108, 2007. [Online]. Available: https://link.aps.org/doi/10.1103/PhysRevB.76.165108

[186] X. Wang, J. R. Yates, I. Souza, and D. Vanderbilt, "*Ab initio* calculation of the anomalous Hall conductivity by Wannier interpolation," *Physical Review B - Condensed Matter and Materials Physics*, vol. 74, no. 19, pp. 1–15, 2006.

[187] C. Verdi and F. Giustino, "Fröhlich electron-phonon vertex from first principles," *Physical Review Letters*, vol. 115, no. 17, pp. 1–5, 2015.

[188] S. Poncé, E. R. Margine, and F. Giustino, "Towards predictive many-body calculations of phonon-limited carrier mobilities in semiconductors," *Physical Review B*, vol. 97, no. 12, pp. 1–5, 2018.

[189] K. A. Mengle and E. Kioupakis, "Electron and hole mobility of rutile $GeO_2$ from first principles : an ultrawide-band-gap semiconductor for power electronics," *arXiv:1911.09750 [cond-mat.mtrl-sci]*.

[190] S. Dagli, K. A. Mengle, and E. Kioupakis, "Thermal conductivity of AlN, GaN, and $Al_xGa_{1-x}N$ alloys as a function of composition, temperature, crystallographic direction, and isotope disorder from first principles," *arXiv:1910.05440 [cond-mat.mtrl-sci]*, 2019. [Online]. Available: http://arxiv.org/abs/1910.05440

[191] K. Bushick, S. Chae, Z. Deng, J. Heron, and E. Kioupakis, "Boron Arsenide Heterostructures: Lattice-Matched Heterointerfaces, and Strain Effects on Band Alignments and Mobility," *arXiv:1909.01449 [cond-mat.mtrl-sci]*. [Online]. Available: https://arxiv.org/abs/1909.01449

[192] T. P. Mernagh and L. G. Liu, "Temperature dependence of Raman spectra of the quartz-and rutile-types of $GeO_2$," *Physics and Chemistry of Minerals*, vol. 24, no. 1, pp. 7–16, 1997.

[193] M. Madon, P. Gillet, C. Julien, and G. D. Price, "A vibrational study of phase transitions among the $GeO_2$ polymorphs," *Physics and Chemistry of Minerals*, vol. 18, no. 1, pp. 7–18, 1991.

[194] Y. Zhang, A. Neal, Z. Xia, C. Joishi, J. M. Johnson, Y. Zheng, S. Bajaj, M. Brenner, D. Dorsey, K. Chabak, G. Jessen, J. Hwang, S. Mou, J. P. Heremans, and S. Rajan, "Demonstration of high mobility and quantum transport in modulation-doped $\beta$-$(Al_xGa_{1-x}O_3/Ga_2O_3$ heterostructures," *Applied Physics Letters*, vol. 112, no. 17, p. 173502, 2018. [Online]. Available: http://aip.scitation.org/doi/10.1063/1.5025704

[195] B. J. Baliga, *Fundamentals of Power Semiconductor Devices.* Berlin: Springer Science & Business Media, 2010.

[196] M. E. Levinshtein, S. L. Rumyantsev, and M. S. Shur, *Properties of Advanced Semiconductor Materials: GaN, AIN, InN, BN, SiC, SiGe.* Hoboken, NJ: John Wiley & Sons, 2001.

[197] Z. Feng, A. F. Anhar Uddin Bhuiyan, M. R. Karim, and H. Zhao, "MOCVD homoepitaxy of Si-doped (010) $\beta$-Ga2O3 thin films with superior transport properties," *Applied Physics Letters*, vol. 114, no. 25, 2019.

[198] S. Sze and K. N. Kwok, *Physics of semiconductor devices*, 3rd ed. Hoboken, NJ: John Wiley & Sons, 2007.

[199] J. A. S. Barker and M. Ilegems, "Infrared Lattice Vibrations and Free-Electron Dispersion in GaN," *Physical Review B*, vol. 7, no. 2, 1973.

[200] K. Sasaki, A. Kuramata, T. Masui, E. G. Víllora, K. Shimamura, and S. Yamakoshi, "Device-quality $\beta$-Ga$_2$O$_3$ epitaxial films fabricated by ozone molecular beam epitaxy," *Applied Physics Express*, vol. 5, no. 3, pp. 5–8, 2012.

[201] D. M. Roessler and W. A. Albers, "Infrared reflectance of single crystal tetragonal GeO$_2$," *Journal of Physics and Chemistry of Solids*, vol. 33, no. 2, pp. 293–296, 1972.